ABSTRACT

Title: HIGHLY SENSITIVE FIBER BRAGG GRATING BIOSENSORS

Christopher J. Stanford, Master of Science, 2008

Thesis Directed by: Professor Mario Dagenais
Department of Electrical and Computer Engineering

Fiber Bragg grating sensors are highly sensitive, cost-effective solutions in chemical and biological sensing. By reducing the resolution of the optical interrogation set-up and enhancing the fiber's evanescent field, etched fiber Bragg gratings (FBG) can detect minimal refractive index shifts. Etched FBG Fabry Perot sensors decrease detectable index shifts (~$2x10^{-9}$ riu) by introducing extremely narrow spectral resonances to single FBG spectra. Furthermore, we describe the fabrication of ultrahigh finesse fiber cavities and a temperature-compensated mount that will be implemented in future chemical testing.

With highly sensitive refractive index sensors, we developed procedures for investigating complex surface chemistry. Chemical species are immobilized on the sensor's silica surface in order to study protein conjugation with Concanavalin A, 21-mer DNA hybridization, monolayer adsorption, and silanization. Sensor results with homogeneous or multilayer environments demonstrate good agreement with theoretical Bragg shifts calculated using the beam propagation method of determining the effective modal index.

HIGHLY SENSITIVE FIBER BRAGG GRATING BIOSENSORS

by

Christopher J. Stanford

Thesis submitted to the Faculty of the Graduate School of the
University of Maryland, College Park in partial fulfillment
of the requirements for the degree of
Master of Science
2008

Advisory Committee:

Professor Mario Dagenais, Chair
Professor Christopher Davis
Professor Philip DeShong
Professor Julius Goldhar

Acknowledgements

I would like to sincerely thank my adviser Professor Mario Dagenais for his direction and support in both the professional and personal paths that I have chosen while at the university. Johann Wolfgang von Goethe, a 19th Century German poet and philosopher, once wrote, "Treat a man as he is, he will remain so. Treat a man the way he can be and ought to be, and he will become as he can be and should be." Prof. Dagenais expected excellence and thus inspired excellence.

I would also like to extend my gratitude to the professors serving on my thesis committee: Profs. Christopher Davis, Philip DeShong, and Julius Goldhar.

In my time at the University of Maryland, my colleagues have been essential in my intellectual growth. Special thanks must be offered to Thanos Chryssis, Dr. Simarjeet Saini, Juhee Park, and Matt Hurley.

My family and friends cannot be sufficiently thanked for their abundant support and unwavering love throughout these years. Without such tremendous stability and understanding this process would not have been possible.

And my wife. Caring, hopeful, patient, and inspiring. This thesis is dedicated to the person who so selflessly encourages me to be and do the best. I love and thank you.

TABLE OF CONTENTS

LIST OF FIGURES

3.4.6 Direct-write set-up in which an amplitude mask shapes the UV light that exposes the grating. Fibers are typically mounted on spools that move the fiber precisely.

3.4.7 Phase mask set-up that recombines the diffracted first-order modes with parallel mirrors and blocks the zero-order mode directly.

3.4.8 Plot of electromagnetic wave amplitudes within a zero-mode nullified phase mask and within the 500nm that is adjacent to the corrugation. The boxed region contains the phase mask and the plane wave is launched from the top and propagates downward.

4.1.1 Momentum conservation for optical signals reflected backward from a fiber Bragg grating. Optical momentum is denoted by the propagation constant *k*.

4.1.2 Plot of the reflection spectrum of a FBG with index contrast of 1e-4. Various grating lengths are plotted. The index contrast was low enough so that the spectra are limited by grating length and not coupling strength.

4.1.3 Plots of the reflection spectrum of a 7.5mm long grating. Various index contrasts are plotted to show that reflectivity and bandwidth increase with the coupling constant.

4.2.1 Fiber Bragg grating index profiles of (a) uniform raised-cosine, (b) Gaussian apodized, and (c) randomly nonuniform patterns.

4.2.2 Plots of the grating reflectivity vs. detuning for uniform and nonuniform index modulations.

4.2.3 Plots of the reflectivity versus detuning for a uniform grating and a Gaussian apodized grating. Note that the reflectivity is expressed on a log scale in order to highlight the extent of the side lobe suppression.

4.3.1 Side-view of the temperature-compensated mount design. Epoxy holds the two metals in contact at the end of the low-CTE metal.

4.3.2 Plot of the Bragg wavelength vs. effective index for fundamental and first higher order modes.

5.5.1 Depiction of the reflections and optical path for light within a fiber Fabry Perot

5.5.2 Spectral plots can be analyzed by calculating the electric fields of (a) a lossless, symmetric Fabry Perot cavity, (b) a lossy asymmetric Fabry Perot cavity, or (c) a Fabry Perot cavity with the R, T, α, and L are wavelength dependent, as with practical FFPs.

5.5.3 Transmission spectra for a Fabry Perot comprised of two mirrors of equal reflectivity. Plots show how the T-spectrum changes for stronger gratings.

5.5.4 Reflection spectra for a Fabry Perot comprised of two mirrors of equal reflectivity. Plot shows how the R-spectrum changes for stronger gratings.

5.2.1 Height-coded of the Fabry Perot finesse versus the grating strength. Grating strength is represented by the minimum transmission

LIST OF ABBREVIATIONS

AFM	atomic force microscopy
APDMS	3-aminopropyldimethylethoxysilane
APTES	3-aminopropyltriethoxysilane
BPM	beam propagation method
BTMS	butyltrimethylethoxysilane
ConA	Concanavalin A
CTE	constant of thermal expansion
EDFA	erbium doped fiber amplifier
FBG	fiber Bragg grating
FDTD	finite difference time domain
FFP	fiber Fabry Perot
FP	Fabry Perot
FSR	free spectral range
Ge-Si	germanium silicon
Ge-O	germanium oxygen
HeNe	helium neon
KrF	krypton fluoride
LPG	long period grating
MOCVD	metal oxide chemical vapor deposition
OSA	optical spectrum analyzer
R	reflectivity
RI	refractive index
riu	refractive index unit
SMF	single mode fiber
T	transmittivity

Chapter 1: Introduction

Fiber Bragg grating sensors and sensor systems can offer highly sensitive, cost-effective solutions for chemical, mechanical, and optical sensing. While fiber Bragg gratings have been implemented in various sensing applications over the past few decades, recent efforts explore the limits of refractive index sensing. Chemical and biological sensing has motivated the detection and reduction of minimal refractive index shifts around fiber gratings. In some applications, fiber Bragg gratings may be considered too sensitive to environmental conditions. While the grating sensors display sensitivity to strain, temperature, and vibrations, it is the purpose of this thesis to enhance the ultimate resolution of detecting refractive index shifts. Two fiber sensors have been investigated: an etched fiber Bragg grating and an etched fiber Fabry Perot. The etched fiber Bragg grating was etched in-house, enhancing sensitivity to refractive index shifts, and was extensively tested as a chemical sensor with DNA, siloxane, and protein studies. The etched fiber Fabry Perot sensors were entirely developed and fabricated in-house though they have not yet been thoroughly tested with refractive index measurements. Minimum index resolutions have been improved from $1x10^{-6}$ to $5x10^{-9}$ refractive index units (riu) by increasing the spectral sensitivity, decreasing the spectral linewidths, and improving the optical interrogation technique.

Both sensors seek to influence the fiber's effective modal index by allowing the environment to penetrate the optical mode's evanescent field. With typical single mode

fibers, the cladding extends over 100μm from the interface with the core. These fibers are typically designed with low index contrast between the core and cladding, and as such, the mode extends deeply into the cladding but not far enough to reach the environment. Chemical etching through the cladding and core reduces the size of the optical mode but enhances field amplitudes in the environment outside of the fiber. When the effective modal index shifts with the environment, highly sensitive measurements are acquired from the reflection spectra of Bragg gratings and fiber Bragg Fabry Perots. Sensitivity depends on the physical fiber parameters such as core index and fiber diameter as well as on the refractive index being measured.

Reducing the minimum resolution of refractive index sensors is essential to measuring and quantifying chemical processes. The etched fiber Bragg sensor has been used in studies of DNA hybridization, surface silanization, monolayer adsorption, and protein conjugation. By immobilizing certain chemical species on the silica surface, etched Bragg sensors monitor selective chemical processes by differentiating between refractive index shifts due to complementary and uncomplementary species. Furthermore, real-time Bragg wavelengths shifts show the progression of chemical attachments to the fiber surface while also elucidating information about parallel processes, such as water adsorption. In a study of the difference between single monolayer and multilayer formation of 3-aminipropyldimethylethodysilane and 3-aminopropyltriethoxysilane, our refractive index sensor confirmed that several oligomeric monolayers form on silica surfaces for siloxanes with multiple oxygenated branches. Additionally, real-time monitoring of the surrounding index within the siloxane attachments revealed the evolution of adsorbed water layers only nanometers thick.

Substantial progress has been made in forming short, high-Q cavities with fiber Bragg gratings that may ultimately result in single molecule detection.

Chapter 2 introduces the structure of typical single mode fibers and begins the theoretical analysis of effective index and refractive index sensing. Discussions focus on how shifts in the effective modal index may be modeled with beam propagation method. An argument is established that etching into fibers enhances the sensitivity to surrounding indices.

Chapter 3 describes how fiber Bragg gratings are formed within photosensitive fibers. Sections compare various types of photosensitive fiber, UV sources, and writing techniques. Ultimately, our in-house fiber Bragg gratings were written by a KrF excimer laser with the contact-mode phase mask technique.

Chapter 4 establishes the theoretical models and modeling that describe the fiber and grating characteristics that enhance spectral features. The transfer matrix method is described in order to explain the spectral qualities of practical Bragg gratings in the context of explaining reflection and transmission data from in-house Bragg grating fabrication. Furthermore, the discussion of fiber Bragg grating sensitivity continues so as to justify suppressing sensitivity to temperature and strain.

Chapter 5 is structured similarly to Chapter 4 though describes fiber Fabry Perots. The goal of this section is to justify the benefits of using sharp spectral features in order to

minimize the resolution of refractive index shifts. The finesse of fiber Fabry Perot sensors is the most important figure of merit.

Chapter 6 describes the fabrication of the sensors. Fabrication of the etched fiber Bragg sensor only involves etching, because the FBG is pre-written and pre-packaged. Fabrication of the etched Fabry Perot sensor is detailed from FBG inscription, to temperature-compensated housings, and then to etching. Cavity finesses of 1000 have been achieved.

Chapters 7 and 8 discuss the etched FBG sensor testing. Chapter 7 describes the results from sensing homogenous surrounding solutions and Chapter 8 describes the results from multilayer refractive index sensing. Results agree very well with theoretical predictions derived from beam propagation method calculations.

Chapter 2: Optical Fiber Theory

We inscribed our Bragg grating sensors in germanosilicate single mode optical fibers. The optical fiber consists of two concentric cylinders of glass with different dopings: a higher refractive index of glass surrounded by a lower refractive index of glass. By properly selecting the refractive indices and dimensions of the core and cladding regions that comprise the total internal reflection, we ensure that the light remains confined by total internal reflection within the fiber core. Maxwell's equations govern how the light propagates down the dielectric waveguide and the specifications (e.g. refractive index and dimensions) govern how effective the waveguide will be as a refractive index sensor. Using the beam propagation method, solutions to Maxwell's equations can be computed for various models of refractive index profiles.

2.1 The Single Mode Fiber

Widespread commercial applications of single mode fiber (SMF), such as in optical communication networks, have made this type of fiber inexpensive, accessible, and standardized. In the subsequent chapters of this thesis, two types of SMFs will be discussed due to their intrinsic photosensitivity: plain germanosilicate and germanosilicate fibers co-doped with boron. While photosensitivity and material properties will be discussed in detail in Chapter 3, it is important to mention here that dopants (e.g. germanium and boron) can alter the refractive index of fused silica in

proportion to their percent composition. Introducing germanium within the glass core provides the refractive index contrast necessary to confine light within the dielectric guide.

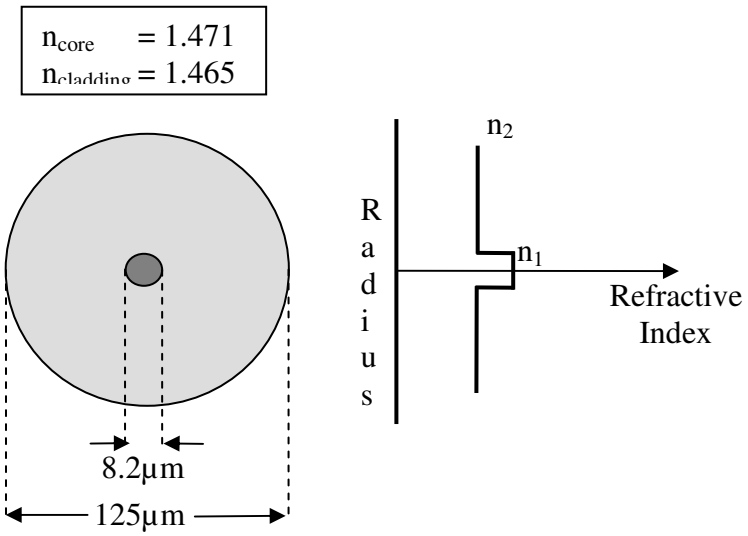

Figure 2.1.1 Standard SMF from Corning. Core and cladding diameters and indices are labeled.

In typical step-index fibers, the index contrast and core diameter are critical in creating the single mode condition. As an example, Fig. 2.1.1 shows a standard single mode fiber from Corning (SMF-28). The fiber is designed to exhibit low loss (e.g. 0.2dB/km) at an optical wavelength of 1550nm in order to maintain signal strength over long distances in communications networks [Ref. 2.1.1].

A highly photosensitive fiber from Newport Corporation is model no. F-SBG-15, a germanosilicate fiber co-doped with boron. This fiber has been manufactured with similar design characteristics to the Corning SMF-28 so that integrating the two is convenient. Newport claims that the numerical aperture and mode diameter of F-SBG-15 is matched to SMF-28 so that "high quality" fiber gratings may be incorporated as in-line spectral filters. Photosensitive single mode fibers are most commonly used to fabricate

multiplexers and demultiplexers within fiber communications networks, routing specific communications channels to the proper part of the network.

In a standard SMF, "single mode" will refer to the condition in which a single eigenvalue solution exists within the waveguide and is associated with how the electromagnetic radiation fills the space. The eigenvalue may frequently be called the propagation constant but within this thesis I will refer to the form of the eigenvalue that is referred to as the effective index. Effective indices of single mode fibers may be measured directly by incorporating optical filters known as fiber Bragg gratings and monitoring how light reflects from these components. Furthermore, the effective index sums up how the light interacts with different regions in space, including the refractive index outside of the core region [Ref. 2.1.2, 2.1.3].

2.2 Effective Index of Optical Fiber

The propagation of electromagnetic waves is described by Maxwell's equations for dielectric media:

$$\nabla \times \mathbf{E} = -\frac{\partial \mathbf{B}}{\partial T} \tag{2.2.1}$$

$$\nabla \times \mathbf{H} = \frac{\partial \mathbf{D}}{\partial T} \tag{2.2.2}$$

$$\nabla \bullet \mathbf{D} = 0 \tag{2.2.3}$$

$$\nabla \bullet \mathbf{B} = 0 \tag{2.2.4}$$

By combining Eqn. 2.2.1 and Eqn. 2.2.2, one may express a wave equation for homogeneous, nondispersive materials in the form of the wave equation:

$$\nabla^2 \mathbf{E} + \beta^2 \mathbf{E} = 0 \tag{2.2.5}$$

where,

$$\beta = n_{eff} k_0 = \frac{2\pi n_{eff}}{\lambda} \qquad (2.2.6)$$

The Helmholtz equation in Eq. 2.2.5 relates the electric field and the propagation constant, β. This wave equation describes electromagnetic wave propagation through a material of effective index n_{eff}. Constraints on the space that the electromagnetic wave travels through thus create constraints on the Helmholtz equation. These constraints consist of defining the electric permittivity in the volume of the optical wave. Fibers are cylindrical waveguides and therefore the constraints on the Helmholtz equation within glass fibers force cylindrical symmetry and impose boundary conditions. Cylindrical boundary conditions are satisfied at the core-cladding and cladding-air interfaces. Furthermore, solutions to the Helmholtz equation must consider that the refractive index profile takes the shape of concentric cylinders. Under these constraints, solutions reveal both the field amplitude everywhere within the fiber and a single effective modal index. The cylindrical boundaries and symmetry is summarized by the following modified Helmholtz equation:

$$\left(\nabla_\rho + \nabla_\phi + \nabla_z\right)E_z + \beta^2 E_z = \left(\frac{\partial^2}{\partial^2 \rho} + \frac{1}{\rho}\frac{\partial}{\partial \rho} + \frac{1}{\rho^2}\frac{\partial^2}{\partial \phi^2} + \frac{\partial^2}{\partial z^2}\right)E_z + \beta^2 E_z = 0$$

(2.2.7)

Two distinct solutions for Eqn. 2.2.7 describe the field and propagation constants within the core and within the cladding. Optical fiber refractive index sensors take advantage of the link between the effective index and the mode amplitudes in both the core and the cladding.

Confinement is a measure of total optical power that remains in the fiber core and is a factor in evaluating the effective modal index. Highly confined modes have weak evanescent fields outside of the core region. As such, weakly-confined optical modes impact the effective index more than strongly-confined modes. Physical parameters of the waveguide (e.g. core diameter, step-index contrast) and the wavelength of the confined optical field will determine how many solutions exist. The benefits of creating and using high order modes to sense changes in the environment's refractive index will be discussed in the following sections.

2.3 Fiber Modes

For each fiber mode, the optical field can be characterized by a single eigenvalue β, which relates the effective index to the wavelength of light. For a set of fiber parameters (e.g. physics dimensions and refractive indices), at least one eigenvalue exists, though not necessarily more than one. The lowest order and simplest mode is considered the "fundamental mode." A single mode fiber is designed so that only one eigenvalue exists. The mode associated with that eigenvalue is the fundamental mode. Strictly speaking, a single mode fiber allows the propagation of two polarization modes that are orthogonal to each other. If the fiber supports more than just the fundamental mode then it is a multimode fiber. The normalized frequency parameter, V, indicates whether a set of fiber parameters is single mode or multimode

$$V = k_0 a \sqrt{\left(n_{core}^{\ 2} - n_{cladding}^{\ 2}\right)} \qquad (2.3.1)$$

where k_0 is the propagation constant and a is the core radius. If V<2.405 then only a single mode propagates in the fiber. This is the single mode condition. This condition

arises from the eigenvalue equations and the first zero of the J_0 Bessel function. The single mode condition does not indicate the exact number of modes, only whether or not more than one mode exists. For a given V parameter, each mode will possess different propagation constants and therefore different effective index values.

$$b = \frac{\beta / k_0 - n_{cladding}}{n_{core} - n_{cladding}} \qquad (2.3.2)$$

The normalized propagation is plotted against the normalize frequency in Figure 2.3.1 below.

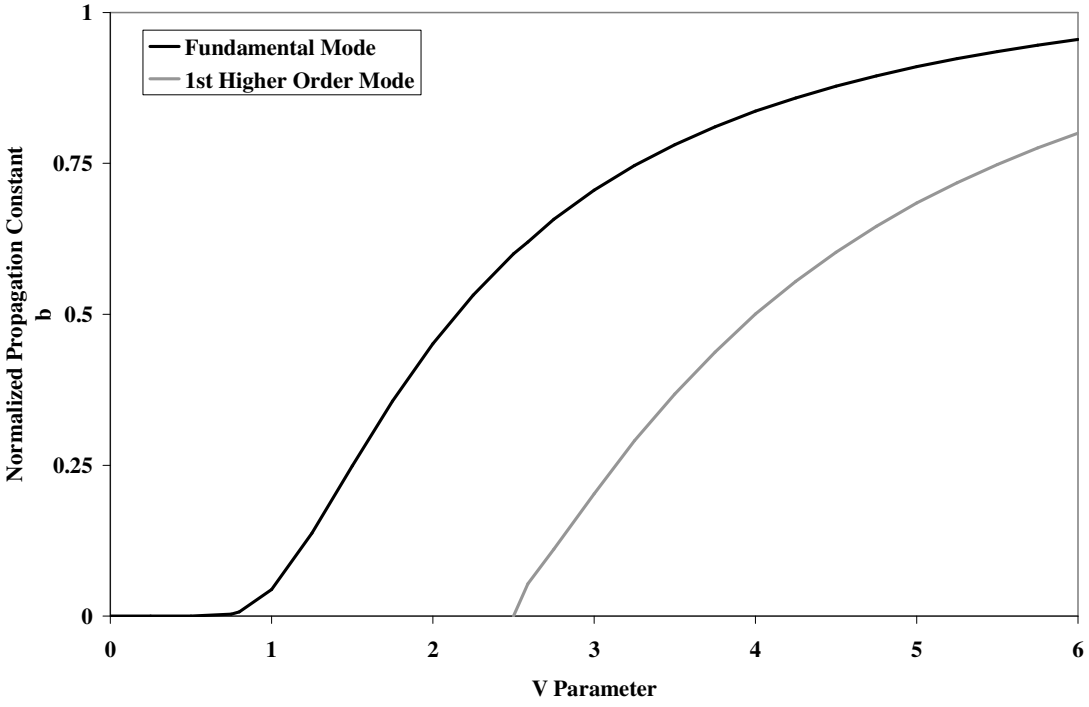

Figure 2.3.1 Plot of the allowed optical fiber modes in terms of the normalized frequency, V parameter, and normalized propagation constant

The plots in Figure 2.3.1 show that the effective index is not linear as a function of V and therefore fiber parameters, such as diameter, may be chosen to maximize the dependence of the effective index on the surrounding (cladding) index.

The amplitude of the fundamental mode follows a different type of Bessel function in the core and in the cladding. For weakly guided modes, the field resembles a two dimensional Gaussian function. Outside of the core, the field amplitude resembles an exponential decay and does not have a real-valued propagation constant in the axial direction [Ref. 2.3.1]. These are evanescent fields. Optical fiber sensors have been used to determine the refractive index changes of the core during exposure to UV light [Ref. 2.3.2], but our goal is to use the evanescent field of the fiber to sense the change of the index outside of the fiber.

It should stand to reason that a single mode fiber may be converted into a multimode fiber if the diameter and cladding index of a single mode fiber are changed (refer to Fig. 2.3.1). A higher order mode will be represented by a different eigenvalue and therefore a different field amplitude and effective index. Furthermore, the sensitivity of the effective index to the cladding index varies from one mode to another. Higher order modes will be less confined to the core region and their evanescent fields will extend further from the core-cladding interface than the fundamental mode fields. Effective indices of higher order modes will increase the weight of the refractive index regions immediately outside of the fiber surface because the effective index is weighted by the intensity of light in each fiber region. The methods for quantifying effective index and shifts with cladding index are analyzed in Section 2.4.

2.4 Beam Propagation Method

The beam propagation method is a computational approach to solving the Helmholtz equation in materials. Simulation fields are discretized with either uniform or

nonuniform grid spacing. Each grid element exhibits homogenous optical properties, namely the complex permittivity. A user-defined electromagnetic wave is launched into the simulation and solutions to the Helmholtz equations are solved within each grid element. Solutions yield mode amplitudes and propagation constants. A stipulation of the method is that the fields are paraxial and slowly varying in transverse directions [Ref. 2.4.1]. The method starts with approximating the electric field within the Helmholtz equation to be of a slowly varying amplitude with a spatially-dependent phase term:

$$\nabla^2 \mathbf{E} + \beta^2 \mathbf{E} = 0 \qquad (2.4.1)$$

$$\nabla^2 \left(A(x,y,z) e^{jn_{cladding} k_0 z} \right) + \beta^2 \left(A(x,y,z) e^{jn_{cladding} k_0 z} \right) = 0 \qquad (2.4.2)$$

where $n_{cladding}$ is the refractive index of the cladding and A(x,y,z) describes the complex amplitude of the slowly varying envelope function of the optical mode. Continuing the substitution shows that the mode propagation is governed by the index variation in space (i.e. the waveguide structure):

$$\nabla^2 A(x,y,z) - 2jk_0 n_0 \frac{\partial A}{\partial z} + k_0{}^2 \left(n^2 - n_0{}^2 \right) A(x,y,z) = 0$$

(2.4.3)

In BPM, electromagnetic waves are approximated in two parts: boundary-free and waveguide-confined. If the space along the waveguide's axis is defined with subunits of length L, then the solutions are calculated as free-space propagation for the space z = [0,L/2] and then calculated with a phase retardation for the space z = [L/2,L]. [Reference 2.4.2] This ultimately results in determining the output amplitude, A(x,y,L), from the input amplitude, A(x,y,0), for every increment along the waveguide axis.

Software packages for BPM, such as BeamProp from RSoft CAD Group, are commercially available and user-friendly. Our effective index modeling is assisted by

the BPM calculations of BeamProp. Within the RSoft CAD, designing a waveguide structure consists of dividing each of three dimensions into individual, uniform grids and defining the complex refractive index within each grid element. BPM does not inherently exclude nonuniform grids, although we only utilize uniform grids in our modeling.

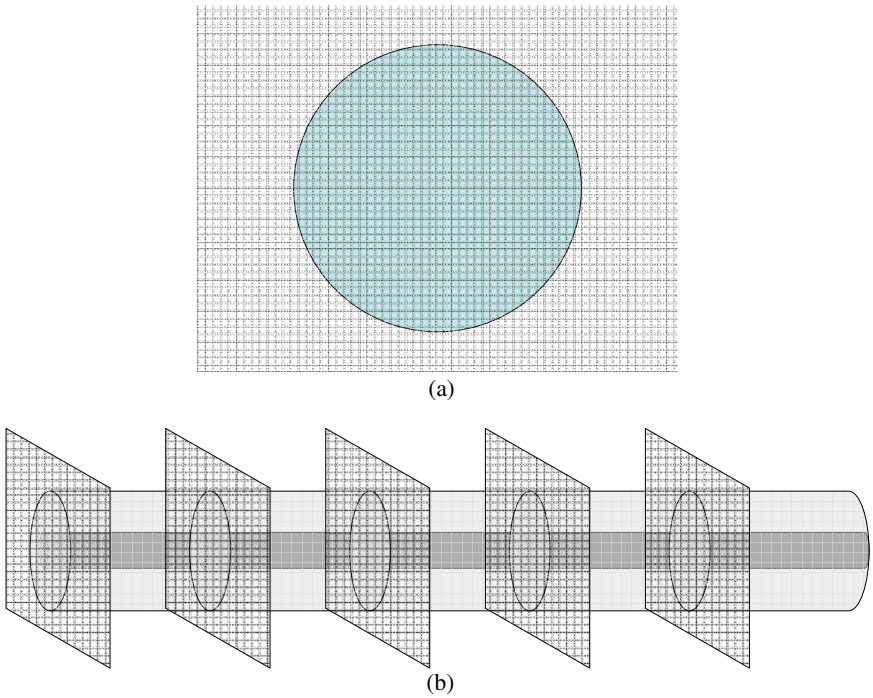

Figure 2.4.1 Depiction of BPM grids in the (a) transverse and (b) axial dimensions

The cross-sectional area of single mode fibers is micrometers by micrometers, however the models grid size is customized to the smallest feature size of the structure. In the context of an etched fiber sensor, the feature may be the curvature of a bare fiber surface or the 10nm thick monolayer on the surface of the fiber. Customarily, we ensure that at least ten grid elements are within the most rapidly varying index regions. A multilayer model may incorporate the following three layers: the 5µm diameter glass fiber, a 10nm molecular monolayer, and millimeters (or milliliters) of buffer solution. In this example, the Cartesian grid size would be set to 1nm at most. The longitudinal grid

size, along the direction of light propagation, would not need to be constrained by the same dimensions. Instead, the z-axis grid size is set to be equal or less than the input wavelength to ensure mathematical convergence of the solution.

The electromagnetic wave input, or launch field, is arbitrary as long as the input allows the solution to converge. As the mode propagates and the Helmholtz equation is solved for increments along the fiber, energy may radiate toward the boundaries of the simulation window, where the simulation is designed to absorb and nullify any boundary fields. The light that remains in the simulation interacts with the fiber and becomes guided by total internal reflection within the waveguide. Simulations converge as long as a minimal amount of light radiates out of the solution from one longitudinal step to another. Typically, the models use waveguides structures with sufficient path lengths to find a convergent solution (i.e. non-radiative fields). If the BPM calculation becomes unstable, due to high index contrast between grid elements for example, it has been observed that the most effective launch field is an approximation of the final solution. This occurs when modeling a 10nm bioattachment layer where $\Delta n \approx 0.1$ refractive index unit (riu) from one grid element to another. In this example, the BPM solution is determined by removing the high index contrast (i.e. biolayer) and then using the output as the launch field for the full layer structure.

Our modeling focuses on two parts of the BPM output: the amplitude of the electric field and the associated effective index of the mode. In Chapter 3 we will examine how etching increases sensitivity of our fiber Bragg grating refractive index sensors. We examine how changing the refractive index layers adjacent to the sensor surface alters both the amplitude and effective index of the optical mode, providing a

measurable quantity for the liquid's index or for the chemical adsorption. The following sections serve to illustrate the BPM design and modeling of an etched fiber waveguide.

2.4.1 Single Mode Model

Figures 2.4.2 and 2.4.3 show a typical single mode fiber structure designed within BeamProp and the BPM solution of the fiber's fundamental mode. The fiber design follows the specifications of a germanosilicate fiber from Corning: SMF-28.

$n_{core} = 1.4708$	$D_{core} = 8.2\mu m$
$n_{cladding} = 1.465$	$D_{cladding} = 125\mu m$

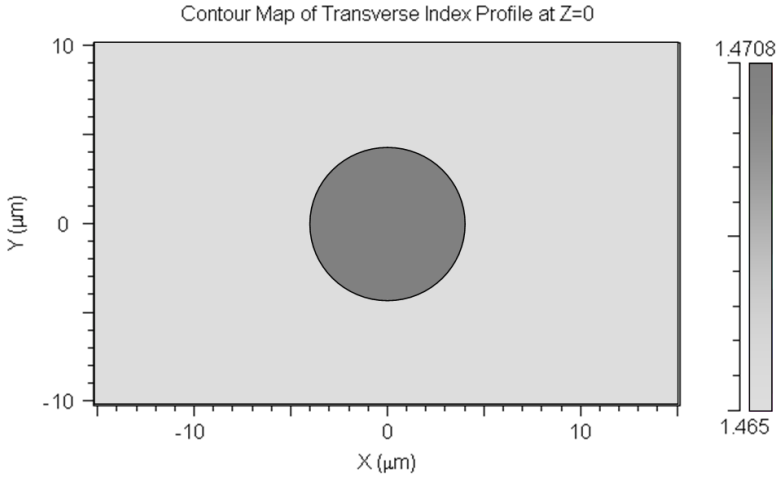

Figure 2.4.2 Index profile of standard SMF fiber. Diameter = 8.2µm.

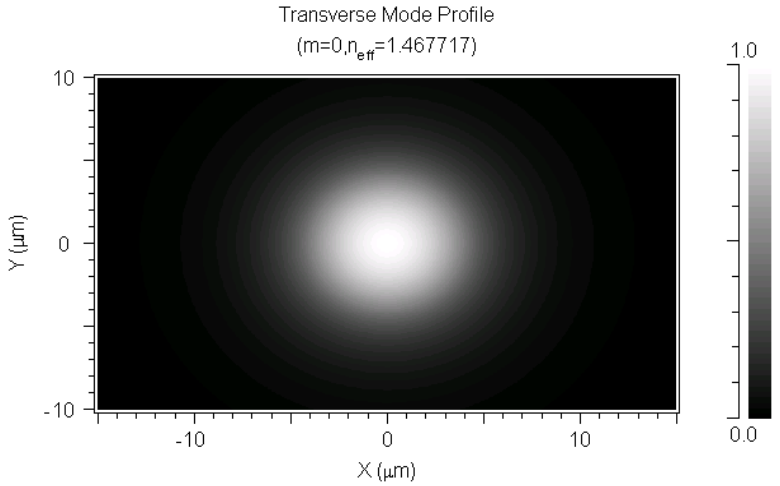

Figure 2.4.3 Mode field amplitude from fiber in Fig. 2.4.2, simulated with BPM

The real amplitude of the output electric field is normalized so that the maximum amplitude within the simulation window is one. For the fundamental mode of this fiber, 75.9% of the optical power is confined to the core region. We also examine the BPM model when a fiber has been chemically etched to remove the cladding and a portion of the core. The ultimate diameter of the fiber is 5μm and the n=1.465 cladding has been replaced by a concentric layer of water (to simulate bulk liquid solutions). Figures 2.4.4 and 2.4.5 show the modified design and the BPM solution of the modified fiber's fundamental mode.

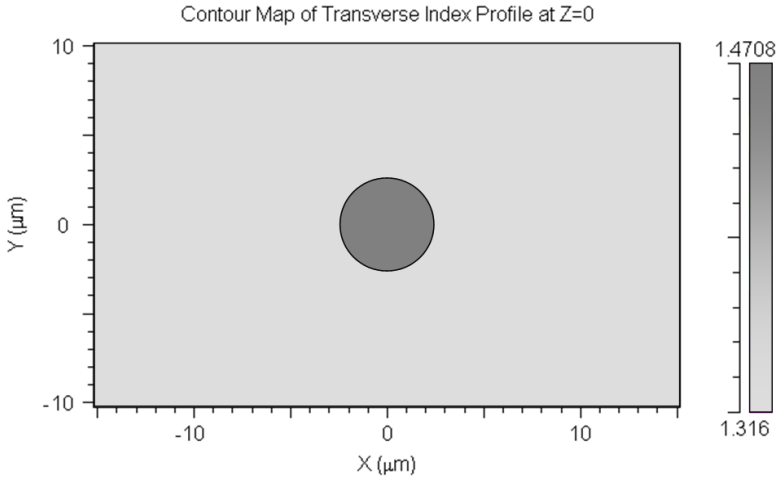

Figure 2.4.4 Index profile of an etched standard SMF fiber. Diameter = 5μm.

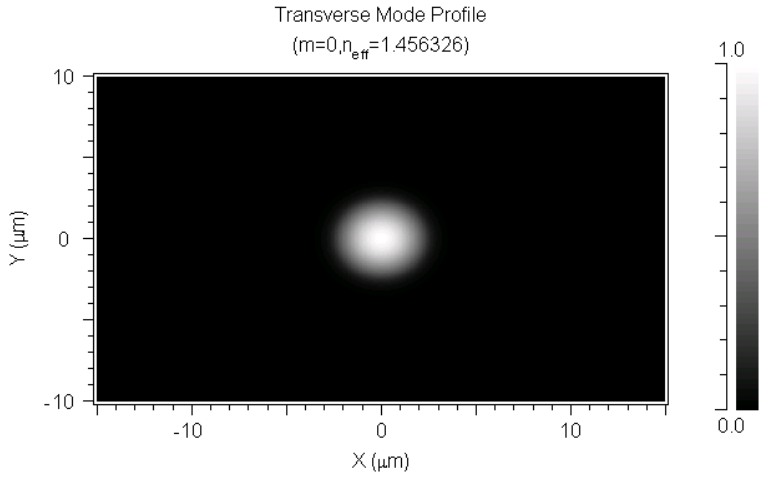

Figure 2.4.5 Mode field amplitude from fiber in Fig. 2.4.4, simulated with BPM

The etching of the cladding and core in the aforementioned fiber is necessary to make the fiber's effective index more sensitive to changes in the surrounding index. In this model, a surrounding layer of low refractive index is designed to be uniform and concentric around the fiber. The Helmholtz equation in Eqn. 2.3.2 indicates that the effective index of the waveguide depends on the amplitude of the electromagnetic field in each region. For this reason, effective refractive index is most heavily influenced by regions where the field amplitude is largest. For the etched fiber, 78.1% of the light is contained within the core. Compared to the 8.2μm fiber, an additional 2.2% of the mode is contained within the evanescent field that penetrates into the region outside of the fiber core. In addition to thinned fibers, multimode fibers demonstrate this phenomenon of greater index sensitivity. Models for multimode fiber are explored in the following section.

2.4.2 Multimode Model

Figure 2.4.5 shows the BPM solution of an altered SMF and how it may exhibit multimode characteristics and a unique propagation constant. The fiber design follows the specifications of a reduced-diameter germanosilicate fiber surrounded by a low bulk refractive index. The fiber diameter must be reduced in order to support a higher order mode. In this simulation, the excitation field contains elements of the first higher order mode.

$n_{core} = 1.4708$	$D_{core} = 5\mu m$
$n_{cladding} = 1.316$	$D_{cladding} = 125\mu m$

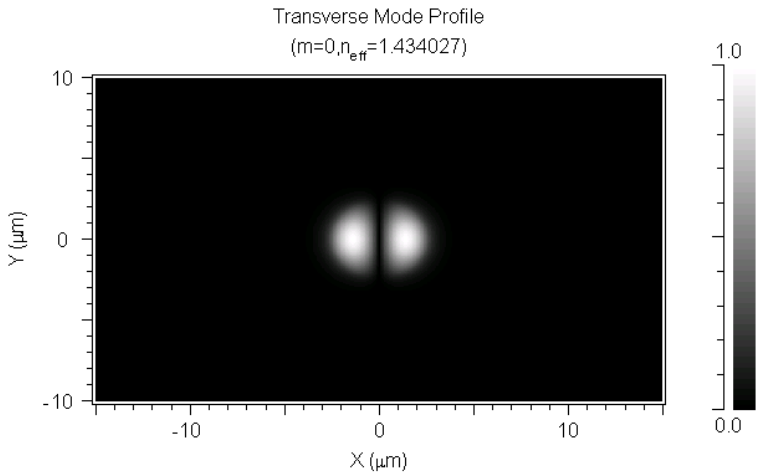

Figure 2.4.6 First higher order mode field amplitude from etched fiber single mode fiber, simulated with BPM

The fundamental mode solution exists for this fiber and was shown in Section 2.4.1. We note that the effective indices of the fundamental and higher order modes are 1.456326 and 1.434027, respectively. The higher order mode exhibits a lower effective index due to the amplitude of the optical field being stronger further into the low refractive index environment. BPM models provide information about the how effective index changes with changes in the surrounding index for each distinct mode. Figure 2.4.7 compares the change in effective modal index as the surrounding index is varied.

We observe that the effective index is more sensitive to changes in the surrounding index for higher order modes and when the fiber diameter is reduced. For this reason, a thinned fiber exhibits ideal characteristics as a refractive index sensor. Others have show that side-polishing [Ref. 2.4.3] and fiber micro-bending [Ref. 2.4.4] take advantage of evanescent fields leaking into the cladding or surrounding material, while wet chemical etching enhances the modes access to the bulk refractive index solutions.

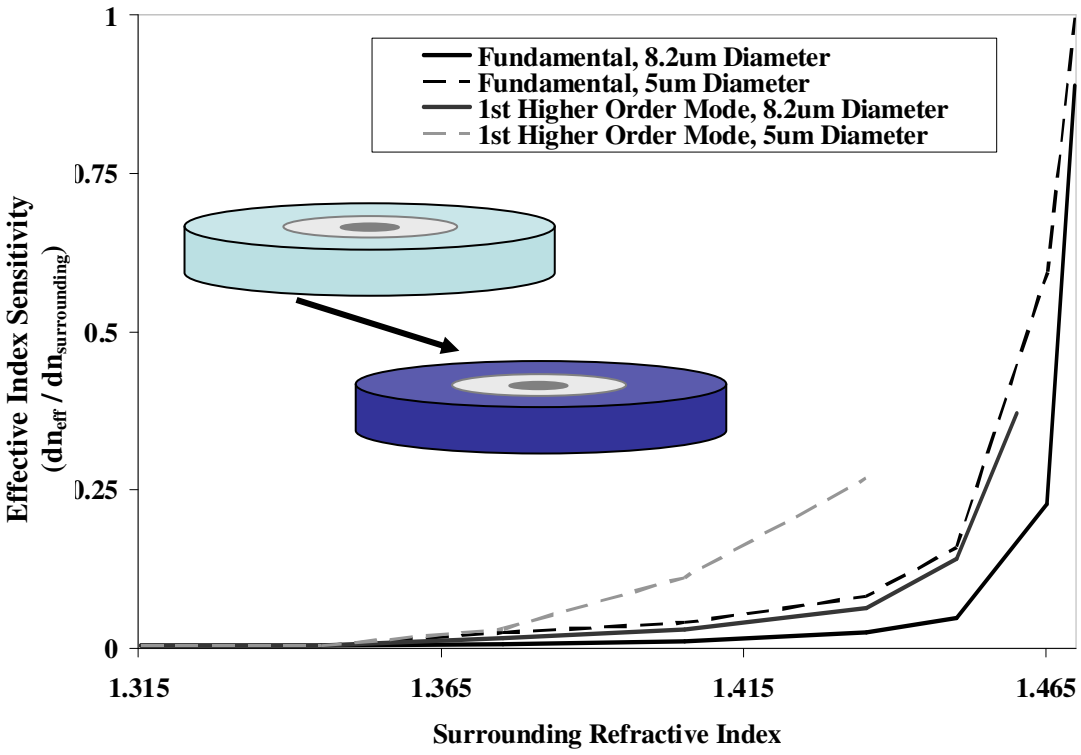

Figure 2.4.7 Plots of the effective index sensitivity between the index of water and the fiber core index. Cartoons depict a fiber cross section.

The fiber may be slowly etched with buffered hydrofluoric acid over a period of hours in order to reduce the fiber diameter without enhancing surface roughness and scattering losses. Figure 2.4.8 demonstrates the effect of etching through the fiber cladding and into the core, replacing the high index of silica with the low index approximated by n_{water} at 1550nm.

The core and cladding dimensions were altered to establish a trend for the effective index sensitivity versus overall fiber diameter. As the cladding is removed, the evanescent wave extends further into the low index etchant, thereby decreasing the effective modal index for the fundamental and first higher order mode. For fiber diameters greater than 40 microns, the fiber will become single mode and the higher

order modes will not propagate. Figure 2.4.8 verifies that the effective modal index is greatly influenced by the more deeply penetrating evanescent field of the higher order mode at all fiber diameters, but particularly for sub-core diameters.

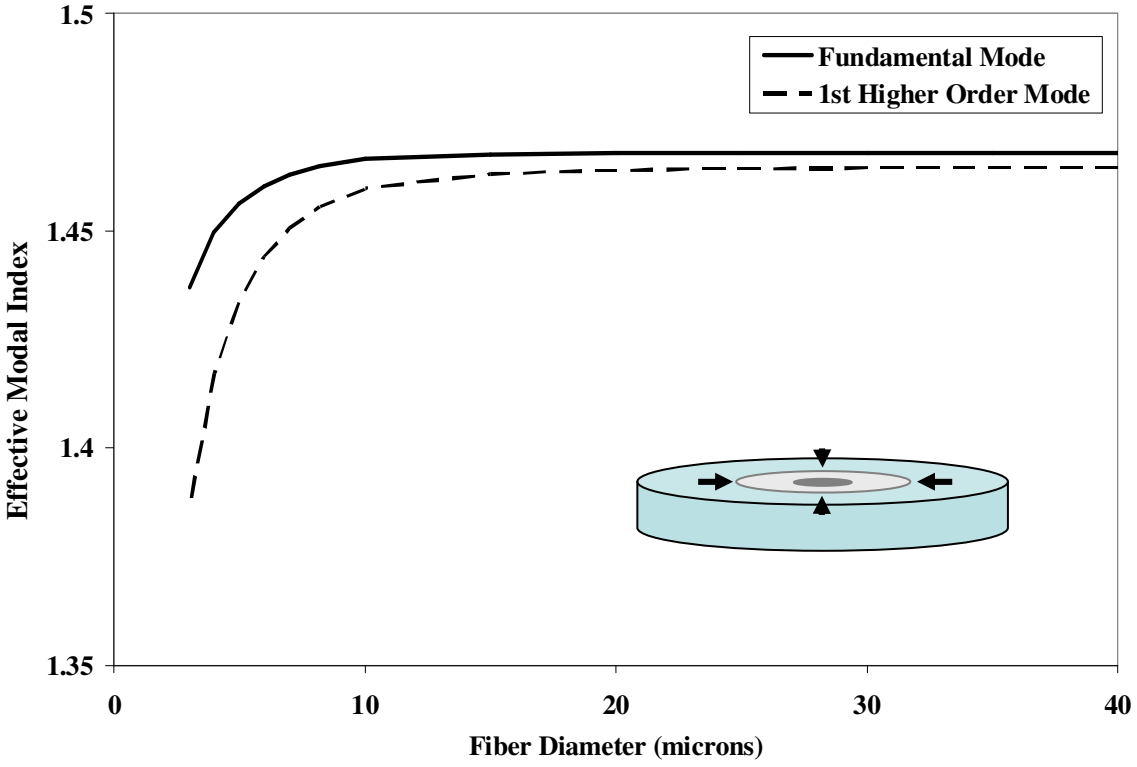

Figure 2.4.8 Study of the effect of etching on the effective index for both the fundamental and first higher order mode. Cartoon depicts a fiber cross section.

2.4.3 Example of a Single Mode Model: The Layered Model

When calculating the shifts in effective index for a single thin layer adsorbed to the fiber surface, a new multilayer model is required. The effective modal index will only be altered by a layer of material on the fiber surface if the evanescent field enetrates into the layer. Therefore we must consider a fiber where the cladding is removed enough

for the field to be nonzero at the fiber surface. Moving from the inner to the outer region, we go from the core, to the cladding (if present), to the adsorbed layer, and finally to the bulk index background layer.

In the context of the adsorbed monolayers that will be discussed later in this thesis, the layers of the adsorbed layer will be between 1-100nm thick. To ensure that the BPM method converges within such thin layers it is necessary to reduce the grid size to between 0.1-1nm, depending on the smallest layer thickness. In order to drastically reduce the computation time from a 3-dimension BPM simulation (transverse grid sizes ~ 10nm), the fiber's azimuthal symmetry was utilized to create a 2-dimensional BPM simulation. This method excludes the higher order modes that do not exhibit azimuthal symmetry. In conclusion, the indices, input fields, and output fields are defined along a single radial dimension.

The background index represents the bulk solution that immerses the fiber. We consider homogeneous mixtures to have a single refractive index. The index of refraction derives from the linear susceptibility of a material and the interaction between molecule dipole moments and electromagnetic radiation. Polarizability is proportional to the volume density of the dipole moments and therefore the material's electric permittivity. Since the electric permittivity is proportional to the square of the refractive index, the bulk index of uniform mixtures is determined by the following equations:

$$\vec{D} = \varepsilon\vec{E} = \varepsilon_0\varepsilon_r\vec{E} = \varepsilon_0(1+\chi_{linear})\vec{E} = \varepsilon_0\vec{E} + \vec{P} \qquad (2.4.4)$$

$$\varepsilon_r = n_{bulk}{}^2 \qquad (2.4.5)$$

$$\varepsilon_r = \sum_i \varepsilon_{r,i} X_i \qquad (2.4.6)$$

$$n_{bulk} = \sqrt{\sum_i n_i^{\,2} X_i} \qquad (2.4.7)$$

where $\vec{D}$ is the displacement field, ε_0 is the permittivity of vacuum, ε_r is the dimensionless relative permittivity, χ_{linear} is the linear susceptibility of the material, $\vec{P}$ is the dipole moment per unit volume, and X_i represent the mole fraction of the i^{th} component of a mixture.

The refractive index of commonly used solvents and solutes are listed in Table 2.4.1. Solute indices are from adsorbed surface layers.

Substance	Refractive Index @ λ=1550nm
water	1.315
ethanol	1.346
silanes	1.42
Concanavalin A	1.45

Table 2.4.1

Refractive indices of solutions and solutes were experimentally determined by our etched fiber sensor and agree with commonly published values.

In the model below, an adsorbed monolayer with an index of 1.42 and thickness of 10nm surrounds the etched fiber surface. The core diameter is 8.2μm unless the calculation considers an etched core. The grid spacing is uniform and fixed at 1nm. The bulk solution outside of the monolayer is a 1% solution (i.e. a 1%, by volume, solution of 3-aminopropyltriethoxysilane (APTES) in water). For our refractive index fiber sensor, the effective index must change dramatically in order to detect adsorption. To enhance this effect, the fiber diameter is reduced.

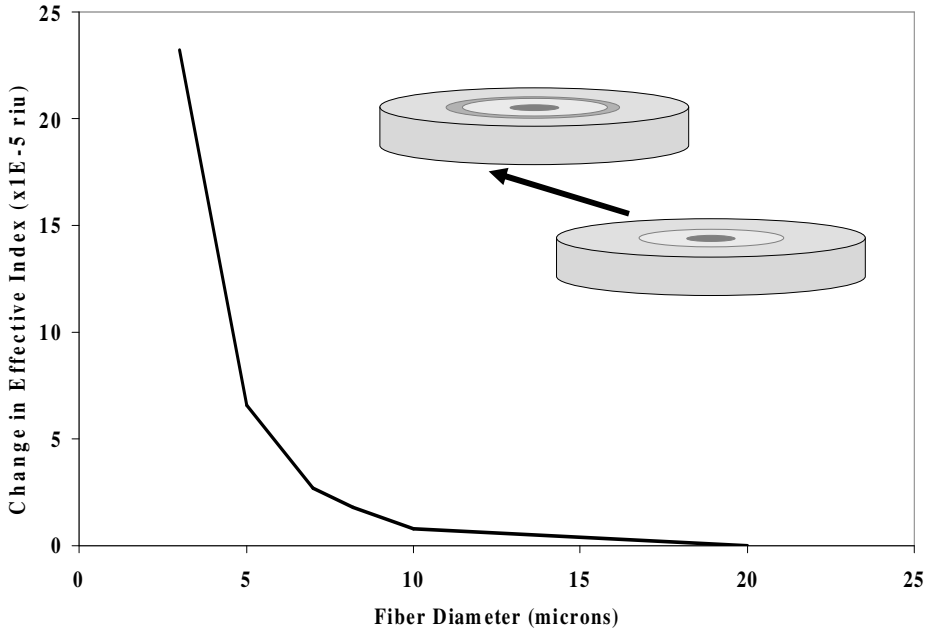

Figure 2.4.9 Effective index shift vs. fiber diameter when an adsorbed monolayer forms on fiber surface.

Chapter 3: Photosensitivity and Fiber Bragg Grating Writing Techniques

When a grating is created in an optical fiber, light incident on the grating will be reflected if its wavelength satisfies the following equation:

$$\lambda_{Bragg} = 2n_{eff}\Lambda$$

where λ_{Bragg} is the Bragg wavelength and Λ is the period of the grating. In order to satisfy the Bragg condition and create an index modulation within the fiber, fabrication must combine adequate photosensitivity with a proper writing technique. While silica fibers with germanium dopants are inherently photosensitive, the potential refractive index modulation increases with the concentration of Ge sites in the crystal lattice. Furthermore, other dopants such as boron and tin may be introduced to further enhance the photorefractive effect. Since the photosensitivity influences the reflectivity of fiber Bragg gratings, it plays a crucial role in the fiber Fabry Perot's finesse and subsequently the minimum index resolution as a refractive index sensor. As photosensitivity peaks in the 240nm range fabrication requires energetic UV sources such as excimer and Argon ion lasers. Holography, prisms, direct-writing and phase masks are typical means of creating the interference patterns within fiber cores. While various techniques have their own limitations and advantages, our in-house fiber Bragg gratings were fabricated with a KrF injection-locked excimer laser, utilizing the phase mask technique.

3.1 Photosensitivity

There are two primary models of photo-induced refractive index changes in germanosilicate fibers: the color center model and the structural change model [Ref. 3.1.1 and Ref. 3.1.2]. When a dopant like Ge is introduced during a metal organic chemical vapor deposition (MOCVD) process, the Ge atoms form bonds with both silicon and oxygen atoms. The Ge-Si bonds strongly absorb UV radiation between 240-248nm. In the color center model, the absorbed UV energy breaks the Ge-Si bond and creates an electron, which is relocalized to a neighboring site. The added electron alters the local linear susceptibility and absorption in the UV. Kramer Kronig relations explain why the refractive index shifts for non-UV radiation (e.g. infrared). If, instead of relocating to a neighbor, the freed electron mobilizes and vacates the vicinity of the recently damaged Ge-Si bond, the region structurally conforms accordingly. This is the structural change model. Compaction and relaxation of the crystal lattice causes microscopic changes wherever the lattice absorbs UV light, thereby changing the macroscopic index of refraction. Both models have been substantiated with various results; neither excludes the other, and the overall effect is thought to be a combination of both.

Additionally, Ge-O defects may absorb UV radiation and augment photosensitivity. During fabrication, the fiber composition depends on the atmospheric composition and conditions. If the environment is pressurized nitrogen or hydrogen, for example, the oxygen sites are replaced by atoms of the environmental gas and defects are formed. UV radiation interacts with these oxygen-deficient hole center (OHDC) defects and photosensitivity improves. The OHDC effect is proportional to the germanium concentration [Ref. 3.1.3].

3.2 Co-doping for Enhanced Photosensitivity

Germanium doping enhances the intrinsic photosensitivity but also increases the refractive index of the silica. For communications fibers, the refractive indices of the core and cladding and numerical aperture are standardized. Increasing the photosensitivity with Ge doping is done at the expense of coupling losses with communications fiber. This is a less than ideal consequence that can be fixed by co-doping. Co-dopants also alter the refractive index while impacting the photosensitivity and can enhance several mechanical properties of the fiber (e.g. thermal resistance).

Hydrogen-loading occurs at both high and low temperatures and relies on the previously mentioned formation of oxygen deficient defects to augment photosensitivity. Standard single mode fibers are conditioned by maintaining a pressurized hydrogen environment over a period of days. A drawback to this method is the strong absorption near the 1550nm communications window that arises due to O-H bond formation. Also, hydrogen loading increases the index of silica [Ref. 3.2.1] and does not fix the coupling losses associated with germanosilicate fibers.

Boron co-doping reduces the refractive index of the germanosilicate while enhancing photosensitivity. Fiber indices may be matched with high concentrations of germanium as long as the boron concentration is sufficient. Birefringence occurs in boron co-doped fibers as stress between regions of high and low concentrations of boron have severe lattice constant mismatches. To contain the photosensitivity within the fiber core, different concentrations of dopants are added in the core than in the cladding and thus the core to cladding interface is stressed. The core then becomes elliptical. The elliptical shape causes internal stress within the core region where the crystal becomes

uniaxial. It is believed that, unlike hydrogen loading, compaction and relaxation are the dominant photosensitivity mechanisms and not oxygen deficient defects [Ref. 3.2.2]. Boron co-doping is limited by absorption within the 1550nm window and the Newport F-SBG-15 fiber has loss values of approximately 0.1dB/m.

Tin co-doped sensors exhibit similar photosensitivity as those doped with boron. While the induced refractive index changes are more stable in time and temperature cycling [Ref. 3.2.3], the fiber's refractive index cannot be compensated for index shifts due to germanium doping as with boron.

The two sensors described in this thesis have displayed different levels of photosensitivity. Photosensitivity measurements are often quantified by the growth of fiber Bragg gratings. As the UV exposure increases, the index contrast between illuminated and non-illuminated regions grows and gratings become stronger. This describes the creation of Type I gratings. While writing Type I gratings, one may only assume that the grating reflectivity is proportional to exposure if the measurement techniques are equivalent. Numerous factors may influence the apparent index contrast, including mechanical stability (of the fiber, UV beam, and optical components) and coherence of the UV beam. For strong gratings, reflectivity is proportional to index contrast. For strong gratings, reflectivity is proportional to index contrast.

3.3 UV Sources

The coherence and beam quality of UV sources vary widely. While not every technique requires coherence, high coherence sources make some techniques for FBG fabrication possible. Some lasers naturally emit light in the proper UV spectrum while

others require frequency doubling crystals to convert the output into the UV. The following sections briefly compare three types of lasers typically used by the FBG industry for manufacturing gratings.

3.3.1 Pumped Dye Lasers

Meltz, et al first implemented the excimer-pumped dye laser for writing FBGs in germanosilicate fibers [Ref. 3.3.1]. The output wavelength of the dye laser was between 486-500nm and so a frequency-doubling BaB_2O_4 crystal was placed at the output in order to downshift to 244nm. Frequency-tripled Nd:YAG and XeCl excimer lasers frequently serve as the optical pump of various dyes. Rhodamine 6G and Rhodamine B are commonly used dyes that produce higher quality beams and efficiency. These dye lasers can be made to exhibit high spatial and temporal coherence.

3.3.2 Argon Ion Laser

Argon ion laser radiation is extremely narrow and useful for grating fabrication techniques where coherence length and alignment may be more challenging. Coherence lengths of these lasers may be on the order of centimeters while the main drawback is that the light must be converted to the 240nm-UV range with a frequency doubling crystal. Argon ion lasers are operated in CW mode and tend to be very robust sources [Ref. 3.3.2].

3.3.3 Spectrally Narrow Excimer Lasers

Our grating fabrication is accomplished with a Lambda Physik LPX-250T excimer laser. The current configuration uses KrF, though the laser may also be used as an ArF laser. ArF has a wavelength of 193nm, which is not typically used for FBG fabrication in germanosilicate fibers due to low absorption at that wavelength. The LPX-

250T is an example of a spectrally narrow excimer laser. It has a tunable range between 247.9nm and 248.7nm, a linewidth of 3pm and a pulse width of 20ns [Refs. 3.3.3, 3.3.4].

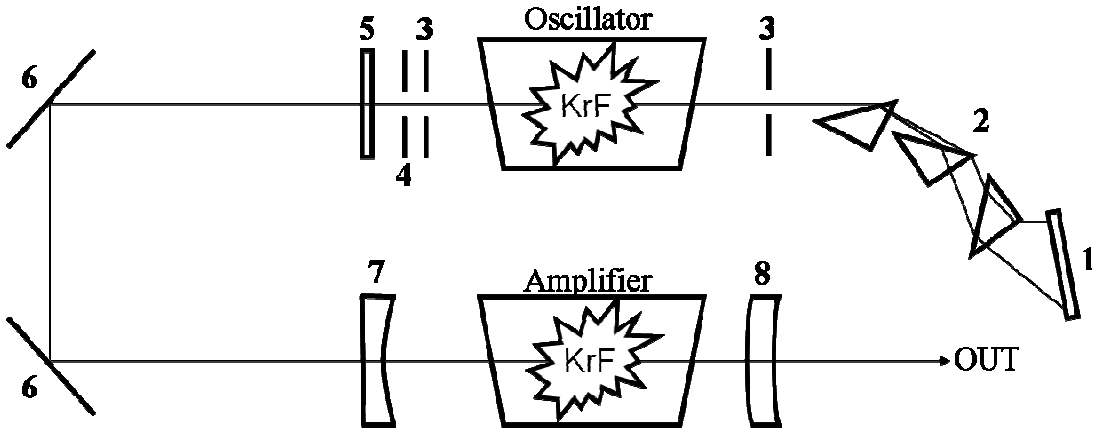

1 Grating – 600 lines/mm
2 Prisms for Spectral Filtering
3 Apertures
4 Iris Aperture
5 30% Refl. Output Mirror
6 Deflecting Mirror
7 Concave Mirror (R=3m)
8 Meniscus (R=0.225m)

Figure 3.3.1 Lambda Physik LPX-250T schematic of optical system

Different laser designs will result in different spectral profiles. The LPX-250T has a tunable range of nearly 1nm and therefore an unfiltered linewidth greater than that. Different schemes have been devised in order to reduce the output linewidth of these lasers. Diffraction gratings and prisms are both used in the LPX-250T. A series of angled prisms sends the fully broadened beam to a diffraction grating, which then reflects different wavelengths at different angles. The angular dependence is important because the grating-reflected beam then passes through the prisms again, where the prisms spatially filter the majority of the beam. A narrow portion of the beam passes through the oscillator cavity again for amplification. The prisms cause amplification of a spectrally narrow beam. The LPX-250T is an injection locked excimer laser. Injection locking is the process in which a stronger, less coherent amplifier receives the output of a weaker,

more coherent oscillator cavity in order to produce a more coherent beam without degrading its intensity. In Fig. 3.3.1, the laser schematic shows two cavities: an oscillator and an amplifier. Let us consider the optical path beginning from where the light pulse leaves the diffraction grating. A spatially and spectrally broad beam leaves the grating and enters the prisms, where it becomes spatially and spectrally narrow. Subsequently amplified by the gain medium of the oscillator cavity, some of the light is then reflected backward and follows the inverse path while some of the light is sent to the amplifier cavity, which contains two deflecting UV mirrors set at 45° each. While in the amplifier, the beam experiences gain within an unstable resonator. The output is sent through a unique window which has been coated to enhance reflectivity at the center but allows the UV light to pass in a halo shape around the center. There are a number of parameters (discharge timing delay, applied voltages, repetition rate) that affect the locking efficiency of the pulses, though the system is quite stable after the first 10 output pulses for a wide range of settings. The LPX-250T uses injection locking to make the output more coherent. This laser suits our grating fabrication because it provides adequate coherence for the phase mask technique of grating fabrication. Also, the output fluences are sufficient to saturate the photorefractive effect in the photosensitive fibers.

The energy leaving the laser is approximately 375mJ per pulse when the gas chambers have been recently refilled. Apertures help to spatially filter the beam to select the smoothest beam profile portion. This filtering causes the input into the FBG writing set-up to be closer to 75mJ per pulse within a 10mm by 5mm beam spot. Laser fluence has been measured to decrease by approximately 15% after 10,000 pulses. The fluence used to write gratings is between 300-550mJ/cm^2 after the UV beam passes through a

beam-shaping aperture and a cylindrical lens, and then is partially reflected from the back facet of the phase mask. With these fluences, which are nearly at the damage threshold of the Newport boron co-doped fiber, the LPX-250T should be a sufficient source for FBG fabrication even though some concerns about the beam profile exist.

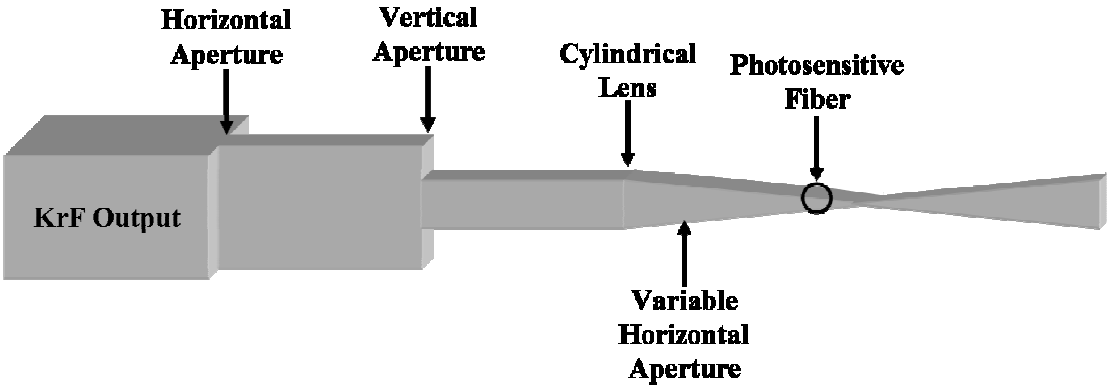

Figure 3.3.2 Top-down perspective view of the apertures and cylindrical lens between the KrF output and the photosensitive fiber. The circle represents a fiber cross-section, though not to scale

3.4 Grating Writing Techniques

There are two primary writing techniques for Fiber Bragg grating fabrication: optical interference and direct-write. The first technique overlaps coherent modes from a UV source in such a way as to create an intensity modulation within the fiber core. Since the photorefractive effect depends on intensity, the induced index modulation matches the intensity profile. In the direct-write technique, the fiber is exposed with a single UV beam spot once per grating cycle repeatedly throughout the grating length. While the direct-write technique is more adaptable than the phase mask technique, it also requires greater mechanical stability and precision alignment. Loosely speaking, a phase mask is a flat silica slide that has a corrugated grating structure permanently etched onto one side. In contact-mode phase mask fabrication, the permanent phase mask structure limits the range of design parameters for FBG production, such as frequency chirping, length, and exposure time.

3.4.1 Holography Technique

The technique that is most sensitive to alignment splits a single UV beam into two and then recombines them within the fiber core. The beam splitting technique sends two beams into paths whose lengths must be within L_c of each other, where L_c is the coherence length of the laser. Typically, an injection locked excimer laser will have a coherence length of 1cm. In addition to matching the beam paths, the optical components that direct the beams must be stable within less than a period of the index modulation. For our example, the Bragg wavelength is approximately 1550nm and the modal index is 1.45, so the fiber must be stationary much better than 500nm!

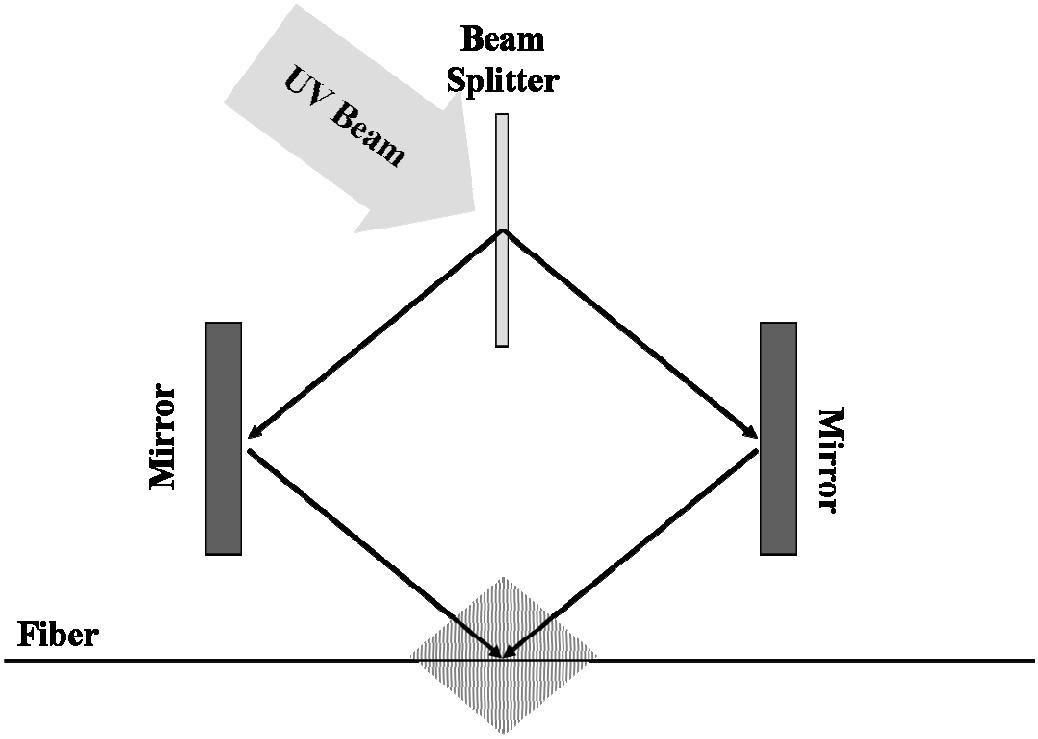

Figure 3.4.1 Diagram of a typical set-up for fabricating FBGs with holography.

Thermal expansion is discussed in Section 4.3.1, which will show that temperature gradients could be catastrophic to the writing process, not to mention vibrations and air currents. Fig. 3.3.1 depicts a typical set-up for this technique. In the beginning of our

work, this technique was briefly attempted because the optical components (e.g. mirrors and beam splitters) were readily available and the pitch and length of the gratings were more flexible. By changing the beam spot sizes and the angle between the recombining beams, the grating lengths and Bragg wavelengths could be tuned.

$$d = \frac{248nm}{2\sin\varphi} \qquad (3.4.1)$$

Eqn. 3.4.1 shows how the grating period d depends on the wavelength of the incident light and the angle between the overlapping beams. The overlapping beams had to be in phase and so the +/- 1 order modes were used. Eqn. 3.4.1 also indicated that holography requires a high level of spectral coherence in the source. If the Lambda Physik LPX-250T's injection locking elements were removed then the sudden reduction in coherence would provide a poor source for fabricating gratings by holography.

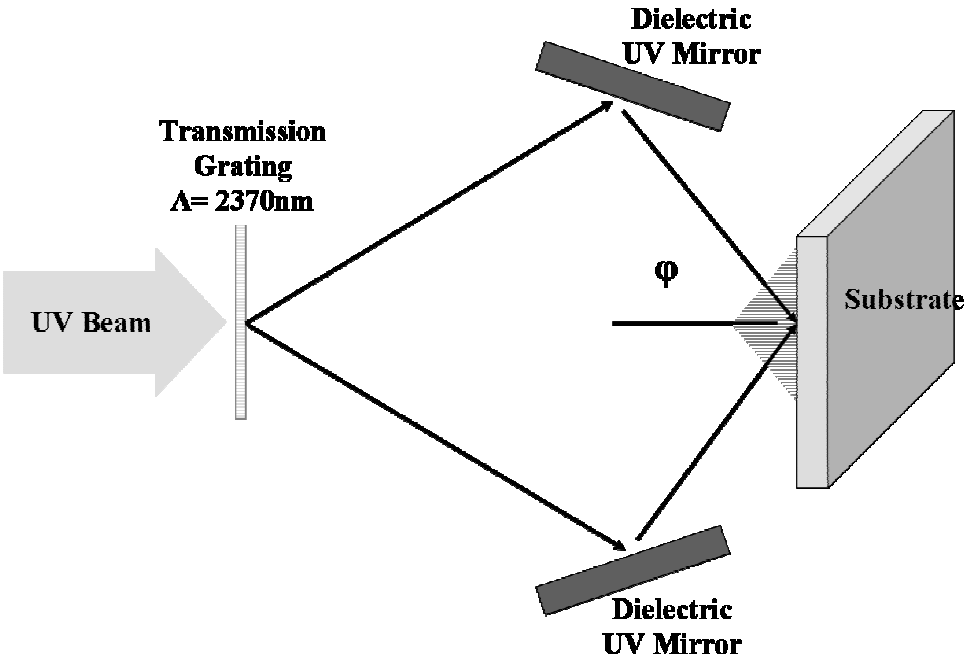

Figure 3.4.2 Diagram of holography set-up used to exposed a silica substrate coated with photoresist. Planar Bragg gratings were created.

In early experiments we attempted to create many-exposure corrugation gratings on a silica substrate coated with Microchem SU-8 photoresist. The absorption of 248nm UV radiation was large and the laser fluences were sufficient (45mJ pulses within 0.5cm x 1.25cm beam spots) to ablate thin layers of resist. One of these structures was created and analyzed with atomic force microscopy. The grating structure could be seen with the naked eye and it appeared that the corrugation was washed out after more than a few exposures. The AFM image below shows that an ablation pattern with Λ=1022nm and 142nm depth was created with a single shot.

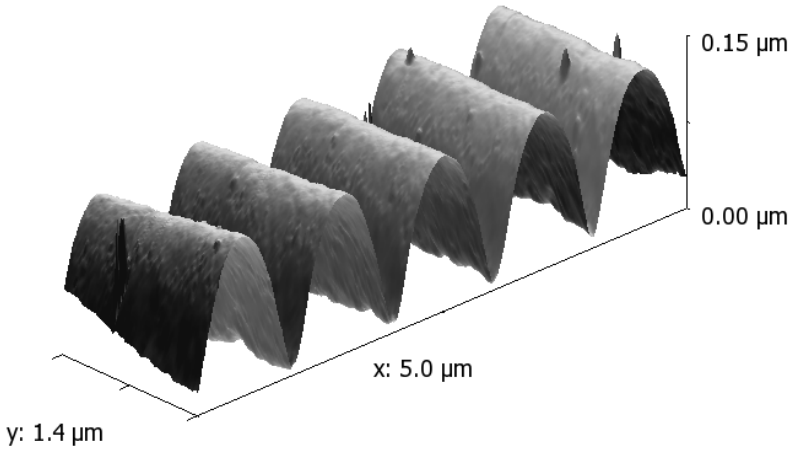

Figure 3.4.3 AFM microscope image of the ablated surface corrugation in SU-8

This relief pattern was initially designed to couple 1550nm light at normal incidence into the planar silica and resist structure and therefore has a different wavelength than fiber Brag gratings. A HeNe laser was used to interrogate the grating during the writing procedure to monitor the Bragg wavelength and grating strength. The set-up is depicted in Fig. 3.4.4.

The power diffracted into the detector did not increase monotonically with the number of exposures and within 10 pulses the grating structure was permanently removed. Instability in the set-up is a typical problem with the holography method of

writing fiber Bragg gratings. We chose to switch to the phase mask technique because of the loosened requirements for mechanical stability and coherence.

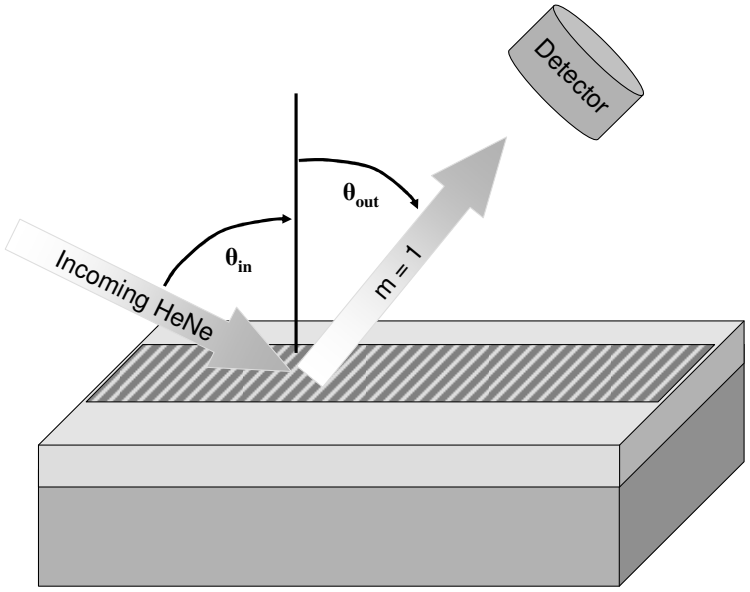

Figure 3.4.4 Surface grating interrogation set-up to monitor grating strength while writing gratings

While still employing holographic means to inscribe a fiber grating, two other techniques requiring less mechanical stability can be used. Fig. 3.4.5 shows two cartoons of simpler methods. Both techniques fold the first order beam upon itself in order to create the intensity pattern. Both require the components (i.e. mirror and prism) to be within a coherence length of the fiber, though the beam paths are inherently equal in length. It is critical to have angular control of the beam and/or optical component in each set-up to ensure that the interference pattern overlaps with the fiber. In both examples, excellent mechanical stability is also required between the optical component and the fiber. Any position drift will result in blurring of the index modulation and a weakened grating.

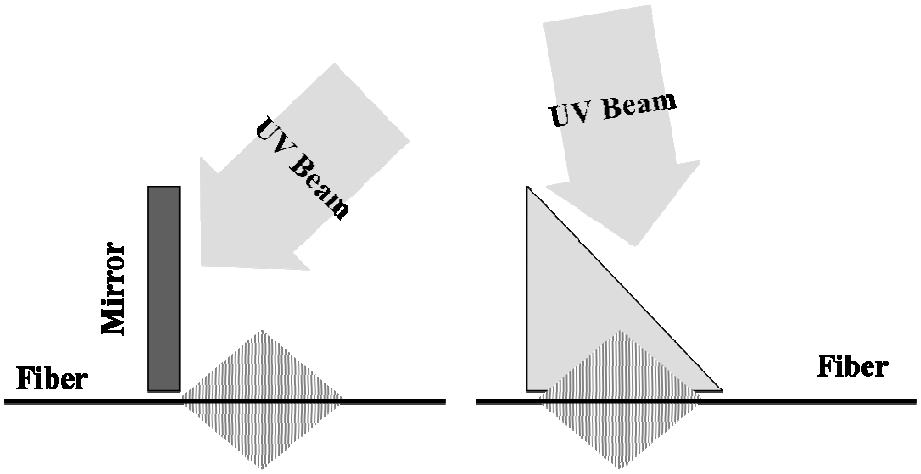

Figure 3.4.5 Holography writing set-ups using (a) a Lloyd mirror and (b) a prism to overlap different portions of the same beam.

3.4.2 Point-by-Point Writing Technique

The most common technique that does not employ an interferometric set-up relies on point by point inscription of the index modulation.

With the point by point writing scheme, the fiber is securely mounted onto a precision translation stage. The goal is to create a periodic array of high index regions with control over the induced refractive index shape and profile. The Bragg condition states that the period of the fiber modulation must be $\Lambda=\lambda/2n_{neff}$, where in the point by point method, the laser spot incident on the fiber will be spaced by $\Lambda/2$. Laser pulses expose the fiber then a translation stage moves the fiber or the beam along the axis and repeats the procedure. The acceleration of the translation stage and the intensity of the beam may be used to create nonuniform grating structures. Apodization is a technique which makes the coupling strength of the fiber a function of the distance along the fiber. This may be advantageous if side lobes need to be suppressed, as in FBGs for communications filters. Lastly, the length of the grating is determined simply by the

length that the fiber may be translated with sufficient precision. With potentially long gratings, the reflectivity values are only limited by grating uniformity and the induced index contrast.

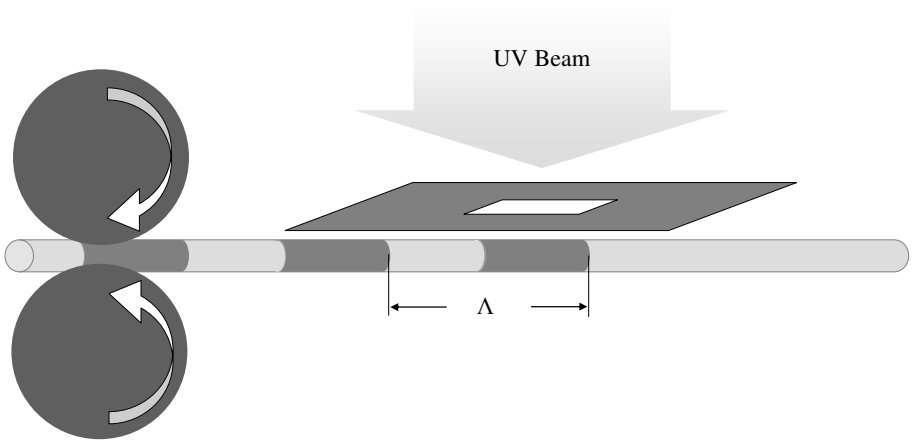

Figure 3.4.6 Direct-write set-up in which an amplitude mask shapes the UV light that exposes the grating. Fibers are typically mounted on spools that move the fiber precisely.

3.4.2 The Phase Mask Technique

Fabricating phase masks requires the ability to make large area uniform corrugations on fused silica. UV holography and electron beam lithography are the two primary means of accomplishing this objective. Holography tends to be the preferred method because large electron beam lithography patterns introduce stitching errors into the phase mask that create spectral flaws in FBGs. An oft-mentioned benefit of large-area phase masks is the ability to fabricate many FBGS at one time. While holographic methods allow for chirping, the E-beam lithography method allows for both the corrugation duty cycle and period to be customized for every period along the mask. Whether by holography or lithography, the grating pattern is transferred to the fused silica substrate so that the pattern may be etched. Anisotropic etching creates a preferred

surface relief pattern, maximizing diffraction into the +/-1 modes. Reactive ion etching creates anisotropic corrugations. Design specifications will be discussed later in this section in the context of contact mode FBG fabrication.

UV beams may be overlapped in any number of ways in order to create an interference pattern. The phase mask is one of many tools that may split a UV beam in order to create interference. For example, Fig. 3.4.7 shows how a phase mask acts as a beam splitter in a holography set-up. The advantage to replacing the beam splitter is normalization of the beam path lengths. The phase of the beam that passes through the beam splitter is retarded due to passing through the beam splitter. An adjustment to one of the beams, after passing through the splitter, ensures that the overlapping beams are in phase and therefore interfere properly. Introducing a phase mask does not put the beams out of phase with one another and therefore a symmetric set-up may be utilized. For this phase mask, the corrugation wavelength is not critical because the two mirrors may be rotated in order to produce a variable grating wavelength.

Unlike the technique that we employ, the phase mask is separated from the fiber and the undiffracted, zero-order beam may be physically blocked. The m=0 beam does not contribute to the strength of the grating but changes the effective modal index of a photosensitive fiber. Blocking the m=0 beam ensures that the photosensitivity does not saturate before maximum index contrast is achieved. If the phase mask technique is performed in contact mode the phase mask must be more carefully designed in order to reduce the effects of the undiffracted zero-order beam.

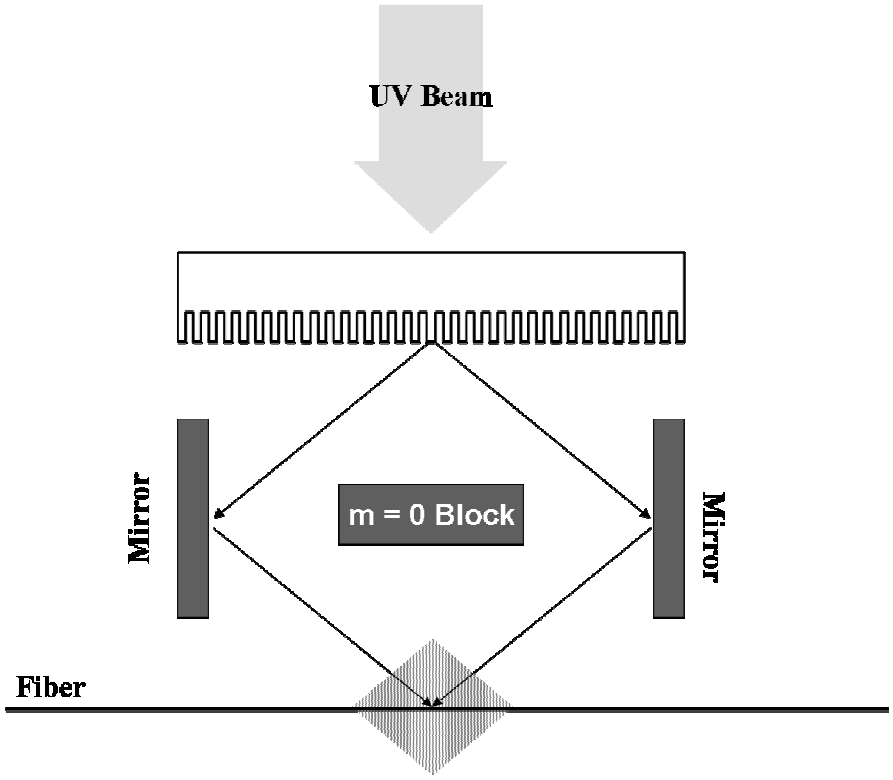

Figure 3.4.7 Phase mask set-up that recombines the diffracted first-order modes with parallel mirrors and blocks the zero-order mode directly.

Phase masks designed for contact mode fabrication of fiber Bragg gratings are specifically designed to make one type of grating with almost no opportunity to change the characteristics. The UV interference pattern from a phase mask is constant, given that the incident angle and wavelength are constant. To change the induced index modulations, different techniques can be used to alter the fiber position, angle, bending, and tension, among other quantities. The phase mask pitch is designed to have twice the modulation wavelength as within the fiber. In order to reflect 1550nm light in a fiber with modal index of 1.45, the index modulation should have a wavelength of 534.5nm and the associated phase mask will have a wavelength of 1069nm. The two first-order diffracted beams will interfere within the coherence length of the UV source. It has been shown that FBG reflectivity decreases when the separation between phase mask and fiber

increases [Ref. 3.4.1]. The diffraction efficiency of each mode type (e.g. m=0, m=+/- 1, etc.) depends on the depth of the corrugation. Zero-order mode suppression enhances index contrast within the FBG region. Without the ability to physically block the zeroth order in contact mode, the corrugation depth may be chosen so that the diffraction efficiency is minimized for the zeroth order.

$$\Lambda_{phasemask} = 2\Lambda_{grating} \tag{3.4.2}$$

$$d = \frac{\lambda_{KrF}}{2(n_{248nm} - 1)} \tag{3.4.3}$$

Phase masks designed to be used with KrF excimer lasers are constructed from fused silica due to the low absorption at $\lambda_{UV} < 300$nm. Nullifying the zeroth order depends heavily on the UV wavelength and the refractive index of fused silica at that wavelength. This condition further constrains the versatility of the phase mask technique. Good phase masks may be able to suppress the zero-order mode so that less than 2% of the total beam power propagates in that direction. The Ibsen Photonics phase mask used in our FBG fabrication only allows 0.58% of the beam in to the m=0 mode. Ibsen estimates the quality of their previous generation of phase masks to have better than 1.5% zero-mode efficiency.

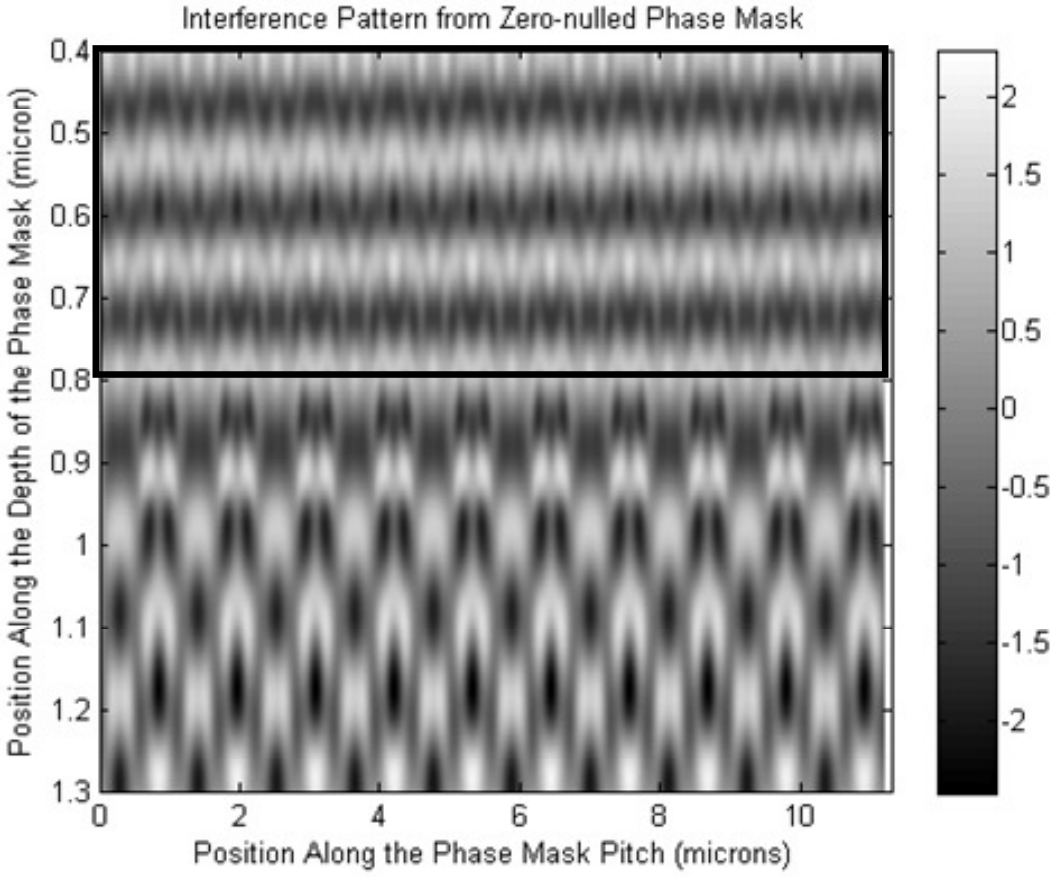

Figure 3.4.8 Plot of electromagnetic wave amplitudes within a zero-mode nullified phase mask and within the 500nm that is adjacent to the corrugation. The boxed region contains the phase mask and the plane wave is launched from the top and propagates downward.

Fig. 3.4.8 is a height-coded map of the electromagnetic radiation emitted by a phase mask with proper pitch and corrugation depth. A simulation tool that uses finite difference time domain (FDTD) simulates how the phase mask converts a normal incidence plane wave into an interference pattern with half of the wavelength. Specifically the FDTD simulation allows for all of Maxwell's time-dependent equations to be solved at every point in space for finite time increments. The boxed region at the top of Fig. 3.4.8 shows the plane waves within the phase mask itself. The grating pitch is oriented from left to right. The weak transverse interference pattern is due to the reflections from the phase mask-air interface. Between 0.8μm and 1.3μm the 248nm

light is free to propagate in air. In the simulation the beam is perfectly coherent both spatially and temporally and therefore the coherence length is not relevant. The wavelength of the simulated beam is 248nm and $\Lambda_{\text{phase mask}}$ = 530nm. The refractive index for silica at 248nm was approximated to be 1.50 [Ref. 3.4.2]. These values are substituted in Eqn. 3.4.3 and the grating depth *d* is calculated to be 248nm. Within 500nm from the phase mask corrugation, the interfering radiation forms an ideal pattern for FBG fabrication. In contact mode, the fiber is placed as near to the phase mask as possible though the pattern must be projected at least as far as the cladding is wide in order to reach the core. Details of FDTD calculations may be found in **Electromagnetic Simulation Using the FDTD Method** by D. M. Sullivan [Ref. 3.4.3].

FBG production by the contact mode phase mask technique relies on mechanical stability between the mask and fiber as well as the UV beam uniformity. Mechanical stability between the interference pattern and fiber index modulation is critical. In contact mode, however, the phase mask and fiber may be mounted on the same stage so that temperature and vibrations impact both similarly. The FBG spectrum may be tuned by applying tension to the fiber during the writing process. When the tension is released the Bragg wavelength shifts due to a contraction of the fiber. If the mounts, typically V-grooves, which maintain tension during the writing process, slip the index modulation becomes blurred and the reflectivity degrades. Lastly, if the UV beam profile is not consistent with respect to the phase mask and the period of the inscribed grating the FBG's index contrast fades out over long exposures. Simulated effects of nonuniform beam profiles are included in Chapter 4.

3.5 Defects and Annealing

The process of inducing refractive index changes within photosensitive inherently generates defects within the fiber. The defects, as discussed in Section 3.2, give rise to the refractive index change according the Kramer Kronig relations [Ref. 3.5.1]. Strongly absorbing OH bonds are frequently treated with a thermal anneal to improve the quality of hydrogen loaded fibers. While more weakly absorbing, boron co-doping enhances the photosensitivity almost as much as hydrogen loading and will have comparable defect formation [Ref. 3.5.2]. Losses due to grating formation may be directly measured by examining how transmission degrades for off-resonance light. On resonance, the average lifetime within the grating increases due to reflections back and fourth within the highly reflective region. Losses due to defects are expected to be even greater for on-resonance wavelengths. Consider now, the Fabry Perot constructed with such lossy gratings. The photon's lifetime within the Fabry Perot is greater than in a single grating and therefore is greater within the grating region. Spectral characteristics of gratings and Fabry Perot cavities deviate from expectation when loss is introduced. Loss within the grating regions must be reduced to analyze the sensing capabilities.

UV damage may also be used to form a different type of index modulation than is discussed in this thesis. These are Type II gratings. These gratings are written with such large energy densities that the induced refractive index must be described by a separate model than the color-center and structural change models mentioned in Section 3.2. If the UV beam used to inscribe gratings is not uniform then there could be local formation of a Type II grating [Ref. 3.5.3]. The localized formation of Type II gratings can be directly attributed to reducing grating reflectivity for high index contrast [Ref. 5.3.4].

Thermal annealing solves the defect loss problems by rearranging the electrons were relocated during the UV exposure. By rearranging the electrons, lossy bonds and lattice deformation both dissipate and cause grating transmission to increase and Fabry Perot throughput to rise. There is an extent to which thermal annealing will be useful for fabricating high finesse Fabry Perot sensors. Literature shows that grating reflectivity is effected by high-temperature, long-duration thermal annealing. The drop in reflectivity is due to the same electron rearranging that helps scattering and absorption. It was mention in Section 3.2 that the structural change model for photosensitivity describes how UV exposure deforms local regions of the silica lattice. Thermal annealing reverses the effect and reverses the induced index contrast. Spectral analysis of loss will be discussed in Chapter 5.

Chapter 4: Fiber Bragg Grating Theory

Bragg gratings are periodic refractive index modulations that reflect light according to the Bragg equation. Fiber Bragg gratings are Bragg gratings whose index modulations are inscribed within the core of a photosensitive fiber. The bandwidth and reflectivity of these spectral filters may be customized to a range of application needs in optical communications, fiber laser fabrication, or, in our case, sensing. We may use a transfer matrix model to analyze how various parameters impact the shape of the FBG spectrum and then tailor the fabrication techniques to suit the demands required by sensing applications. Furthermore, this chapter will examine the impact of surrounding index, temperature, and strain on the standard and etched fiber.

4.1 The Bragg Equation

The condition for light to enter a grating and be reflected back is derived from conserving momentum in the optical signals. The incoming momentum of the optical field within the fiber must be matched by the momentum of the grating and the outgoing momentum of the optical wave.

$$\vec{p}_{incoming} = \vec{p}_{reflected} + \vec{p}_{grating} \tag{4.1.1}$$

$$\vec{k}_{incoming} = \vec{k}_{reflected} + \vec{k}_{grating} \tag{4.1.2}$$

$$\vec{k}_{incoming} = -\vec{k}_{incoming} + \vec{k}_{grating} \tag{4.1.3}$$

$$2\vec{k}_{incoming} = \vec{k}_{grating} \tag{4.1.4}$$

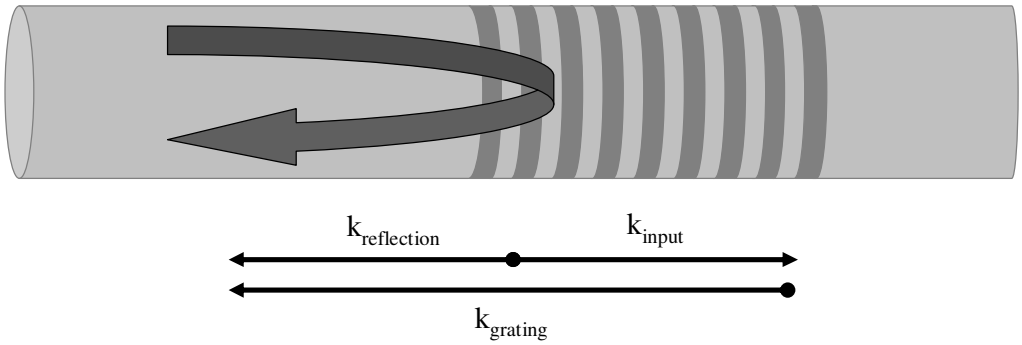

Figure 4.1.1 Momentum conservation for optical signals reflected backward from a fiber Bragg grating. Optical momentum is denoted by the propagation constant *k*

The equations listed above show that fiber Bragg gratings will only reflect the input light if the grating is characterized by twice the momentum of the input light. In terms of wavelengths, the general Bragg condition becomes

$$\lambda_{optical} = 2n_{eff}\Lambda_{grating} \qquad (4.1.5)$$

To reflect one of the main communications wavelengths, λ=1550nm, within the Newport photosensitive fiber (n_{eff} = 1.45), the grating pitch should be 534.48nm. Equation 4.1.5 is essential in understanding the measured quantities in refractive index sensing with etched fiber components. If $\Lambda_{grating}$ is fixed, the wavelength of the reflected light shifts with effective index shifts. The Bragg condition, however, does not tell the whole story about the usefulness of etched fiber sensors. Coupled wave theory is required to theoretically predict the FBGs spectrum and reflectivity.

Coupled mode theory describes forward and backward propagating waves (both amplitude and phase) as they are confined within the fiber's grating region. The initial assumption is that the index modulation follows a raised-cosine pattern, where the index along the fiber can be expressed as:

$$n(z) = n_{core} + \Delta n \cos(k_{grating} z) \qquad (4.1.6)$$

As previously mentioned in Chapter 3, the index contrast, Δn, depends on the writing technique, stability, and photosensitivity of the fiber. With the phase mask technique, the index modulation follows the interference pattern projected onto the fiber core. Counter-propagating waves that interact with a periodic index modulation may be generally expressed in terms of a complex amplitude and phase.

$$E_F(z,t) = F(z)e^{i(wt-\beta z)} \tag{4.1.7}$$

$$E_B(z,t) = B(z)e^{i(wt+\beta z)} \tag{4.1.8}$$

The magnitude of the phase indicates that each of the counter-propagating waves have the same propagation constant. The sign of the phase indicates the direction of propagation. A. Yariv and M. Nakamura first formulated the coupled wave equations that govern how field amplitudes behave when light encounters a periodic modulation [Ref. 4.1.1].

$$\frac{dF(z)}{dz} = i\kappa B(x)e^{-2i\Delta\beta z} \tag{4.1.9}$$

$$\frac{dB(z)}{dz} = -i\kappa^* F(x)e^{2i\Delta\beta z} \tag{4.1.10}$$

By solving these coupled differential equations, amplitudes of the reflected and transmitted waves can be determined in terms of coupling strength, grating length, and input wavelength [Ref. 4.1.2].

$$R(\kappa, L, \lambda) = \frac{\kappa^2 \sinh^2(\sqrt{\kappa^2 - \Delta k^2}\,L)}{\Delta k^2\left(\sinh^2(\sqrt{\kappa^2 - \Delta k^2}\,L) - \cosh^2(\sqrt{\kappa^2 - \Delta k^2}\,L)\right) + \kappa^2 \cosh^2(\sqrt{\kappa^2 - \Delta k^2}\,L)} \tag{4.1.11}$$

If the grating is lossless, then the sum of the reflectivity, R, and transmittivity, T, will be one. Scattering, absorption, and angled index modulations cause the well-confined mode

to leak out of the core or couple into other modes. If light remains in the guide within the cladding, then the optical power remains constant within the waveguide. These cladding modes tend to be supported and reflected at shorter wavelengths than the center Bragg wavelength of the FBG. Non-guided modes are radiative and permanently leak into the environment. According to Eqn. 4.1.11, the grating spectrum broadens for stronger coupling coefficients and/or shortening of the grating. The index contrast Δn, the mode confinement, and wavelength all determine the coupling constant. A general expression for the coupling constant may be derived from K.O. Hill's paper [Ref. 4.1.2].

$$\kappa = \frac{\pi \Delta n \Gamma}{\lambda} \qquad (4.1.12)$$

In Eqn. 4.1.12, Δn is the magnitude of the index contrast and Γ is the modal confinement. For weak gratings, light penetrates through the entire grating and the filter's spectrum is proportional to the grating length. Fourier analysis describes how the spectrum responds to varying degrees of spatial confinement within the grating region. For strong gratings, the width of the FBG spectrum is not determined by the grating length but depends instead on the coupling strength. This coupling strength will depend on the fiber photosensitivity, the writing technique, and the UV source quality.

An apodized FBG spectrum has reduced reflectivity in the side lobes beside the central peak. The process of writing an apodized grating involves reducing the coupling strength on the edges of the grating. Varying the index contrast, Δn, along the fiber axis is typically achieved by varying the UV beam intensity along that direction. Graded amplitude apertures and variable diffraction efficiency phase masks are both used to customize the beam intensity. In the direct write method, the UV power is fixed but the exposure time at each location along the grating is changed.

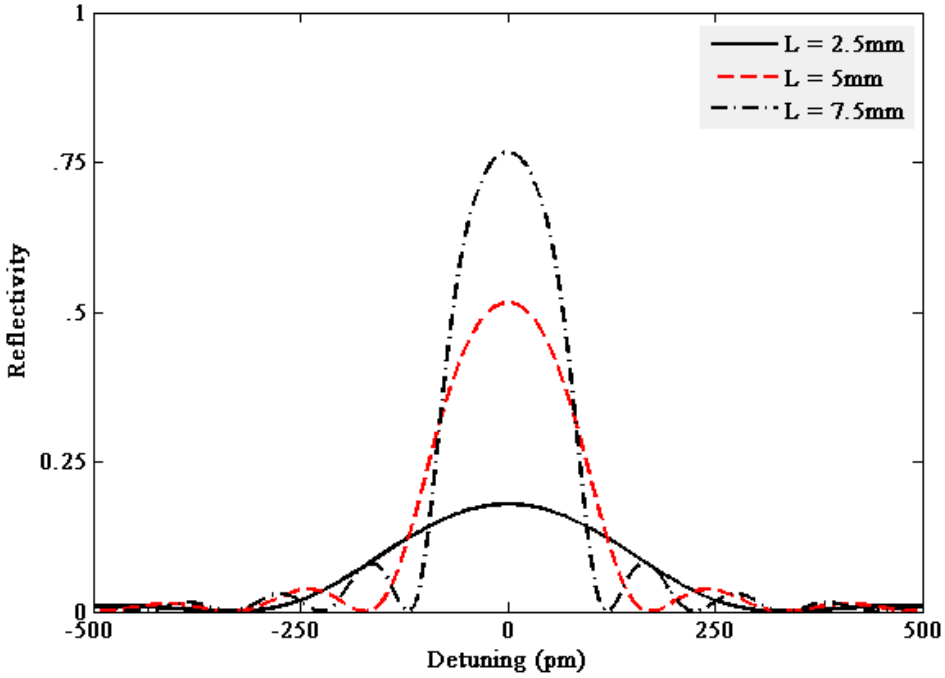

Figure 4.1.2 Plot of the reflection spectrum of a FBG with index contrast of 1e-4. Various grating lengths are plotted. The index contrast was low enough so that the spectra are limited by grating length and not coupling strength.

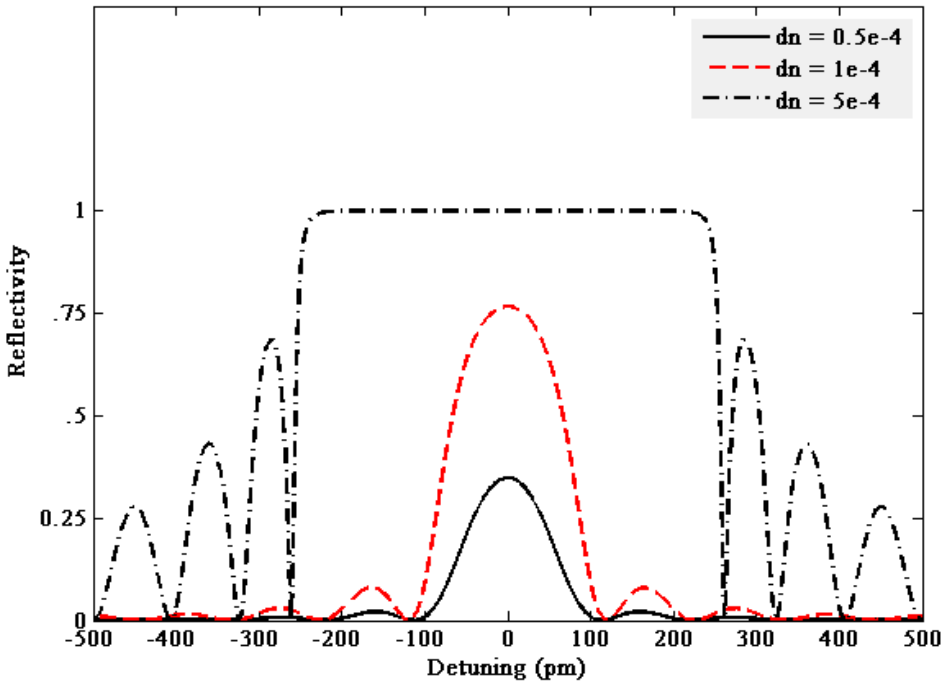

Figure 4.1.3 Plots of the reflection spectrum of a 7.5mm long grating. Various index contrasts are plotted to show that reflectivity and bandwidth increase with the coupling constant.

4.2 Transfer Matrix Simulations

FBG spectra may also be simulated utilizing the transfer matrix method where transmission and reflection matrices can be defined for uniform sections along the grating region. From the coupled mode equations in Eqn. 4.1.9 we may express a transfer matrix as follows [Ref. 4.2.1, 4.2.2, 4.2.3]:

$$\begin{bmatrix} F_0 \\ B_0 \end{bmatrix} = \begin{bmatrix} T_{11} & T_{12} \\ T_{21} & T_{22} \end{bmatrix} \begin{bmatrix} F_L \\ B_L \end{bmatrix} \tag{4.2.1}$$

where F_0 and B_0 are the normalized field amplitudes of the forward and backward traveling waves at the beginning of the grating. F_L and B_L are the normalized field amplitudes at the end of the grating. F_L and B_0 represent the grating transmission and the grating reflection as a function of the detuning from the center Bragg wavelength. The elements of the transfer matrix are solved by using expressions for the counter-propagating waves in Eqns. 4.1.7 and 4.1.8 with the coupled differential equations found in Eqns. 4.1.9 and 4.1.10 [Ref. 4.2.1, 4.2.2, 4.2.3]:

$$\begin{bmatrix} T_{11} & T_{12} \\ T_{21} & T_{22} \end{bmatrix} = \begin{bmatrix} \dfrac{\Delta k \sinh(\kappa L) + i\kappa \cosh(\kappa L)}{i\kappa} e^{-i\beta_0 L} & \dfrac{\kappa \sinh(\kappa L)}{i\kappa} e^{-i\beta_0 L} \\ -\dfrac{\kappa \sinh(\kappa L)}{i\kappa} e^{i\beta_0 L} & \dfrac{-\Delta k \sinh(\kappa L) + i\kappa \cosh(\kappa L)}{i\kappa} e^{i\beta_0 L} \end{bmatrix} \tag{4.2.2}$$

Implementing the transfer matrix method in a Matlab routine provides insight into the spectral features of practical gratings. Gratings with gradual changes in the grating pitch, grating strength, and uniformity may be simulated and analyzed with the transfer matrix method. For example, shallow and low frequency modulation of portions of the spectrum

may be attributed to spikes in the coupling strength within localized regions of the grating.

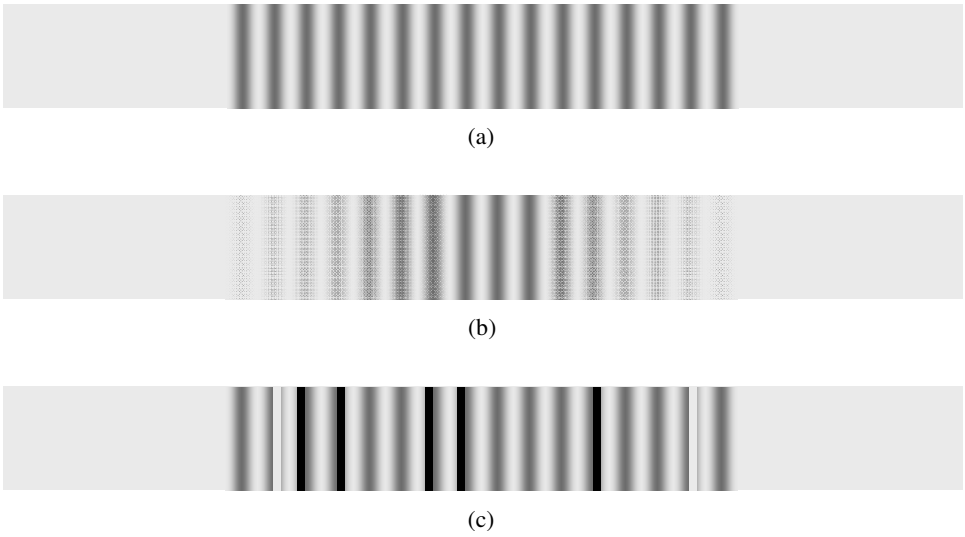

Figure 4.2.1 Fiber Bragg grating index profiles of (a) uniform raised-cosine, (b) Gaussian apodized, and (c) randomly nonuniform patterns

In Matlab calculations, the 7.5mm grating is divided into 100 lengths of 75μm. Each length has equal and uniform periodicity but different coupling strengths and core indices. The plot below shows the reflection spectrum of an unperturbed, uniform grating of length 7.5mm with index contrast of 1e-4 riu and a nonuniform grating spectrum. The latter reveals how the center and side lobes are impacted by increasing the coupling strength in randomly generated portions of the length that consist of 30% of the total grating length. This is intended to simulate nonuniformity in the grating strength that may be caused by a nonuniform UV beam profile. The features to note (see figure below) are the raised side lobes and the irregularity in spacing between the local minima. Both of these characteristics of the spectra are evident in the FBG spectra of our in-house fiber Bragg gratings.

The transfer matrix method is also very effective in simulating chirped and apodized gratings. While we are in the process of fabricating fiber Fabry Perot sensors in our lab, the etched FBG sensor that was used in this thesis has been manufactured and

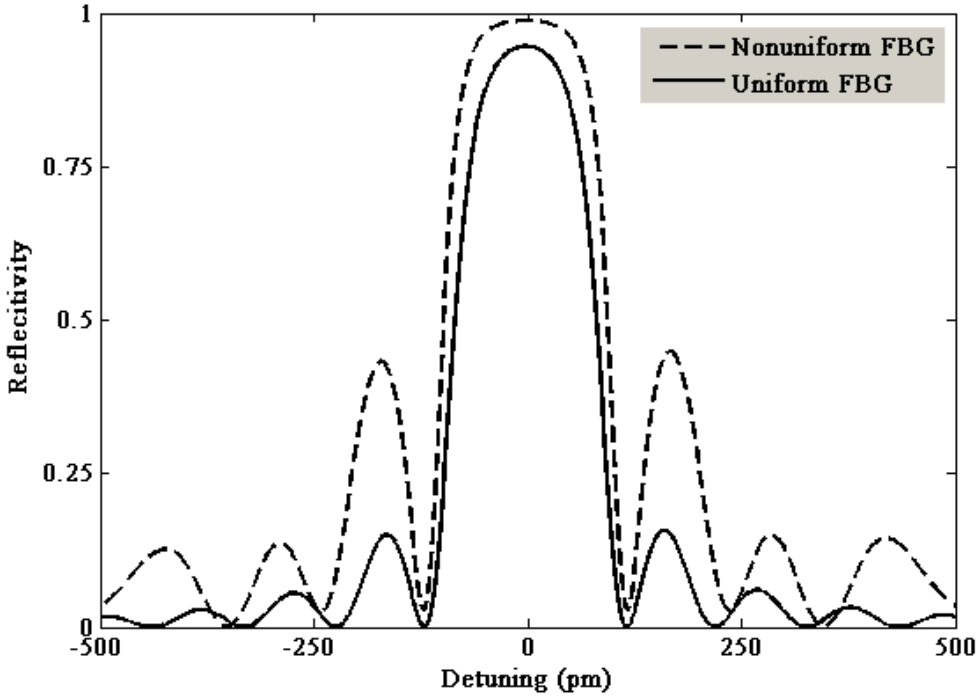

Figure 4.2.2 Plots of the grating reflectivity vs. detuning for uniform and nonuniform index modulations

purchased from JDSU. While unfortunately there is no remaining literature available from the company that can provide specifications of the FBG's design, there is reason to believe that the grating is apodized. The JDSU grating spectrum may be described as a table top, with a broad central peak and well-suppressed side lobes. The side lobe suppression may be simulated by assuming a Gaussian envelope to the raised cosine index modulation. Fig. 4.2.2 shows the simulation results.

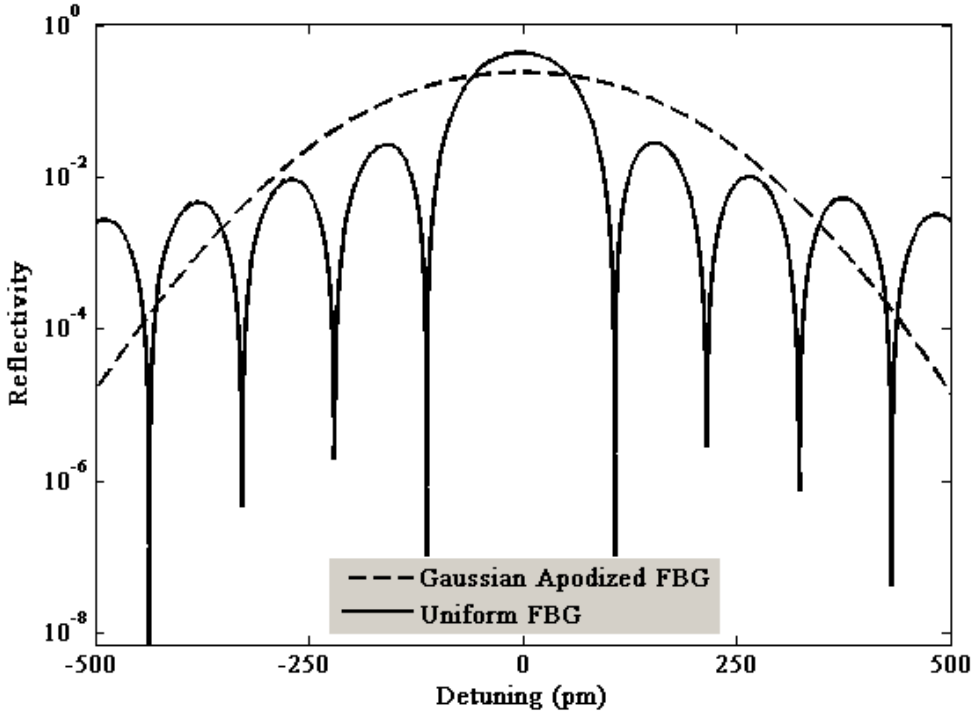

Figure 4.2.3 Plots of the reflectivity versus detuning for a uniform grating and a Gaussian apodized grating. Note that the reflectivity is expressed on a log scale in order to highlight the extent of the side lobe suppression.

4.3 FBG Sensitivity

FBGs are effective sensors because they are sensitive to numerous environmental conditions. The Bragg equation (Eqn. 4.1.1) is used to determine how the different environmental conditions influence the spectral features. In our etched fiber Bragg grating and fiber Fabry Perot sensors, the central Bragg wavelength is measured in real-time. In order to understand how FBGs may be used to sense the index of refraction of solutions and adsorbed chemicals, one must understand how temperature, strain, and surrounding indices influence the Bragg wavelength. The Bragg wavelength shifts with three primary environmental changes according to the Bragg equation [Ref. 4.3.1]:

$$\Delta\lambda_{Bragg} = 2\left(\Lambda_g \frac{\partial n_{eff}}{\partial T} + n_{eff} \frac{\partial \Lambda_g}{\partial T}\right)\Delta T + 2\left(\Lambda_g \frac{\partial n_{eff}}{\partial L} + n_{eff} \frac{\partial \Lambda_g}{\partial L}\right)\Delta L + 2\left(\Lambda_g \frac{\partial n_{eff}}{\partial n_{surr}} + n_{eff} \frac{\partial \Lambda_g}{\partial n_{surr}}\right)\Delta n_{surr} \quad (4.3.1)$$

The first term represents the Bragg shift due to a change in the temperature. The second term represents the shift due to strain. Lastly, the grating pitch Λ_g does not depend on the bulk surrounding index and so only the first expression in the third term (refractive index sensing) is nonzero. The total Bragg shift due to all of these factors is expressed as:

$$\Delta\lambda_{Bragg} = 2\left(\Lambda_g \frac{\partial n_{eff}}{\partial T} + n_{eff} \frac{\partial \Lambda_g}{\partial T}\right)\Delta T + 2\left(\Lambda_g \frac{\partial n_{eff}}{\partial L} + n_{eff} \frac{\partial \Lambda_g}{\partial L}\right)\Delta L + 2\left(\Lambda_g \frac{\partial n_{eff}}{\partial n_{surr}}\right)\Delta n_{surr} \quad (4.3.2)$$

Sections 4.3.1, 4.3.2, and 4.3.3 discuss the three above terms in the order as they appear in Eqn. 4.3.2.

4.3.1 Temperature Sensitivity

$$\Delta\lambda_{B,temperature} = 2\left(\Lambda_g \frac{\partial n_{eff}}{\partial T} + n_{eff} \frac{\partial \Lambda_g}{\partial T}\right)\Delta T$$

$$\Delta\lambda_{B,temperature} = \lambda_B\left(\frac{1}{n_{eff}} \frac{\partial n_{eff}}{\partial T} + \frac{1}{\Lambda_g} \frac{\partial \Lambda_g}{\partial T}\right)\Delta T \quad (4.3.3)$$

$$\Delta\lambda_{B,temperature} = \lambda_B\left(Thermo-optic + Thermal-\exp ansion\right)\Delta T$$

The temperature sensitivity of a fiber Bragg grating derives partly from the thermo-optic effect and partly from thermal expansion. The thermo-optic effect

represents the change in the refractive index of a material due to the change in temperature. Different materials may exhibit positive or negative thermo-optic constants and some materials (e.g. silica) exhibit both depending on dopant type and relative concentration. Ferreira, et al and others quote the value of typical germanosilicate fibers as having a thermo-optic constant of 8.5×10^{-6} [Ref. 4.3.2]. The thermo-optic constant of plain germanosilicate is greater than that of the boron co-doped fibers. The concentration of boron and germanium within the core and cladding will determine the properties in each region. The thermo-optic constant of the Newport FBG was measured directly in a temperature compensated mount, which will be discussed at the end of this section. Mode confinement must also be considered if the core and cladding have different dopant levels, as is the case for the Newport boron co-doped fiber. Unfortunately, both Newport and NuFern (plain germanosilicate fibers) maintain that the dopant levels in the photosensitive fibers used in the experiments are protected trade secrets.

Thermal expansion of the glass fiber also causes shifts in the Bragg wavelength. Most materials expand when the temperature increases, however there are some exotic materials that contract. Silica, for example, has a thermal expansion constant of 0.5×10^{-6}. This means that every unit of length along the fiber will increase by the same fraction of that length, including between the high and low index regions within the grating. If the fiber expands with an increase in temperature then the grating pitch increases and the Bragg wavelength red-shifts. In terms of temperature dependence, the thermal expansion accounts for only 5.5% of the total effect. Silica is known to have a particularly low constant of thermal expansion (CTE), as compared to common metals and plastics which expand and contract 20-100 times more with temperature fluctuations.

The Bragg wavelength will shift a total of 10pm/°C at 1550nm for typical germanosilicate fibers. While boron co-doping decreases the sensitivity of our in-house FBGs to temperature changes, a temperature compensated mount was designed to further reduce the temperature sensitivity. In addition to compensating for the positive Bragg shift with temperature, the mount also provides the structural support necessary for handling the fiber sensor. There are exotic materials with near-zero and negative CTE values, though the materials are costly and some, as in the case of some ceramics, are not compatible with the rigors of chemical etching and testing. Table 4.3.1 lists the estimated CTE values for materials that were considered for the mount.

Material	**CTE ($x10^{-6}$)**
Silica	0.5
Invar 36	1.2-1.6
Stainless Steel 416	9.9
Aluminum 6063	23.4
Acrylate	45-60

Table 1.3.1 Commonly cited CTE values for various materials in the range from 20-100°C.

The purpose of the mount is to hold the fiber under tension at two points that contract when the temperature of the mount increases. The mount's contraction is designed to compensate for the thermo-optic effect. As long as tension is maintained on the fiber, the length of the fiber, and thus the grating, depends on the distance between two epoxied points on the mount. Tension must be maintained during temperature cycling so that the fiber expands and contracts with the two contact points. The design of the fiber holder hinges on machining two materials with different CTE values and assembling them so that one expands outward and one expands inward along the fiber axis. Fig. 4.3.1 shows the design. Lengths L_1 and L_2 have to be chosen such that the net

effect compensates for the fiber's thermo-optic constant. By fixing the high-CTE metal at the ends of the low-CTE material, the high-CTE metal expands outward and the low-CTE metal expands inward with increasing temperature and vice versa with decreasing temperature.

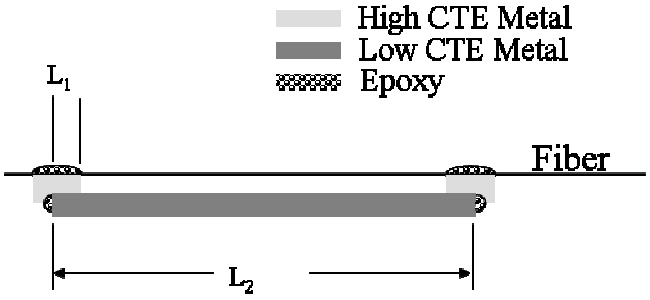

Figure 4.3.1 Side-view of the temperature-compensated mount design. Epoxy holds the two metals in contact at the end of the low-CTE metal.

Additionally, the mount design should accommodate at least two types of optical fiber components. In addition to a 7.5mm long FBG, the 2-4cm long fiber Fabry Perot must fit. As such, the spacing $L_2 - 2L_1$ should be designed to be approximately 5cm long.

$$\alpha_{HighCTE} \times 2L_1 - \alpha_{LowCTE} \times L_2 = \zeta_{FBG} \qquad (4.3.4)$$

where $\alpha_{HighCTE}$ and α_{LowCTE} are the thermal expansion constants of the two metals and ζ_{FBG} is the thermo-optic constant of the fiber. The thermo-optic constant of a fiber of unknown dopants may be measured directly while testing this type of mount. If we vary lengths L_1 and L_2 we expect to find a linear relationship, where the slope yields a value for the thermo-optic constant. As mentioned previously, the dopant levels within the Newport boron co-doped fiber are protected trade secrets.

The Bragg wavelength's sensitivity to 0.1°C temperature fluctuations should be kept at or below 0.01pm range so as to not interfere with refractive index sensing. The minimum proposed line widths for the spectral resonances are on the order of 0.01pm.

Improving temperature sensitivity equates to reducing the minimum detectable wavelength shift and therefore refractive index shift. If the wavelength resolution is not limited by thermal effects on the silica itself, then we must consider the temperature effects on liquids used in sensing. For this limiting case, the thermo-optic term is dominated by the refractive index shift of surrounding solution.

$$\Delta\lambda_{B,temperature} = \lambda_B \left(\frac{1}{n_{eff}} \frac{\partial n_{eff}}{\partial T} \right) \Delta T$$

$$\Delta\lambda_{\min imum} = \lambda_B (\zeta_{solution}) \Delta T_{\min imum} \qquad (4.3.5)$$

The minimum detectable temperature shift is only limited by the responsiveness and sensitivity of a YSI 2252 thermistor at room temperature. While the accuracy of determining local temperatures may be improved with higher resolution thermometers, practical RI sensing of chemical processes is limited by the temperature uniformity and convection within the liquid solutions.

4.3.2 Strain Sensitivity

$$\Delta\lambda_{Bragg,strain} = 2 \left(\Lambda_g \frac{\partial n_{eff}}{\partial L} + n_{eff} \frac{\partial \Lambda_g}{\partial L} \right) \Delta L$$

The second part of Eqn. 4.3.2 represents the Bragg shift due to lengthening the fiber. In addition to the physical stretching of the index modulation, the refractive index of the glass changes due to lattice stress. The latter is the stress-optic effect. In typical germanosilicate fibers, and those co-doped with boron, the stress-optic effect reverses the shifts due to lengthening the fiber.

Straining the silica fiber causes stress within the lattice in both transverse and longitudinal directions to the applied strain direction. This is called the Pockels effect or

the photoelastic effect. The strain-optic tensor relates the refractive index shifts along different crystal directions with an applied strain in each or a combination of directions. For cylindrical fibers, the Pockels coefficients p_{11} and p_{12} are the only relevant tensor components, describing index shifts of two transverse polarizations for tension applied along the z-axis of the fiber.

$$P = \frac{n}{2}(p_{11} - \upsilon \times (p_{11} - p_{12}) \qquad (4.3.6)$$

The other component of the strain-induced Bragg shift is from the fiber's elongation. $\frac{\partial \Lambda_B}{\partial L}$ represents how much the grating pitch lengthens when the fiber length L has been increased by ∂L. Each unit of the fiber length increases by the same fractional amount as the entire fiber length. Therefore if the fiber's length has increased by 10^{-6} of the total length then the grating region has increased by 10^{-6} times *its* total length and the grating pitch has increased by 10^{-6} times *its* period. This is a unit called micro strain, με. Fiber strain exceeding 5-10με is likely to cause fiber breakages in recently exposed photosensitive fibers due to small defects.

The net effect of strain on the fiber is reduced from that expected from elongation alone. Standard experiments have shows that the multiplicative factor M is between 71-78% of the expected shift [Ref 4.3.1].

$$\Delta\lambda_{Bragg,strain} = 2\left(n_{eff}\frac{\partial \Lambda_g}{\partial L}\right)(1-P)\Delta L$$

$$\Delta\lambda_{Bragg,strain} = 2\times M \times \left(n_{eff}\frac{\partial \Lambda_g}{\partial L}\right)\Delta L$$

Fiber Bragg grating sensors have been used extensively as strain gauges for decades. A FBG may be used to measure the elongation of numerous substrates, including the metals used in the temperature compensated mount. Results from an experiment to verify the CTE of aluminum will be discussed in Chapter 6.

4.3.3 Refractive Index Sensitivity

$$\Delta\lambda_{Bragg,RI} = 2\left(\Lambda_g \frac{\partial n_{eff}}{\partial n_{surr}}\right)\Delta n_{surr}$$

The remaining component of sensitivity to be examined is the expected Bragg shift for a change in the environmental index of the fiber. Theoretical shifts in effective index with surrounding index changes were modeled in Section 2.4. As Bragg shifts will respond linearly to the change in effective index, the Bragg sensitivity follows according to the sensitivity of the effective index to the change in surrounding solution. Thusly, it has been shown that the Bragg wavelength shifts most with an etched fiber where the surrounding index is near to the core index. Furthermore, we may take the limit that the modal confinement goes to 100% in the limit that $n_{surrounding} \rightarrow n_{core}$. As this occurs, $\frac{\partial n_{eff}}{\partial n_{surr}} \rightarrow 1$, and the ultimate wavelength sensitivity is

$$S = \frac{\Delta\lambda_{Bragg,RI}}{\Delta n_{surrounding}} = {2\Lambda_{grating}}/{riu} \approx 1063\,{nm}/{riu} \qquad (4.3.7)$$

where *riu* represents the "refractive index unit." While practical limitations of handling and measuring make this sensitivity unrealistic, etched fibers with diameters of 3μm-5μm are sensible. Fig. 4.3.2 uses similar data as in Fig. 2.4.6 to plot the Bragg wavelength for various surrounding indices, given that the fiber is standard etched Corning SMF-28. The slope varies and represents the Bragg sensitivity to surrounding index. For lower

indices, higher order modes display greater Bragg sensitivity to index shifts than the fundamental modes at any given fiber diameter. However, as the surrounding index approaches the core index, the most sensitive mode is the fundamental mode.

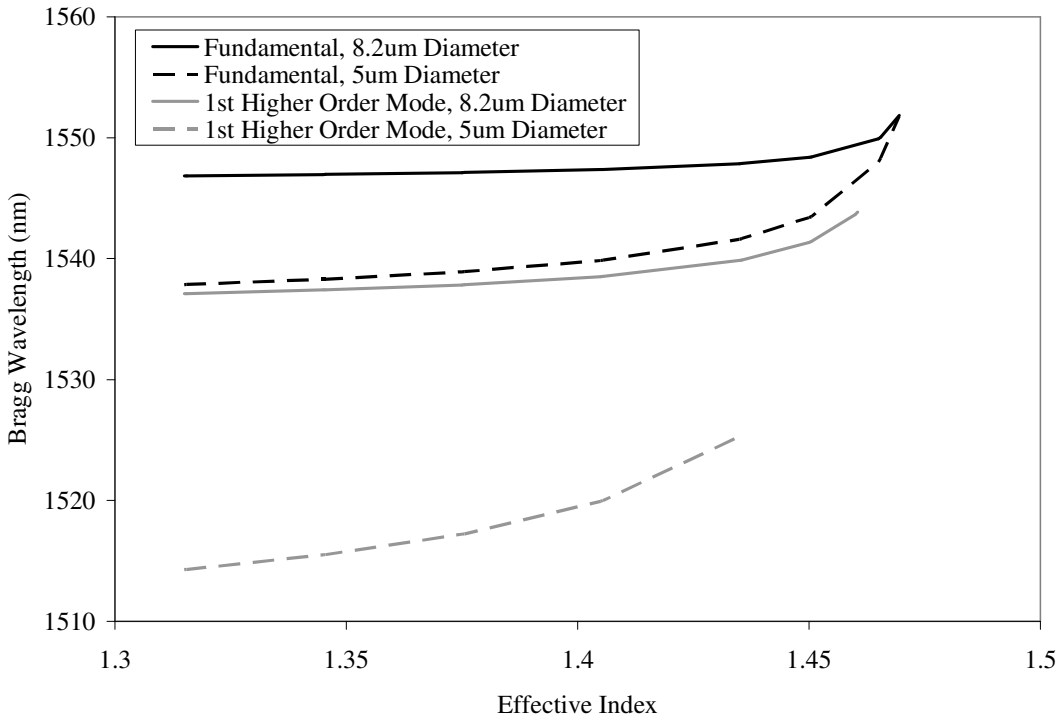

Figure 4.3.2 Plot of the Bragg wavelength vs. effective index for fundamental and first higher order modes.

Chapter 5: Fiber Fabry Perot Theory

Fiber Fabry Perot (FFP) cavities consist of two reflective of fiber components with similar reflection spectrum separated by a short distance. Common FFPs use dielectric and metal mirrors on cleaved fiber facets to create the reflective components required. The reflective components may also be a set of fiber Bragg gratings that are written to share the same central Bragg wavelength. Highly reflective Bragg gratings may reach reflectivies of over 45dB within boron co-doped fibers and thus serve as excellent mirrors for a FFP. The sharpness of the Fabry Perot transmission peaks, characterized by finesse, is the figure of merit for a high quality Fabry Perots. The finesse is defined as the ratio of the spectral separation between two transmission peaks divided by the full width at half the peak transmission. For highly reflective gratings and low loss fibers, finesse values over 10,000 seem achievable. Furthermore, an etched fiber Fabry Perot will significantly enhance the sensitivity of an etched FBG refractive index sensor.

5.1 Fiber Fabry Perot Spectra

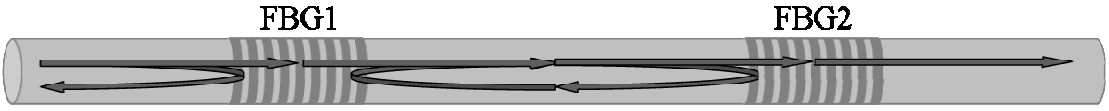

Figure 5.1.1 Depiction of the reflections and optical path for light within a fiber Fabry Perot

The two gratings FBG1 and FBG2 act as any mirrors do in a standard Fabry Perot cavity, though the wavelength-dependence of the reflectivity is much greater than a

metal-coated mirror. Light enters the structure through one of two FBGs. The reflection and transmission spectra may be calculated for wavelength-independent reflectivity, R, and transmittivity, T.

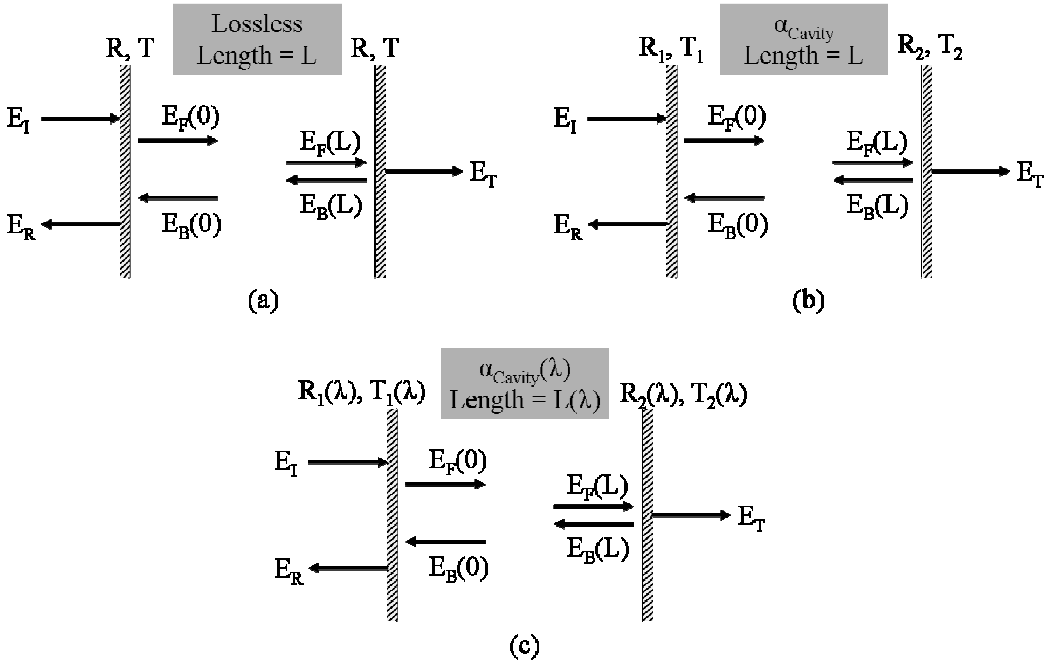

Figure 5.1.2 Spectral plots can be analyzed by calculating the electric fields of (a) a lossless, symmetric Fabry Perot cavity, (b) a lossy asymmetric Fabry Perot cavity, or (c) a Fabry Perot cavity with the R, T, α, and L are wavelength dependent, as with practical FFPs.

Taking the example show in Fig. 5.1.2 (b), the fiber Fabry Perot may be analyzed at a fixed wavelength of the spectrum where R_1, T_1, R_2, T_2, and cavity loss α_{Cav} are constant. E_I and E_R represent the input and reflected amplitudes of the electric fields. E_T represents the amplitude of the transmitted field. In between the mirrors, the electric fields are forward and backward propagating, as in coupled wave theory from Section 3.2, and defined at either side of the cavity. Mirrors are treated as infinitesimally thin and none of the parameters depend on wavelength. Beginning with expressions for three of the field expressions, E_R, $E_B(0)$, and $E_F(0)$, the transmission and reflection spectra may be calculated in terms of detuning from a spectral resonance.

$$E_R = \sqrt{R_1}\,E_I + \sqrt{T_1}E_B(0) \tag{5.1.1}$$

$$E_B(0)e^{ikL} = \sqrt{R_2}E_F(0)e^{-ikL}e^{-\alpha L/2} \tag{5.1.2}$$

$$E_F(0) = \sqrt{T_1}E_I + \sqrt{R_1}E_B(0)e^{-\alpha L/2} \tag{5.1.3}$$

By substituting Eqn. 5.1.3 into Eqn. 5.1.2 and then substituting the result into Eqn. 5.1.1, the ratio between the reflected electric field amplitude and the input electric field amplitude is solved.

$$\left|\frac{E_R}{E_I}\right|^2 = \frac{R_1 + R_2e^{-\alpha L} - 2\sqrt{R_1R_2}(1-2\sin^2(kL))e^{-\alpha L/2}}{1+R_1R_2e^{-\alpha L} - 2\sqrt{R_1R_2}(1-2\sin^2(kL))e^{-\alpha L/2}} \tag{5.1.4}$$

The product of the propagation constant k and the length L is the phase information and indicates detuning from the resonance. Eqn. 5.1.4 is an expression for the reflection spectrum of a lossy Fabry Perot. A similar equation may be derived using another triplet of equations derived from example in Fig. 5.1.2 (c).

$$E_T = \sqrt{T_2}E_F(0)e^{-ikL}e^{-\alpha L/2} \tag{5.1.5}$$

$$E_F(0) = \sqrt{T_1}E_I + \sqrt{R_1}E_B(0)e^{-\alpha L/2} \tag{5.1.6}$$

$$E_B(0) = \sqrt{R_2}E_F(0)e^{-ikL}e^{-\alpha L/2} \tag{5.1.7}$$

Similarly, by substituting Eqn. 5.1.7 into Eqn. 5.1.6 and then substituting the result into Eqn. 5.1.5, the ratio between the transmitted electric field amplitude and the input electric field amplitude is solved

$$\left|\frac{E_T}{E_I}\right|^2 = \frac{T_1T_2e^{-\alpha L}\Big/\left(1-\sqrt{R_1R_2}e^{-\alpha L}\right)^2}{1+\dfrac{4\sqrt{R_1R_2}e^{-\alpha L}}{\left(1-\sqrt{R_1R_2}e^{-\alpha L}\right)^2}\sin^2(kL)} \tag{5.1.8}$$

The reflection and transmission spectra are calculated over 2π detuning spans for varying grating strengths.

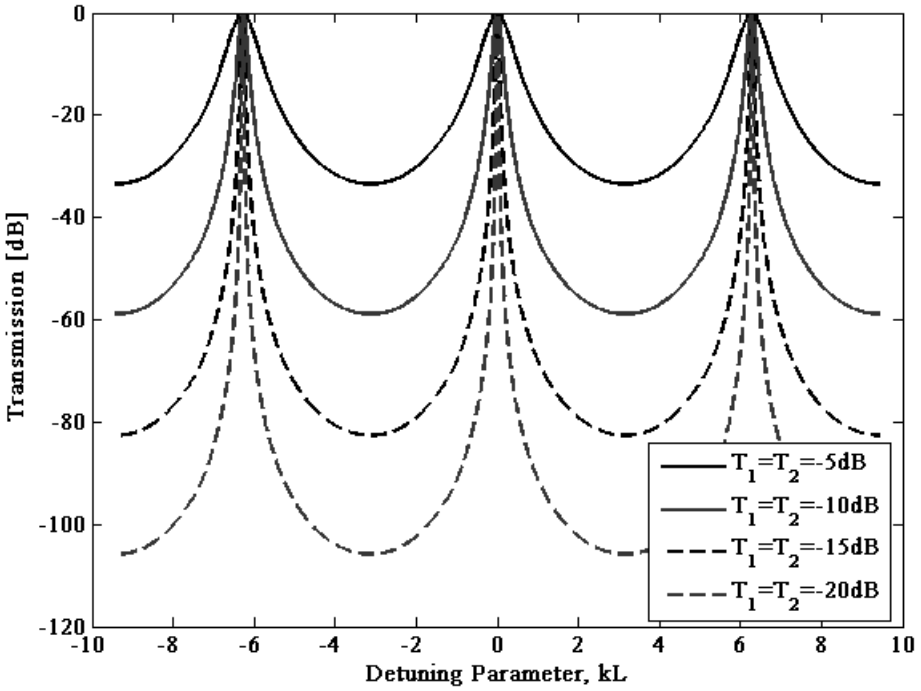

Figure 5.1.3 Transmission spectra for a Fabry Perot comprised of two mirrors of equal reflectivity. Plots show how the T-spectrum changes for stronger gratings.

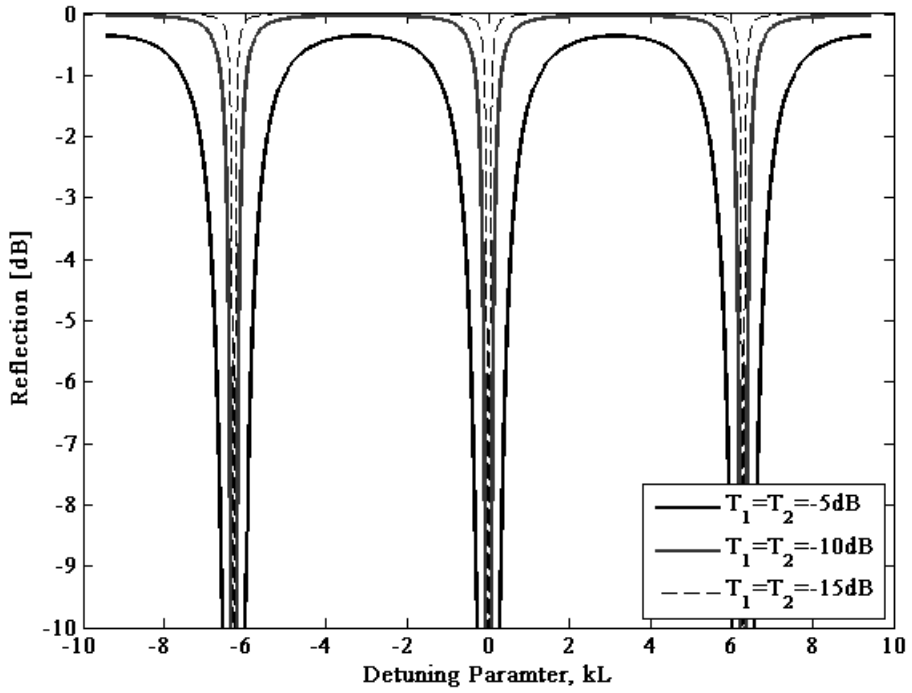

Figure 5.1.4 Reflection spectra for a Fabry Perot comprised of two mirrors of equal reflectivity. Plot shows how the R-spectrum changes for stronger gratings.

5.2 Fabry Perot Finesse

Two spectral quantities indicate the quality of a Fabry Perot cavity: finesse and throughput. Finesse is a ratio between the resonance linewidth and the free spectral range. The free spectral range is a fixed quantity for a Fabry Perot cavity with a fixed length.

$$FSR = \Delta\upsilon = \frac{c}{2nL} \tag{5.2.1}$$

In Eqn. 5.1.9, the values c, n, and L are the speed of light, the refractive index, and the cavity spacing. Within waveguides, such as fibers, the effective refractive index should be used for *n*. In the plots in Figs. 5.1.3 and 5.1.4, the FSR is represented by a detuning of 2π. The linewidth is the other factor when considering finesse. The linewidth of a Fabry Perot resonance may be solved analytically from Eqns. 5.1.4 and 5.1.8. For strong gratings the following expression can be used:

$$F = \frac{Linewidth}{FSR} = \frac{\pi}{2}\sqrt{\frac{4\sqrt{R_1R_2}}{(1-\sqrt{R_1R_2})^2}} \tag{5.2.2}$$

Fig. 5.2.1 on the next page shows how finesse changes when the mirror reflectivities are not equal. For fixed mirror spacing, the linewidth decreases for increasing values of R_1 and R_2.

In Fig. 5.1.4, the FSR is kept constant and as the reflectivity of the mirrors increases the linewidth decreases dramatically. Take, for example, a cavity spacing of 1cm and a finesse of 10,000. The FSR of this Fabry Perot will be 82.8pm if the cavity is filled with glass and 91.3pm if the cavity is filled with water. Accordingly, the linewidth of the resonances will be $8.28\text{x}10^{-15}$fm and $9.13\text{x}10^{-15}$fm respectively. Resonances on

this order of magnitude are commonly quantified in units of frequency. The linewidths are 1.03MHz and 1.13MHz respectively. As reference, the laser used for grating interrogation is a tunable laser with a linewidth of 100kHz.

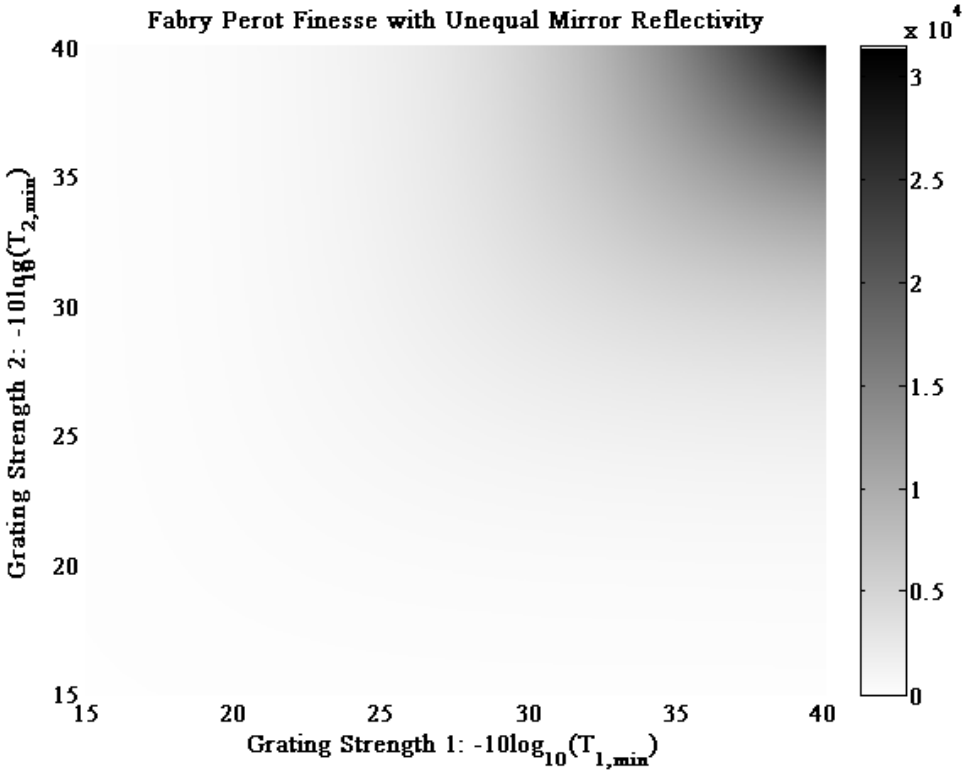

Figure 5.2.1 Height-coded of the Fabry Perot finesse versus the grating strength. Grating strength is represented by the minimum transmission

Figures 5.3.1, 5.3.2, and 5.3.3 all show how the finesse may be affected by fiber losses and unequal grating reflectivity. In conclusion, the finesse is only affected by the intracavity losses and the product of the two reflectivities. Mirror losses, from scattering or absorption, may also degrade the finesse of a Fabry Perot for FBG Fabry Perots. When light penetrates a FP mirror, mirror loss becomes intracavity loss. For deeper penetrations depths, intracavity loss is exacerbated. The effective grating length, or penetration depth, of a FBG is related to the reflectivity of the grating. For stronger

gratings, the entering light does not reach the end of the grating. Effective grating lengths may be expressed in terms of reflectivity [Ref. 5.2.1]:

$$\frac{L_{eff}}{L} = \frac{\sqrt{R}}{2a\tanh(\sqrt{R})} \tag{5.2.3}$$

Depending on reflectivity, the fiber Fabry Perot lengthens by $L_{eff,1}+L_{eff,2}$ according to Eqn. 5.2.3. Lengthening the cavity reduces the FSR and the linewidth accordingly. Considering losses within the grating region, the effective grating length also enhances the intracavity losses that degrade the finesse.

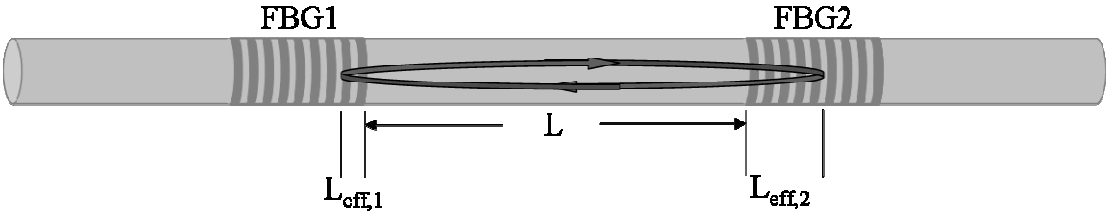

Figure 5.2.2 Effective lengths of the gratings cause the separation between the mirrors to be greater than the physical separation.

$$FSR = \frac{c}{2n(L + L_{eff,1} + L_{eff.2})} \tag{5.2.4}$$

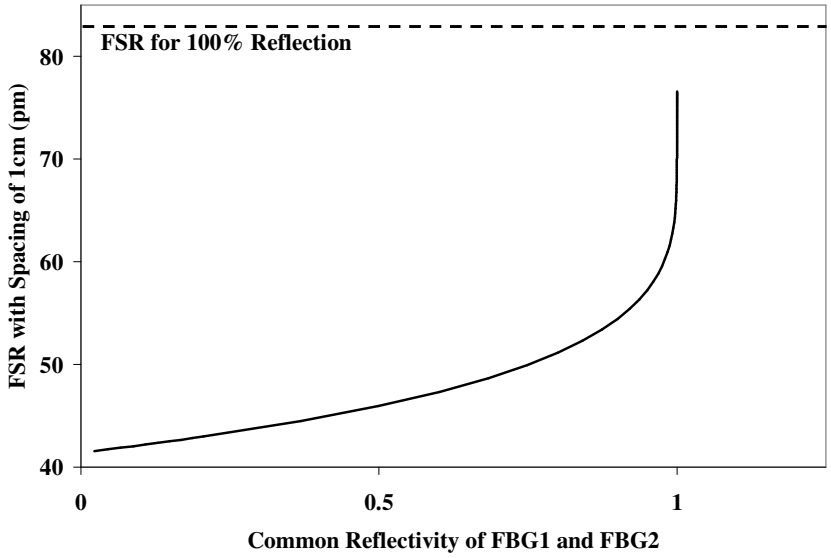

Figure 5.2.3 Plot of the FSR of a Fabry Perot with two FBGs of the same reflectivity. The FSR for 100% reflecting FBGs is 82.8pm

Additional intracavity losses from grating penetration do not alter any of the previously established equations. The loss term α includes all intracavity loss.

5.3 Fabry Perot Throughput

The throughput is a comparative measure of the peak transmitted light on-resonance. It is normalized to the input power. Transmission at the peak resonance is normalized to the input power and so the throughput is expressed as a fraction. Rewriting Eqn. 5.1.8, throughput is the transmission when detuning is equal to zero (on-resonance)

$$\left|\frac{E_T}{E_I}\right|^2_{on-resonance} = T_1 T_2 e^{-\alpha L} \Big/ \left(1-\sqrt{R_1 R_2}\, e^{-\alpha L}\right)^2 \qquad (5.1.11)$$

Mirror losses (expressed by unexpectedly low values of T_1 and T_2) and intracavity loss severely degrade the throughput of a Fabry Perot. Furthermore, we expect that unequal reflectivity in the two gratings will vary the throughput. For a lossless cavity $\alpha \rightarrow 0$, the throughput goes to 1 if the grating reflectivities are equal. Spectra in Figs. 5.1.3 and 5.1.4 both demonstrate throughputs of 100%. When forming FPs with FBGs, the central Bragg wavelengths must overlap so that the peak reflectivities share the same bandwidth. This ensures high finesse. When writing the second FBG of the FP, the throughput may be monitored to estimate the maximum overlap of the spectra. Eqn. 5.1.11 shows that throughput is maximized for equal reflectivies. The maximum throughput will occur at the maximum overlap if the writing process does not create lossy defects at a comparable rate. Since defects cause greater mirror and intracavity losses, the throughput will not appear to increase for FBG spectra that overlap more.

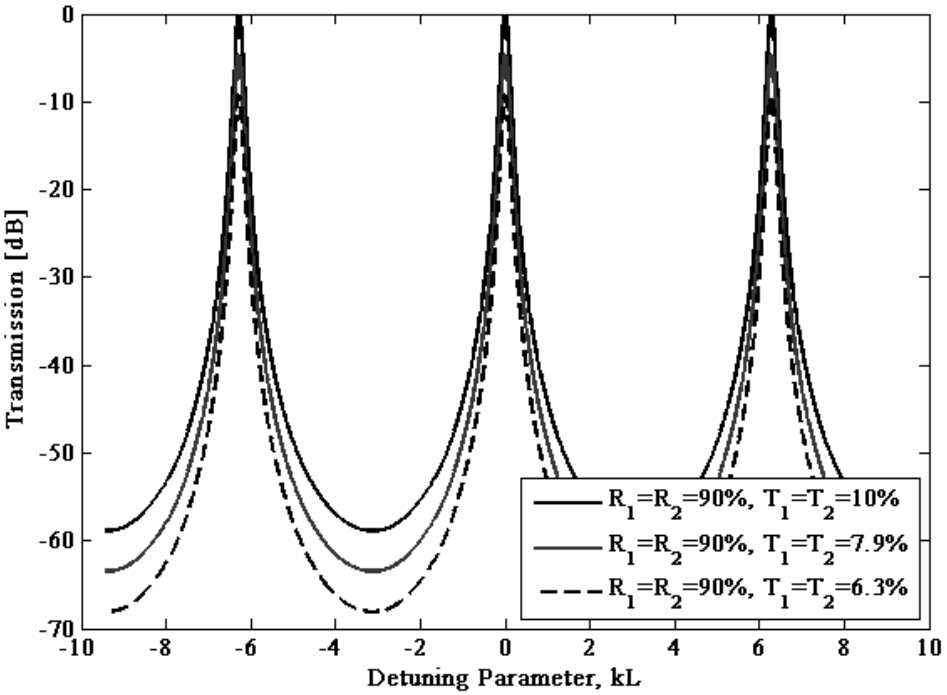

Figure 5.3.1 Plots of the Fabry Perot transmission spectrum for increasing mirror losses. Both mirrors share the same value of reflectivity and transmittivity but R+T≠1 necessarily. The finesse remains constant but the throughput is changed.

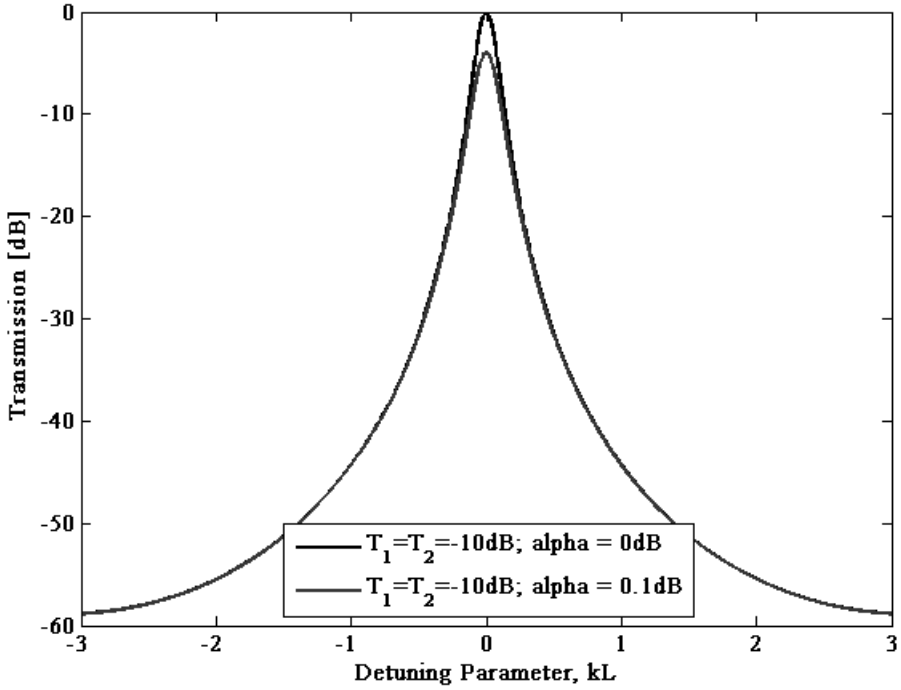

Figure 5.3.2 Plots of the Fabry Perot transmission spectrum for a lossless cavity and a cavity with 0.1dB per round trip. The finesse and throughput are affected.

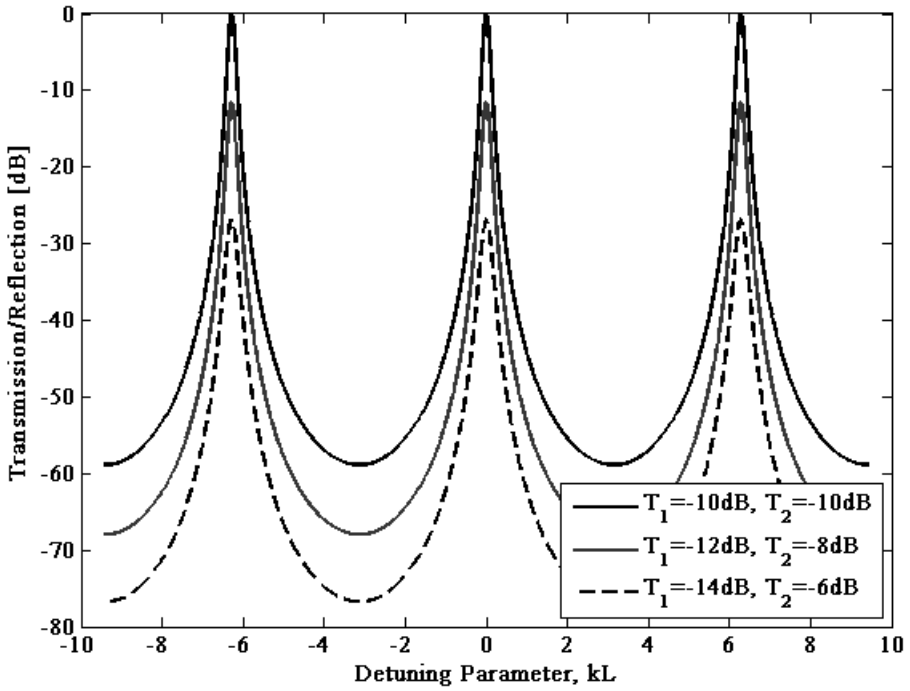

Figure 5.3.3 Plots of the Fabry Perot transmission spectrum for mirrors of different reflectivities. Note that the average reflectivity remains constant with each plot. Both finesse and throughput are effected by these changes.

Figs. 5.1.6, 5.1.7, and 5.1.8 demonstrate the effects of mirror loss, cavity loss, and unequal reflectivities on the throughput. As mentioned in Section 2.5, thermal annealing mends losses from scattering and absorption within the grating. The intracavity absorption losses are minimized for the boron co-doped fiber as long as the cavity lengths are short. This makes loss within the grating region a primary concern. Throughput becomes the key indicator for loss reduction during thermal annealing. While a throughput measurement is a useful diagnostic for understanding grating losses, refractive index sensing focuses on determining the spectral resonance shifts in wavelength. For high finesse cavities, linewidths narrow and small wavelength shifts may be monitored easily.

5.4 Wavelength Dependent FFP Spectra

For all of the previously considered Fabry Perot spectra, grating reflectivity, transmittivity, loss, and length have been independent of wavelength. When a FP utilizes the reflections from fiber Bragg gratings, wavelength dependence drastically alters the shape of the spectrum.

In Section 4.1, FBG reflection spectra were plotted for varying index modulations. The flatness of the reflectivity versus wavelength changes based on the index modulation (both magnitude and pattern). With overlapping FBG spectra, the Fabry Perot spectrum has different FSR, finesse, and throughput throughout the spectrum. The FSR depends on the effective penetration depth within the grating. For FBGs, light will penetrate the grating at different distances because L_{eff} is dependent on reflectivity (Eqn. 5.2.3). Wavelengths in the FBG sidelobes and central peak edges have weaker reflectivity and will therefore penetrate more deeply into the gratings. FSR narrows and finesse broadens (for lossy gratings only) for wavelengths further from the central Bragg wavelength. Lower reflectivity also directly impacts the finesse.

According to Fig. 5.4.2, finesse varies between 0 and 3140 across a grating with 99.99% reflectivity. Likewise, the FSR changes with detuning from the central Bragg wavelength as in Fig. 5.4.3. Unlike the finesse plot, the FSR near to the Bragg wavelength is relatively flat and does not depend heavily on wavelength.

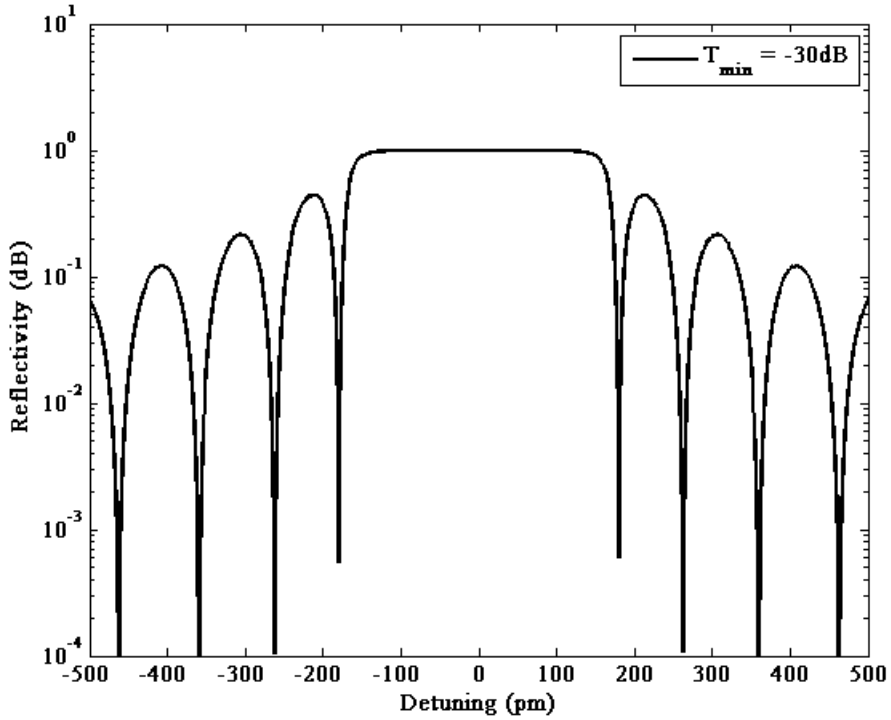

Figure 5.4.1 Plot of the reflectivity of a 30dB FBG versus detuning.

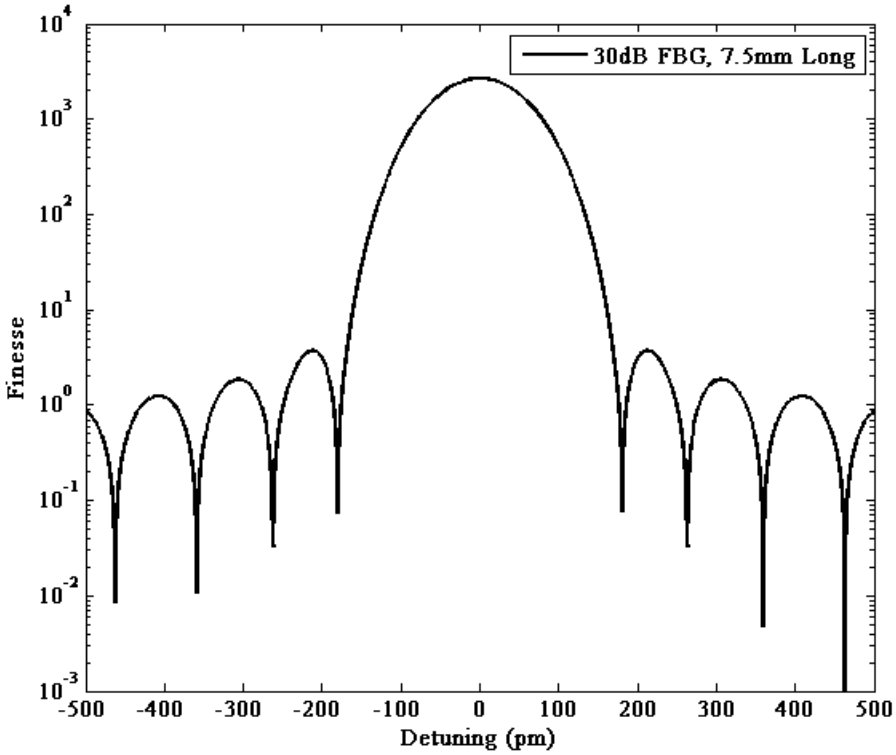

Figure 5.4.2 Plot of the finesse of a Fabry Perot with 30dB lossless FBGs versus detuning

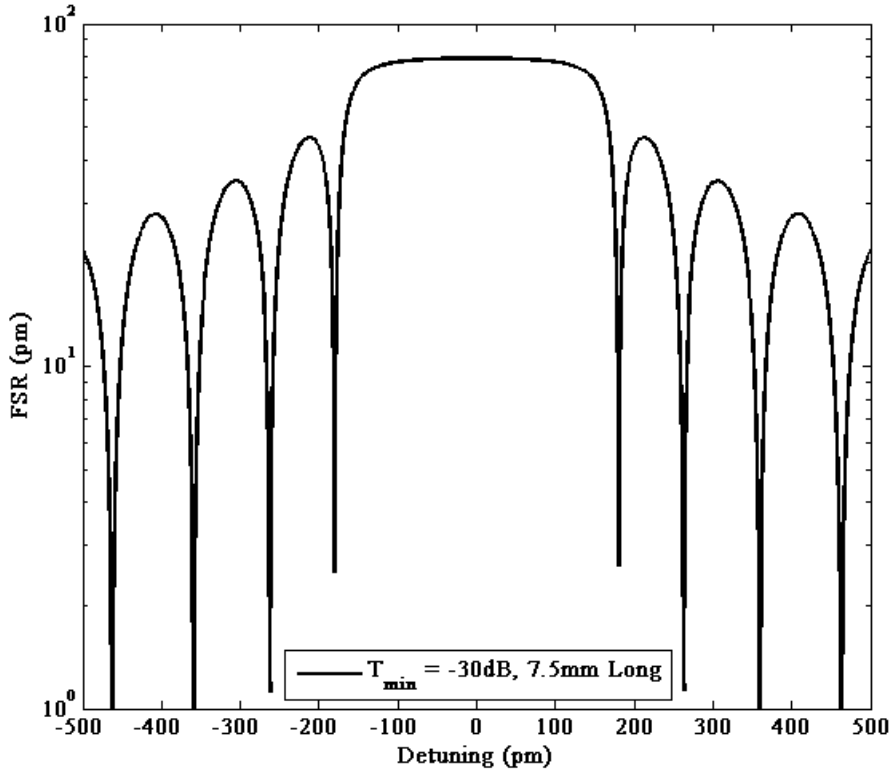

Figure 5.4.3 Plot of the FSR of a Fabry Perot with 30dB lossless FBGs versus detuning

In conclusion, a Fabry Perot comprised of FBG mirrors will have a nonuniform spectrum because the mirror characteristics change with detuning. The optimal finesse is at the center of the FBG spectrum where the reflectivity is greatest and effective grating lengths are shortest.

5.5 FFP Sensitivity and Minimum Index Resolution

Fiber Fabry Perots have been used for decades as highly sensitive environmental sensors. Analysis used to describe the FFP's sensitivity to environmental conditions resembles the analysis used for fiber Bragg gratings. Temperature, strain, and surrounding index influence sensors by changing the element's effective index and length. Multiplexed fiber Fabry Perot sensors are the most common FFP sensor and there

are numerous interferometric measurements that are common detection techniques [Ref. 5.5.1]

5.5.1 Temperature Sensitivity

The temperature sensitivity is examined similarly to the FBG temperature sensitivity. The analysis begins by describing the round-trip phase within the cavity:

$$\phi = 2n_{eff}kL_{cavity} = \frac{4\pi n_{eff}L_{cavity}}{\lambda} \qquad (5.5.1)$$

where the phase is expressed in terms of the effective index, the wavelength, and the cavity length. Temperature fluctuations cause shifts in the round-trip phase due to the thermo-optic constant and cavity strain [Ref. 5.5.2]:

$$\Delta\phi = \frac{4\pi n_{eff}L_{cav}}{\lambda}\left(\frac{1}{n_{eff}}\frac{\partial n_{eff}}{\partial T} + \frac{1}{L_{cav}}\frac{\partial L_{cav}}{\partial T}\right)\Delta T \qquad (5.5.2)$$

The first part of the expression in Eqn. 5.5.2 is the thermo-optic effect and the second part is the temperature-induced strain. The sum of these terms also appeared in the expression for FBG sensitivity to temperature in Eqn. 4.3.2. The temperature compensated mount that was described in Section 4.3.1 negates this sum by forcing the temperature dependent strain to have the exact opposite effect of the thermo-optic effect. Thus the temperature compensated mount described for the FBG works equally well for the FFP.

5.5.2 Refractive Index Sensitivity

The sensitivity of a FBG Fabry Perot may be analyzed similarly to the FBG itself. Sensitivity expressions starting with the expression for wavelengths supported within the FFP cavity:

$$m\lambda_{FP} = 2n_{eff}L_{cav} \tag{5.5.3}$$

Eqn. 5.5.3 states that an integer number of half-wavelengths must fit within the cavity for the cavity to be resonant. Sensitivity of the resonant wavelength to environmental changes comes from differentiating Eqn. 5.5.3:

$$\frac{\Delta\lambda_{FP}}{\Delta n_{eff}} = \frac{\lambda_{FP}}{n_{eff}} \tag{5.5.4}$$

The FFP resonance sensitivity to changing the effective index is constant. The sensitivity to changing the cladding index depends on how effectively the effective index may be changed by the cladding index.

$$\frac{\Delta\lambda_{FP}}{\Delta n_{surr}} = \frac{\lambda_{FP}}{n_{eff}}\frac{\Delta n_{eff}}{\Delta n_{surr}} \tag{5.5.5}$$

Plots derived from Eqn. 5.5.5 are calculated with the BPM simulations described in Chapter 3. Unless the entire length of the cavity is etched and equally influenced by the surrounding index (i.e. uniform diameter), Eqn. 5.5.4 must be changed to consider reductions in the sensitivity. As compared to A. Yariv's LPG Fabry Perot sensor [Ref 5.5.2], where the sensitivity is reduced by the limited etching within the cavity, our approach is to etch the entire cavity and grating regions. Etching enhances the sensitivity of the grating by the same amount of the etched FBG sensitivity to refractive index. The refractive index sensitivity becomes a sum of the sensitivity of the etched FBGs and the phase shifting of the Fabry Perot resonances. This doubles the wavelength shift per riu.

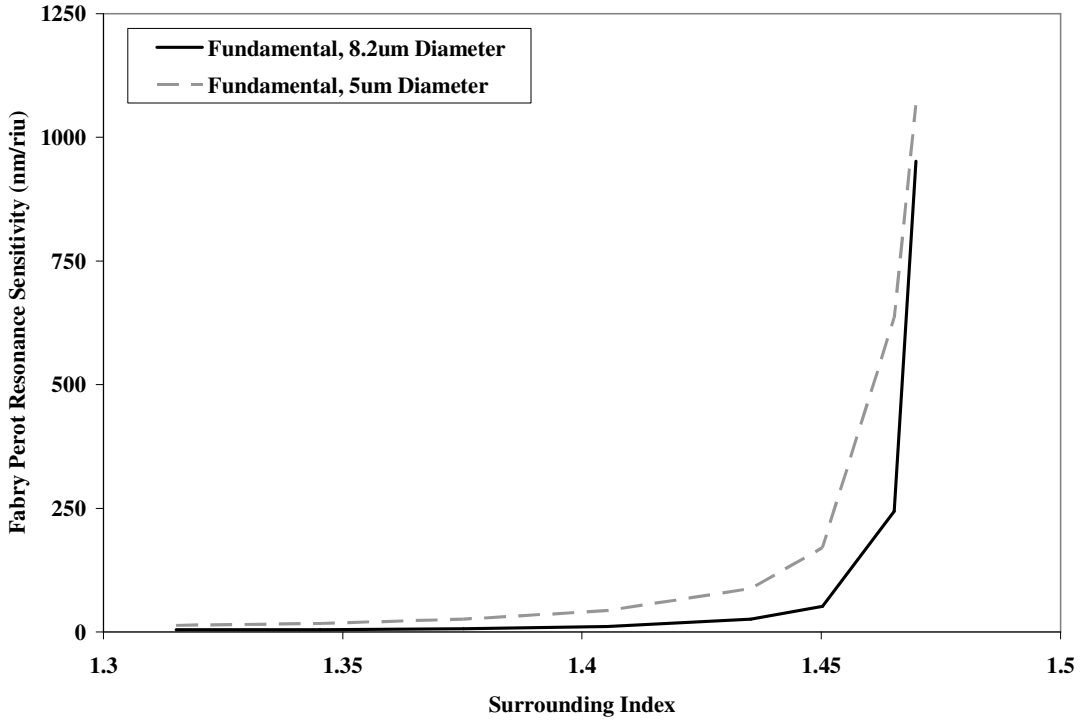

Figure 5.5.1 Refractive index sensitivity of a Fabry Perot resonance.

Highly sensitive refractive index sensors must detect minimal changes in the refractive index in order to effectively analyze adsorption and molecular binding studies. A combination of the Bragg sensitivity to refractive index change and the spectral sharpness of a high finesse cavity enhance what is possible to detect. Ultra-high finesse cavities with extremely narrow linewidths serve as ideal sensors for detecting the ultra small shifts in index. Vahala et al [Ref 5.5.3] have shown that single molecules may be detected by an induced thermo-optic effect within the whispering gallery modes of a silicon microcavity. The figure of merit that allows for such sensitive detection is proportional to Q^2/V or the ratio between the square of the cavity quality factor and the optical mode volume. For the silica microcavity, Vahala's Q is 10^8 can be realized and the mode volume is comparable to the fiber Fabry Perot mode volume. Therefore, the etched fiber Fabry Perot may be

used to detect single molecules for a Q of 10^8. At 1550nm, the FFP resonance linewidth must be on the order of 10^{-14}m in order to achieve such high Q and that linewidth is associated with a finesse of over 100,000. These finesse values are possible for grating reflectivities stronger than 99.997%. By increasing the mode volume, the requirement for finesse decreases and thus so does the reflectivity of the FBGs. Newport Corp. specifies that the boron co-dopes fibers have been inscribed with 47dB gratings with as few as 2000 exposures.

Chapter 6: Fabrication and Measurement

The FBGs used in the etched FBG sensor were purchased and prepared for sensing applications. On the other hand, the etched FFP sensors described in this theses were entirely fabricated in-house. Two different optical interrogation set-ups were used to characterize the spectral response and shifts in the sensors during fabrication and testing. In the first, a broadband source and 7pm optical spectrum analyzer resolution yielded a minimum wavelength resolution that is three orders of magnitude larger than the one that can achieved with our tunable laser set-up. The fabrication of gratings and sensors aimed to minimize the spectral features of the fiber components while maximizing the sensitivity to refractive index. This section will discuss the fabrication and measurement of the two different sensors.

6.1 Spectra Acquisition

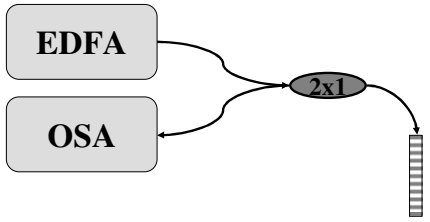

Figure 6.1.1 Interrogation set-up with a broadband EDFA source and Advantest Q3487 optical spectrum analyzer. Input and reflected signals pass through a 2x1 splitter. Resolution without curve-fitting = 7pm

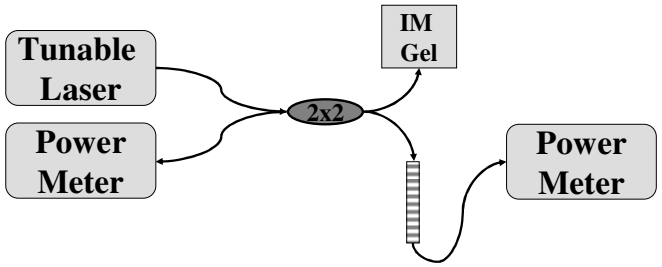

Figure 6.1.2 Interrogation set-up with an Agilent 81600 lightwave measurement system. Infrared source is a tunable semiconductor laser and synchronized power meters detect the transmitted and reflected signals. Reflections are reduced by immersing the unused pigtail in index-matching gel

Spectra acquisitions were performed with broadband and laser sources. The broadband signal was provided by an erbium-doped fiber amplifier. The EDFA gain spectrum spans from 1450nm-1650nm. The Advantest Q8347 optical spectrum analyzer has a minimum resolution of 7pm with a maximum buffer size of 2000 data points. Manual spectra acquisition regenerates every 7 seconds and, by interfacing through GPIB and Labview, automatic spectra acquisitions regenerate approximately every 10-15 seconds. The semiconductor laser within the Agilent 8164b has a linewidth of 100kHz, wavelength accuracy of 12MHz, maximum power output of 1W, and tuning rate 80nm/s. The lightwave systems allows for the tunable laser and power meters to coordinate and acquire spectra with 0.1pm accuracy. Data buffer sizes are limited to 10,000 data points and the acquisition time depends on the laser tuning rate, which ranges from 5nm/s to 80nm/s.

For the broader spectral features of an etched FBG, the EDFA/OSA set-up provides sufficient wavelength resolution and range to monitor the Bragg shifts in sensor testing. Labview interfaces with the optical spectrum analyzer so that spectral data is acquired and stored at regularly timed intervals.

Ultimately, wavelength precision limited the usefulness of the OSA set-up. The tunable laser set-up is preferred for acquiring spectral resolution features below the 1pm-

7pm spectral resolution. In the automatic tuning mode, the Agilent lightwave system could synchronize the internal power meter measurements with the laser's output wavelength to within 0.1pm. This wavelength accuracy is constant over the range of scan rates, varying from 5nm/s to 50nm/s. Agilent provides a Labview code for obtaining spectral scans using automatic tuning. Additionally, the spectral resolution may be increased by manually tuning the laser wavelength. By applying a modulated voltage to the system's BNC input, the wavelength could be tuned over much narrower wavelength ranges with even higher resolution. For this application, the lightwave system could store 4000 data points in the buffer for each of two power meters and had a minimum acquisition time of 100μs. Fig. 6.1.3 shows how the wavelength tuning is controlled by applied voltages.

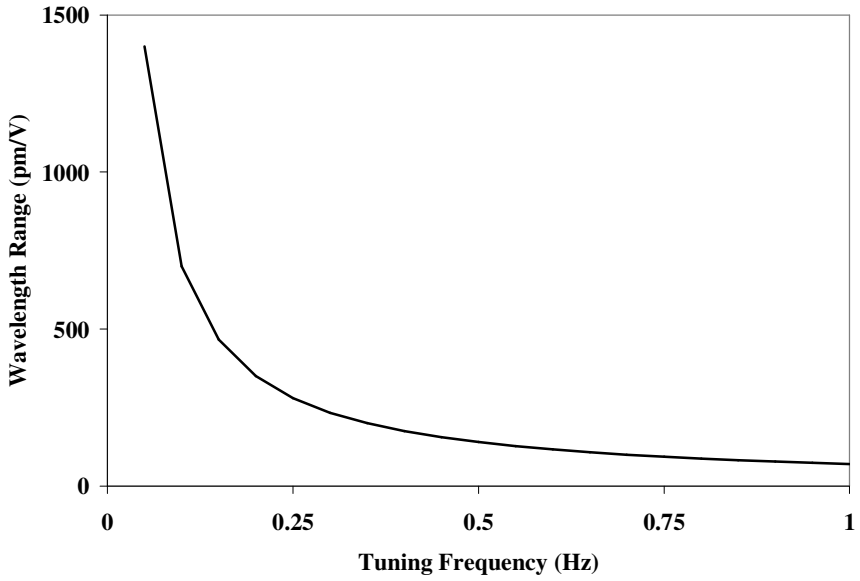

Figure 6.1.3 Plot of the manual tuning range of the laser wavelength. The wavelength range is in terms of wavelength units per volt of the applied signal magnitude.

With an applied voltage signal frequency of 0.25Hz and voltage range of +/-0.5mV, the spectral resolution increases by two orders of magnitude to $1x10^{-3}$pm. Fig. 6.1.4 shows

the comparison of two FFP transmission spectra acquired with automatic and manual tuning.

The spectra acquisition set-up that utilizes the Agilent tunable laser system improves the minimum wavelength accuracy by three orders of magnitude compared to the OSA set-up. The wavelength resolution is ultimately limited by the finite laser linewidth, which is 100kHz or 0.8×10^{-3}pm. For similar sensor refractive index sensitivities, the minimum detectable RI resolution is improved by the same three orders of magnitude by using the tunable laser set-up.

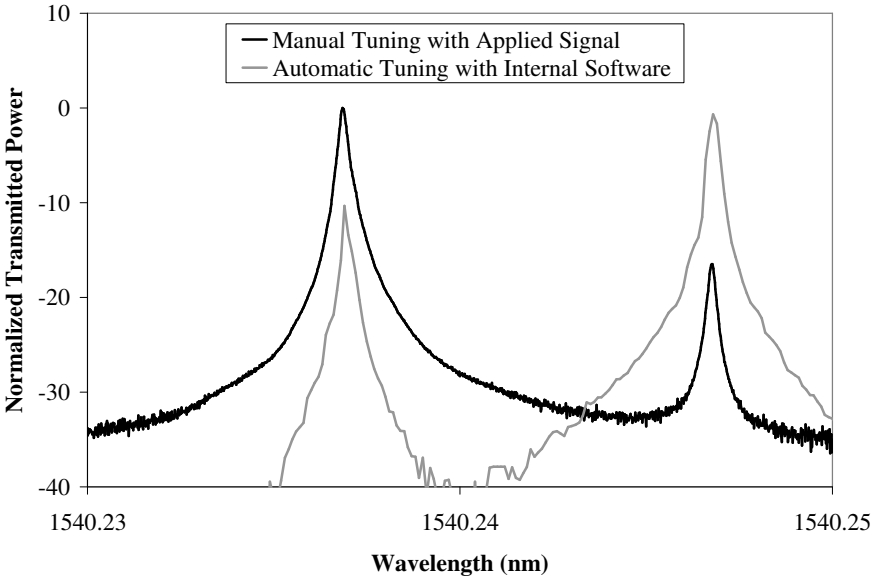

Figure 6.1.4 Comparison of tuning the Agilent laser source manually with an applied signal and automatically tuning with the internal software of the lightwave system.
Minimum Automatic Resolution = 0.1pm; Minimum Manual Resolution = 0.001pm

6.2 JDSU Fiber Bragg Grating

The etched fiber Bragg grating sensor was fabricated from a commercially-available grating from JDSU. Packaged in an unknown housing, the component included two FBGs at different wavelengths. The gratings were approximately 5mm long and

separated by 1cm. The unetched central Bragg wavelengths were 1533nm and 1563.8nm. While the specifications of the fiber and grating designs are unavailable, various diagnostics reveal probable specifications. For example, the grating transmission and reflection spectra were acquired with the tunable laser set-up. The gratings were determined to have a peak reflectivity of 30dB and extremely well-suppressed sidelobes. The gratings are likely superimposed chirped FBGs, consisting of three overlapping gratings, used for optical communications multiplexing with flat group delay.

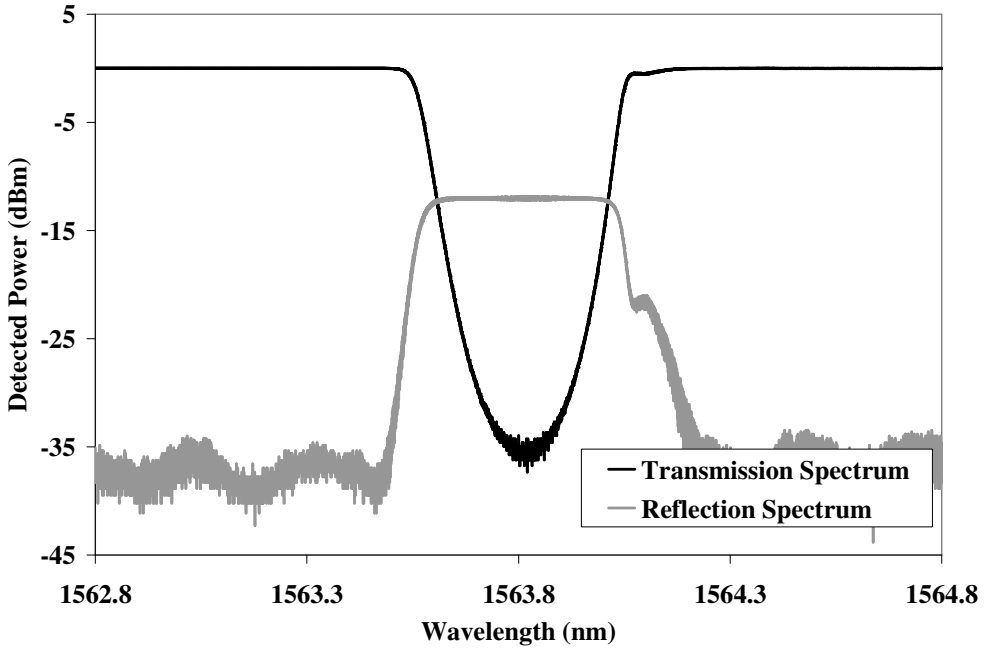

Figure 6.2.1 Transmission and reflection spectra of the JDSU sensor. Spectra were acquired before etching. Wavelength resolution = 0.1pm.

Attempts to inscribe additional gratings on the same fiber as the JDSU FBG formed weaker gratings than with the boron co-doped fiber. For an equivalent method and exposure, gratings written in the JDSU fiber displayed maximum reflectivities of 90%. Additionally, measurements from designing a temperature-compensated mounts reveal that the JDSU fiber has a thermo-optic coefficient of 9.8×10^{-6}. The JDSU fiber is

likely plain germanosilicate fiber that has likely been hydrogen loaded to enhance photosensitivity. Thermal annealing is used to remove the OH-bond absorption and increase the lifetime of hydrogenated FBGs.

Both FBGs are packaged in a single temperature-compensated mount. When the fiber is unetched, the FBG sensitivity to temperature fluctuations is -0.1pm/°C within 10°C from room temperature.

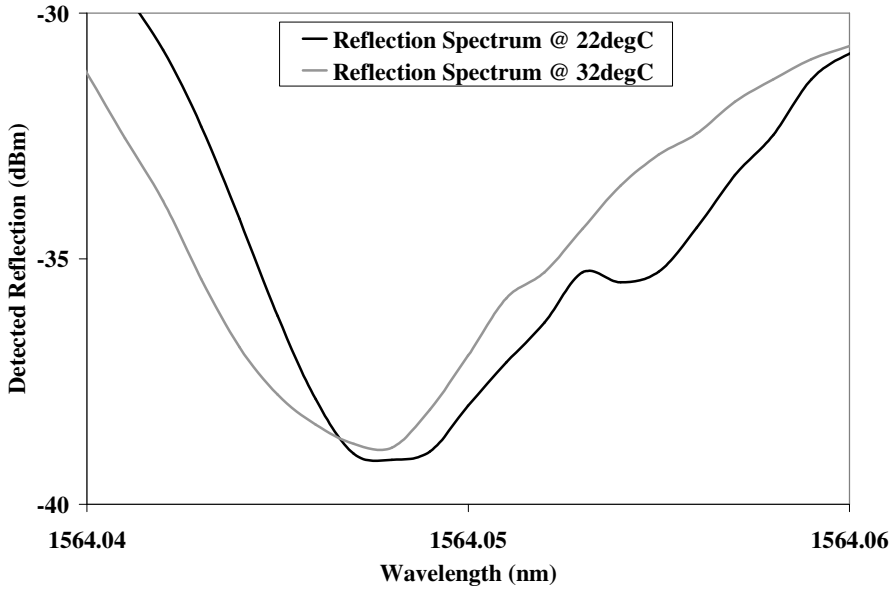

Figure 6.2.2 Spectral features in the reflection spectra for the unetched JDSU sensor and room temperature and ten degrees above room temperature. The average temperature sensitivity through the spectrum was -0.1pm/°C.

6.3 Etched Fiber Bragg Grating

Fabricating the etched FBG sensor starts with a two-step chemical etch. Fiber etching was conducted in 7:1 buffered oxide etch with surfactant from J. T. Baker. According to the M.S.D.S, the solution is comprised of 0.5%-10% hydrogen fluoride, 40%-70% water, 30%-50% ammonium fluoride, and 0.5%-10% surfactant.

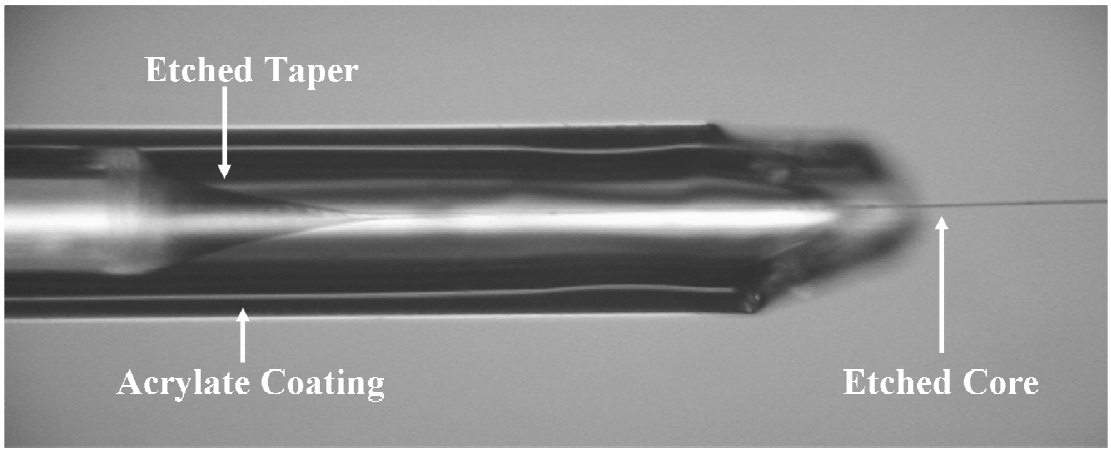

Figure 6.3.1 Photograph from an optical microscope showing the etched fiber taper

The low concentration of hydrogen fluoride and the addition of surfactant reduce the silica etch rate and enhance surface smoothness. Coupling losses and poor cavity finesse are exacerbated by surface roughness and need to be kept to a minimum. The etch rate is very stable for fixed temperature and at 23°C the fiber etch rate is 10.9µm/hr. Etch rates vary with temperature and will vary by more than 2% per degree. Primary etches involve fully immersing the sensor within the etchant for 7 hours. The diameter is changed from 125µm to 49µm. During the secondary etch, the lower grating is immersed in etchant and the upper half of the housing remains in air. The diameter is reduced from 49µm to the final etch diameter within 3.5hr-4.5hr. Lab temperatures were generally constant throughout the 11hr etches. Even though etch rates are very uniform and reproducible, the final fiber diameter is determined through optical interrogation of the FBG. Using the results discussed in Chapter 3, the fiber's effective index can be determined when the cladding and several microns of the core have been replaced by a low index solution. For the JDSU fiber, with core index of 1.4708, the central Bragg wavelength shifts by 10.5nm from the initial, unetched position once the fiber diameter is 5µm.

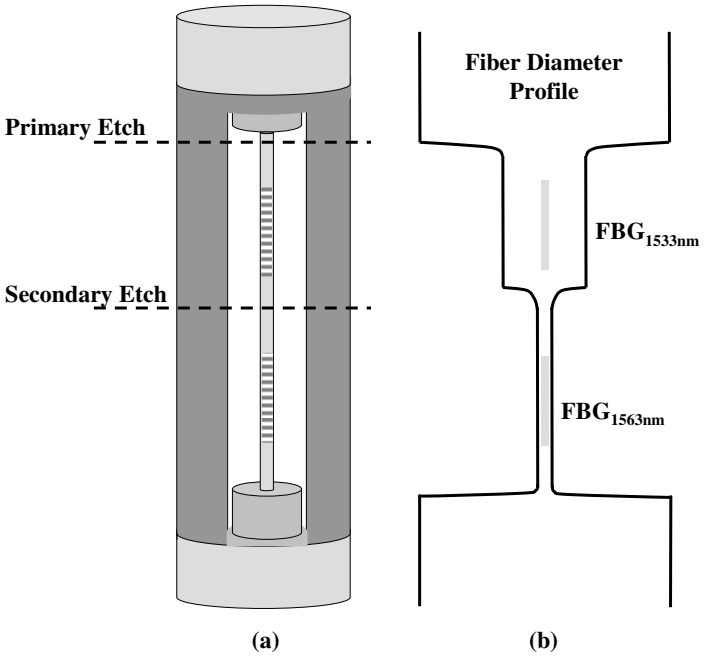

Figure 6.3.2 (a) Diagram of the JDSU fiber housing and positions of the etchant during primary and secondary etches; (b) fiber diameter profile after secondary etch

Since the sensitivity of the fiber depends heavily on the fiber diameter, fibers were consistently removed from etches when the Bragg wavelength blue-shifted from 1563.8nm to 1553.3nm. Monitoring the reflection spectra during etching revealed two distinct trends. Between 125µm and 40µm fiber diameters, the Bragg wavelength red-shifted with an increasing rate until saturating approximately 200-500pm from the initial Bragg wavelength. Since the fiber is under tension while etching, the tension only remains constant if the fiber diameter is uniform throughout the entire length. During primary etching, the entire fiber housing is being immersed in etchant, however the liquid surface tension often prevents the etchant from reaching both ends of the exposed fiber. The unetched portions remain thicker and therefore transfer more tension to the etched regions, red-shifting the Bragg wavelengths of both gratings. This strain effect eventually competes with the fiber's increasing sensitivity to the environmental refractive index. For fiber diameters of 40µm, the optical mode begins to penetrate the cladding-

liquid interface and changes the Bragg wavelength. During this time, the rate of blue-shifting increases since the RI sensitivity is non-linear with fiber diameter (refer to Fig. 2.4.7). The taper between 49µm and 20-30µm also serves as an optical mode converter. At this point during etching, the first higher order mode emerges on the low-wavelength portion of the spectrum. The intermodal coupling efficiency varies and is not specifically controlled by the etching technique. Higher order modes have been shown to be more sensitive to effective index changes [Ref. 6.3.1] than lower order modes, yet exhibit the same sensitivity to strain and temperature changes.

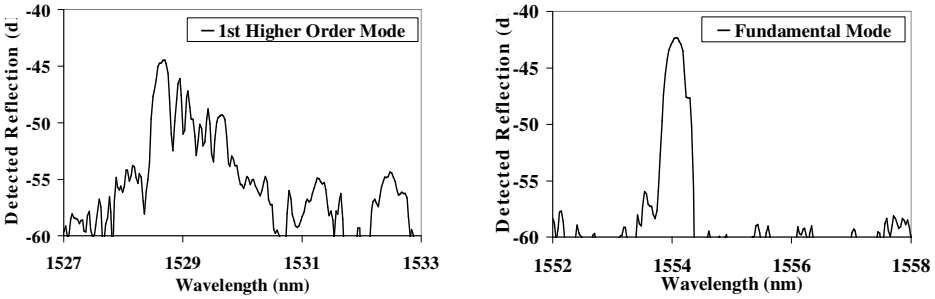

Figure 6.3.3 Reflection spectrum obtained with the OSA set-up for the etched FBG modes (a) higher order and (b) fundamental.

6.4 In-house Fiber Bragg Gratings

In-house fiber Bragg gratings are made on Newport's boron co-doped photosensitive fiber with a Lambda Physik LPX-250T. The optical path is shown in the figures below. The pulsed, 248nm output is deflected into an exposure chamber, where three apertures only allow the most uniform portion of the beam through to the phase mask. After passing through a UV-grade cylindrical lens, the beam is narrowed in the direction perpendicular to the phase mask pitch.

Figure 6.4.1 Photograph of the LPX-250T excimer output and the beam path into the exposure chamber. A dielectric UV mirror deflects the beam.

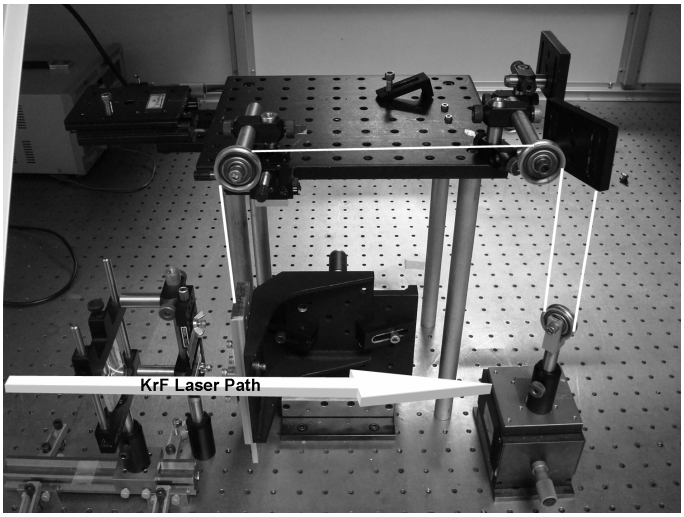

Figure 6.4.2 Photograph of the FBG writing set-up from the side. Upper: tensioning stage, fiber preparation platform, and pulleys. Lower: cylindrical lens, variable aperture, phase mask, fiber mount, and tensioning weight. Note: fiber is embellished for clarity.

The phase mask pitch is oriented vertically because the KrF beam is more coherent in the vertical transverse direction than the horizontal [Ref. 6.4.1]. The fused silica, 248nm phase mask was purchased from Ibsen Photonics and has a grating pitch of 1062nm. Fibers are placed on a custom mount that securely holds the fiber in contact-mode with the phase mask.

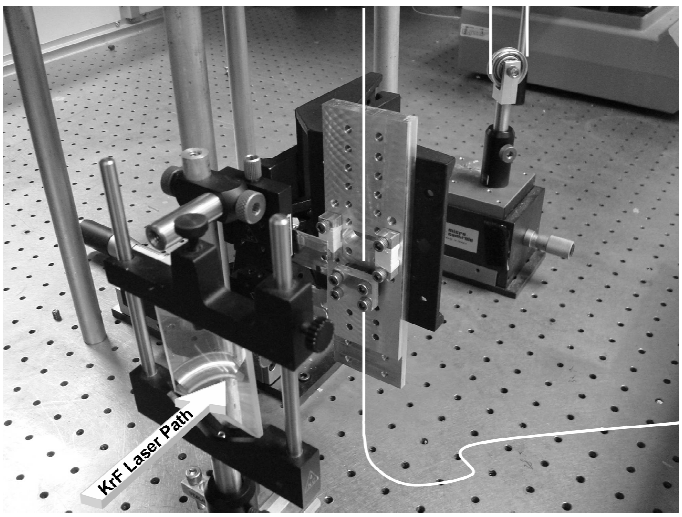

Figure 6.4.3 Photograph shows the FBG writing set-up from a perspective. The custom mount holds the fiber under tension and the phase mask in contact mode with the fiber. Note: the fiber is embellished.

The relative position between the fiber and phase mask is adjusted by allowing the upper pulley to translate in both directions horizontally. The pulley system above the fiber mount maintains tension on the fiber throughout grating writing. FBGs written under tension will have blue-shifted Bragg wavelengths (approx. 1nm for 100g weight) when relaxed.

Grating writing is monitored in real-time with the Agilent tunable laser system. For ultra-high finesse Fabry Perot cavities, the grating reflectivity should exceed 99.7%. Typically, the minimum transmission levels reached -25dB after several hundred exposures. The transmission dip grew at slower rates after 1000 exposures and gratings were written with 2000-3000 exposures with a 4Hz repetition rate. Both reflection and transmission spectra were acquired during the writing process. The bandwidth of the reflection spectrum and the depth of the transmission spectra indicate the grating quality. Transmission depths appear to be augmented by additional grating losses, which can reduced by thermal annealing and will be discussed in Section 6.6. The FSR and finesse

values make for more reliable indicators of reflectivity than the depth of the transmission spectrum. The peak of the grating's reflection spectrum shows whether the reflectivity is greater than 95%, but does not provide further information.

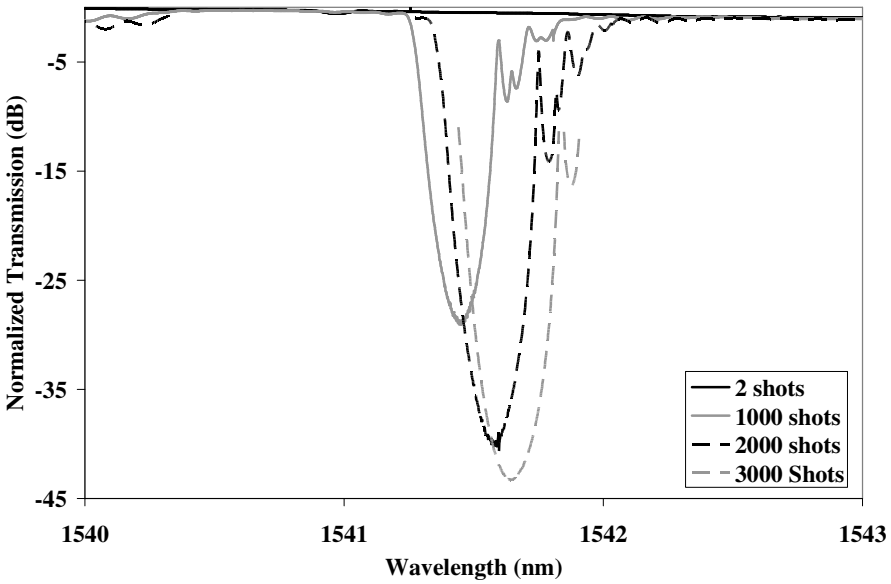

Figure 6.4.4 Transmission spectra during continuous grating writing. The "2 Shots" transmission spectrum is barely noticeable and centered at 1539.95nm. The rate of Bragg shifting and grating strengthening saturates for longer exposures.

For strong gratings, the spectral bandwidth is linearly proportional to the index contrast. The Bragg shift will be a measure of how the average refractive index increases per excimer pulse. For high quality gratings, the slope of FBG bandwidth versus Bragg shift should be maximized. Steep slopes indicate that the index modulation is steady and deep. Fig. 6.4.5 uses data from writing FBGs on two separate fibers with identical techniques and laser fluences. The data was acquired with the exact same phase mask technique and used the Lambda Physik 250T. The trends in Fig. 6.4.2 will have different slopes based on the photosensitivity of the fiber.

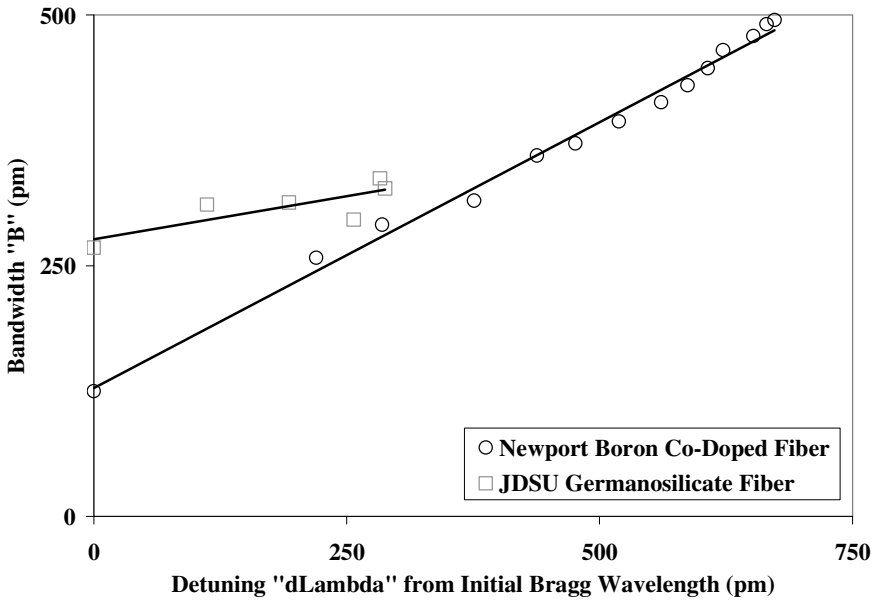

Figure 6.4.5 Plots of how the average effective index changes with index contrast in FBGs written in a germanosilicate fiber and a fiber co-doped with boron. Data from single measurements.

6.5 **In-house Fiber Fabry Perot**

Fiber Fabry Perot cavities are created from the fiber Bragg gratings discussed in Section 6.6. The gratings are spaced with a Newport translation stage set-up that moves the fiber with respect to the phase mask. The UV beam and phase mask are maintained at the same elevation when writing both gratings. For longer cavity lengths (~2-4cm), a custom mount is able to hold the fiber inside or outside of the cavity so that tension may be applied to or removed from fiber during the inscription of a second grating. If tension is removed from FBG1 during the inscription of FBG2 then the FBG2 spectrum does not interfere with the FBG1 spectrum once FBG2 is completed. For short cavity lengths, interfering spectra cannot be avoided and the spectrum of FBG2 must be estimated.

One of the challenges to making high finesse Fabry Perots is overlapping both grating spectra at the peak reflectivity. The difficulty is in monitoring the central Bragg wavelength of FBG2 when the FBG1 spectrum begins to overlap. The Fabry Perot

throughput will be maximized when the two grating reflectivities are equal, but practical FP fabrication is not as straightforward. In addition to having wavelength-dependent reflectivity, mechanisms that create fiber loss compete with maximizing throughput. Fig. 6.5.1 shows the spectrum of FBG1 and the spectrum after a second grating has been inscribed with an FBG spacing of 800μm.

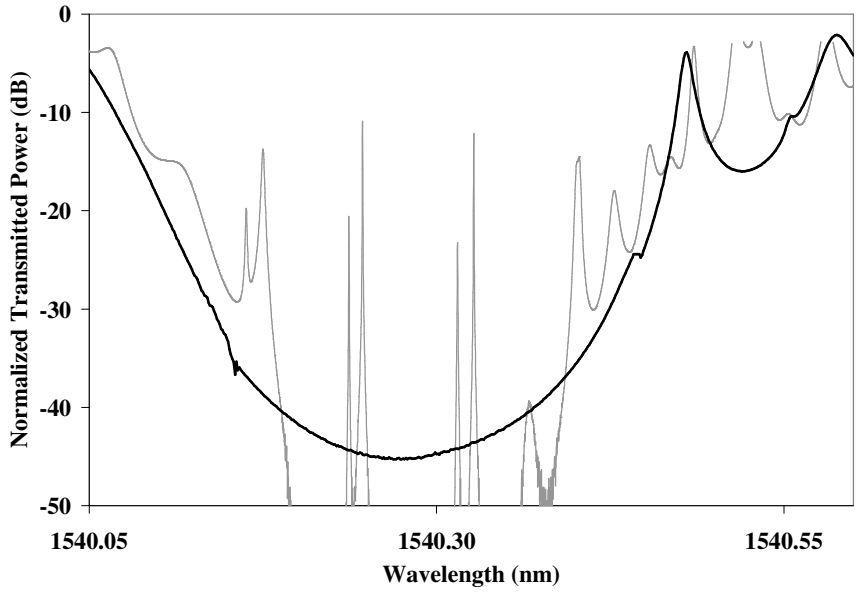

Figure 6.5.1 Comparison between the transmission spectrum of the first of two FBGs written for a fiber Fabry Perot and the associated FFP transmission spectrum.

The first FBG spectrum has a minimum transmission of -45dB, normalized to the transmitted power at 1550nm. FBG1 was written under tension and after the fiber had been moved to create an 8mm cavity. The tension was then reapplied so that the central Bragg wavelength was returned. For an ideally uniform beam and unmoving alignment between the fiber and phase mask, the FBG2 spectrum would be identical to the FBG1 spectrum. Practical experiments did not show this level of reproducibility. However, the Bragg wavelength was measured at the onset of grating formation (i.e. 1-3 pulses of KrF laser radiation) to estimate the number of shots required to shift the average effective

index by the same amount as FBG1. The FFP transmission spectrum in Fig. 6.5.1 would be broadened with respect to the FBG1 spectrum if the two grating spectra did not overlap reasonably well. As expected, the resonances near the center of the FFP spectrum display greater finesse. The FFP data was obtained after thermal annealing. Thermal annealing will be shown to improve FFP throughput while leaving finesse unchanged.

The in-house FFPs also form doublet resonances. These doublets arise from fiber birefringence. Polarization within the fiber changes as it propagates down the length, so within the grating region the light is randomly polarized. With birefringent fibers, each polarization will propagate with a different effective index and thus the Fabry Perot resonance wavelengths will be slightly offset for each. The separation between the polarizations measures the amount of birefringence, whereas the difference in throughput for each resonance indicates either that there is more light in one particular polarization or that the FBGs preferentially reflects one polarization over the other. The latter effect has been documented to occur for side-written FBGs like those fabricated in our lab [Ref. 6.6.1]. Additionally, boron co-doped fibers are known to be more birefringent because of the lattice deformations introduced by boron sites.

Ultimately, high finesse fiber Fabry Perot cavities offer the highest resolution refractive index sensing and thus are an important figure of merit. In a recent experiment, the FBG spacing was shortened to 300μm and the FFP resonance naturally appeared at the center Bragg wavelength. This situation provided the circumstance of our highest finesse FFP to date. The spectrum is included in Fig. 6.5.2. With such a short cavity length, the FSR is larger than the bandwidth of the FBG spectra. In Section 5.4,

the finesse is plotted against the detuning of a 30dB FBG. Since the reflectivity changes with detuning, the effective length also changes with detuning and thus the FSR changes. In order to solve for the finesse in a self-consistent manner, a graphical solution was used to find common solution between the general expression for Fabry Perot finesse in terms of FBG reflectivity and the experimental linewidth.

$$Finesse = \frac{\pi}{2}\sqrt{\frac{4R}{(1-R)^2}} = \frac{FSR}{\Delta\upsilon} = \frac{\lambda^2}{2n\Delta\upsilon \times \left(L_c + 2L_{FBG}\left(\frac{\sqrt{R}}{2a\tanh\sqrt{R}} \right) \right)}$$

(6.5.1)

In Eqn. 6.5.1 the experimentally measured values are λ, L_c, L_{FBG}, n, and Δν. The solution to this equation is independent of scattering losses and provides the value of R that agrees with the linewidth and the other measured quantities above. Fig. 6.5.2 shows the raw data of the high finesse spectrum and Fig. 6.5.3 shows the graphical solutions to finesse.

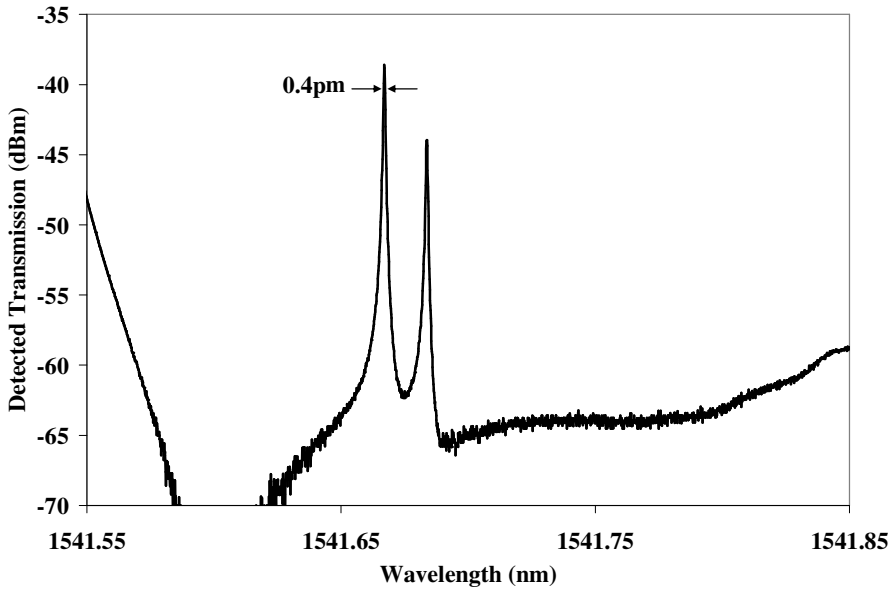

Figure 6.5.2 Transmission spectrum of extremely high finesse fiber Fabry Perot comprised of two fiber Bragg gratings.

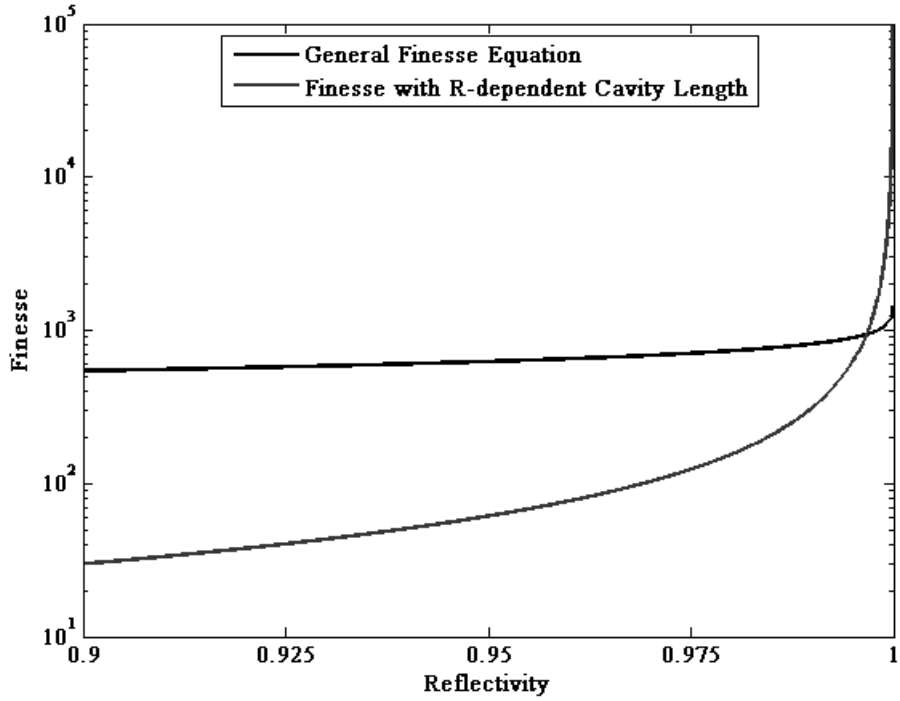

Figure 6.5.3 Graphical solution of the finesse from the spectral data in Fig. 6.5.2. The finesse is determined to be 942 and the reflectivity to be -24.8dB.

In a FFP with grating spacing of 8mm, four resonances fit within the bandwidth of the FBG spectrum. The transmission spectrum is plotted in Fig. 6.5.1 and Fig. 6.5.4 contains a plot of how the FSR changes with detuning. Note that the slight curvature of the FSR with detuning is similar to the theoretical FSR variation of a 30dB grating (refer to Fig. 5.4.3). The throughput of resonances with further detuning from the central Bragg wavelength is too small to measure the FSR accurately.

In summary, experimental finesse values range from 500-1000 with strong dependence on the UV laser fluence. If multiple resonances fall within the bandwidth, the finesse will vary drastically from one to another. Resonances near the center will exhibit the greatest finesse and the sharpest linewidths. Thermal annealing may be an effective means to tune the resonances so that there exists at least one resonance within a narrow range at the center of the FFP spectrum.

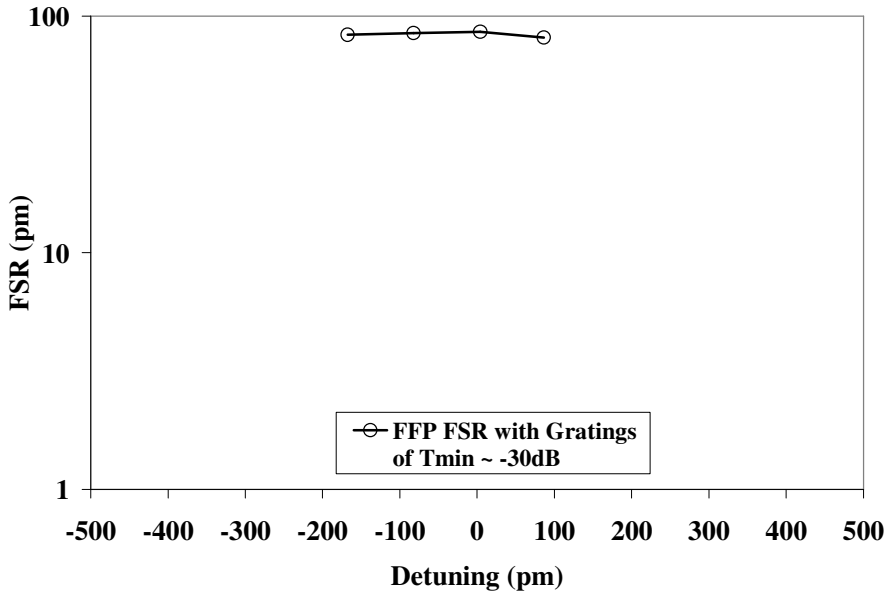

Figure 6.5.4 Plot of the FSR versus detuning for the FFP created in our lab. The grating reflectivities are approximately 25dB each.

6.6 Thermal Annealing

Typically high-temperature thermal annealing is a process used to either pre-treat or post-treat a hydrogenated fiber to either reduce loss or increase FBG lifetime. Lower-than-expected throughput and poorer finesses indicate that grating losses might be contributing to the unexpected grating characteristics. The infrared absorption in our boron co-doped fiber is 0.1dB/m. Off-resonant transmission was monitored during grating writing to confirm that some broadband losses were being introduced due to the writing process. In a 2000 shot FBG, the off-resonance transmission dropped 0.1dB. These scattering losses are not necessary evenly distributed throughout the entire grating and therefore cannot be treated like typical background loss. For each writing process, scattering losses will impact Fabry Perot characteristics differently based on the degree to which light interacts with the lossy portions of fiber.

Fibers are placed in a V-groove copper oven atop a digital hot plate for annealing. The plastic coating is stripped away from the FFP cavity region because at such hot temperature, plastic becomes less elastic and therefore less useful as a fiber coating. Fibers are annealed for 30 minutes at 250°C while the reflection and transmission spectra are monitored. The effects of annealing are summarized in Fig. 6.6.1.

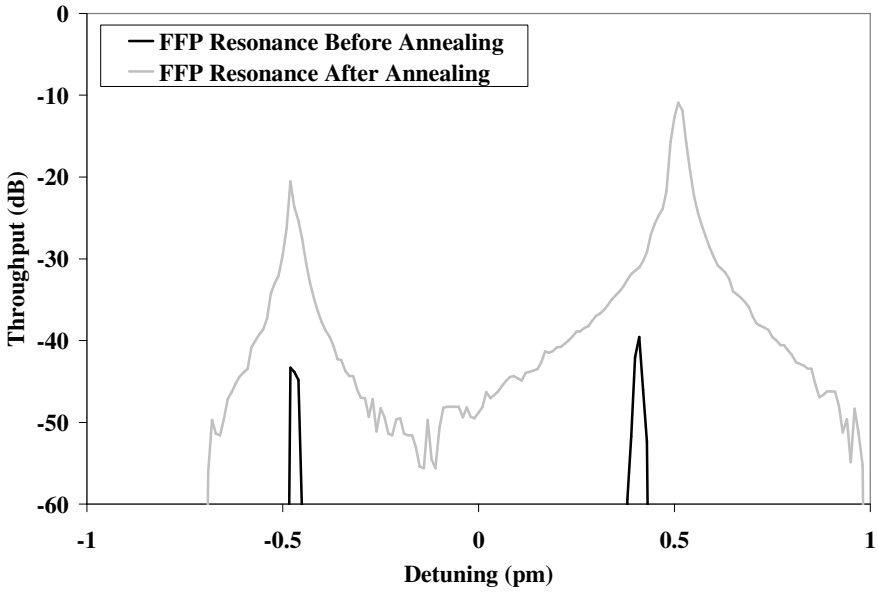

Figure 6.6.1 Fabry Perot resonance transmission spectrum before and after thermal annealing at 250°C for 30 minutes.

In addition to improvements of the finesse, thermal annealing also changes the effective modal index. In annealed fiber, the central Bragg wavelength blue-shifts with respect to pre-annealed fibers. Furthermore, the polarization splitting due to fiber birefringence changes due to annealing. The Bragg wavelengths of the overall FFP spectrum shift by -128pm due to annealing. This Bragg shift is associated with an induced refractive index shift of 6.3e-5 riu.

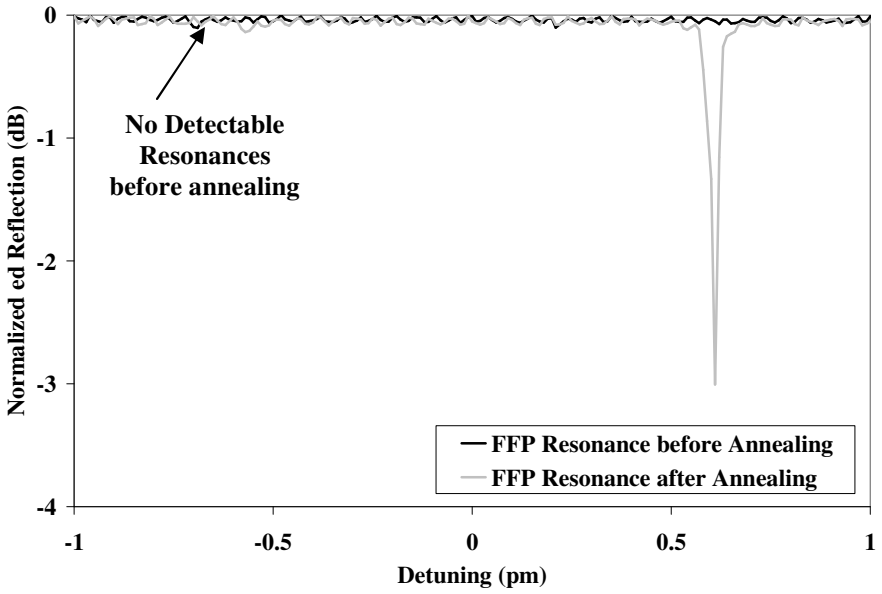

Figure 6.6.2 Fabry Perot resonance reflection spectrum before and after thermal annealing at 250°C for 30 minutes.

Polarization splitting increases from 8.9pm to 9.9pm due to thermal annealing. This increase is due to a shift in the cavity's effective index of 9.4e-7 riu.

$$\Delta\lambda_{Bragg} = 2\Delta n_{eff,FBG}\Lambda_g$$

$$\Delta\lambda_{FP} = \frac{\Delta n_{eff,cavity}\lambda_{FP}}{n_{eff,cavity}}$$

The cavity was 9.6mm and the gratings were 7.4mm each. Since the refractive index shifts were greater in the FBGs than in the cavity, photoinduced scattering losses were reduced by thermal annealing.

Improving throughput is the primary motivation for thermal annealing. Reducing mirror loss will improve throughput throughout the spectrum. Since reflectivity determines how far light penetrates into the grating region, reflectivity also determines how the throughput changes across the FFP spectrum. Fig. 6.5.3 not only shows that the throughput increases for each resonance but that the flatness increases across the

spectrum. Annealing became a regular procedure to prepare the Fabry Perot before continuing with sensor fabrication.

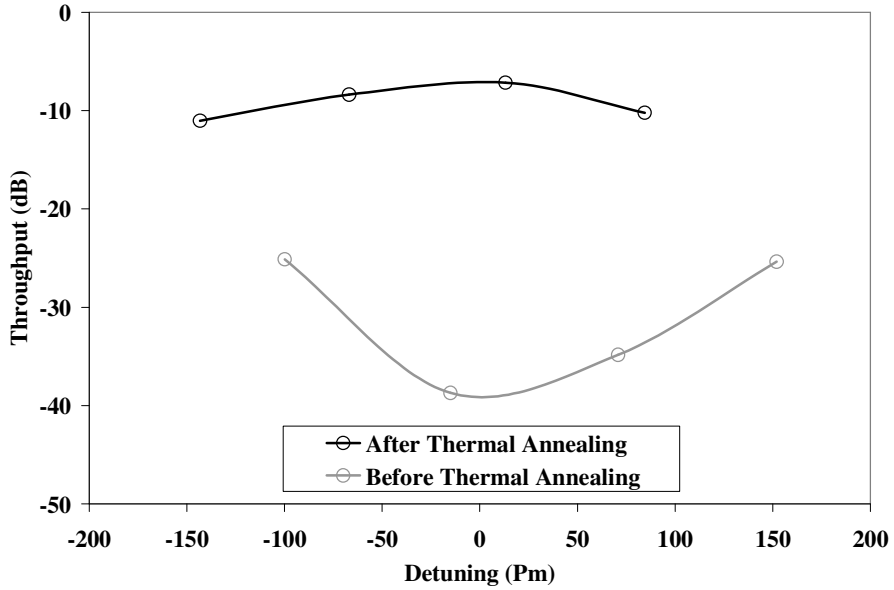

Figure 6.6.3 Effects of spectral detuning on the FFP throughput. Primary factors for nonuniform throughput are reflectivity mismatching and mirror losses. Annealing improves the throughput and the throughput uniformity by reducing mirror losses.

6.7 Fiber Fabry Perot Etching

Experiments with etching the Fabry Perot cavity are recent and still in development. Some LPG Fabry Perot refractive index sensors have been fabricated to be etched only within the cavity. This design does not utilize the sensitivity of the etched FBG. Our idea is to etch the cavity and FBGs together so that there are no tapers within the cavity. Tapers cause coupling losses and losses between the gratings, which will degrade the FFP finesse. In multiple early attempts to etch the gratings and cavity, the finesse has been maintained at least until the fiber diameter is approximately 25µm. At that diameter, the evanescent field begins to penetrate the surrounding solution and there are measurable taper losses.

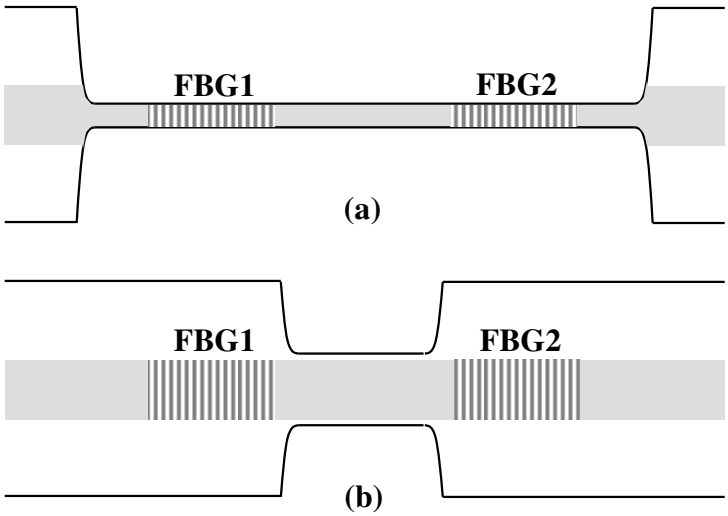

Figure 6.7.1 Diagram of the etched FFP diameter of (a) our sensor and (b) another sensor of similar design [Ref. 6.7.1]

FFP finesse seems to degrade at a certain point during etching. It is believed that surface roughness may induce scattering within the cavity and/or nonunform etch rates may remove the spectral overlap of the two FBGs. One proposed solution is to thermally anneal the etched FFP to reduce the surface roughness. The etched spectrum does still contain Fabry Perot resonances with high throughput but low finesse. Figs. 6.7.2 and 6.7.3 show the FFP spectrum through the first 100μm of etching and the final spectrum in a deionized water rinse.

The new sensor was removed from etchant after the Bragg wavelength had shifted by 10.3nm and the diameter was expected to be 5μm. Upon removing the fiber from etchant, the sensor is rinsed in a 30mL volume of water so as to prevent further etching. The transition between environments caused a 600pm shift in the central Bragg wavelength of the sensor.

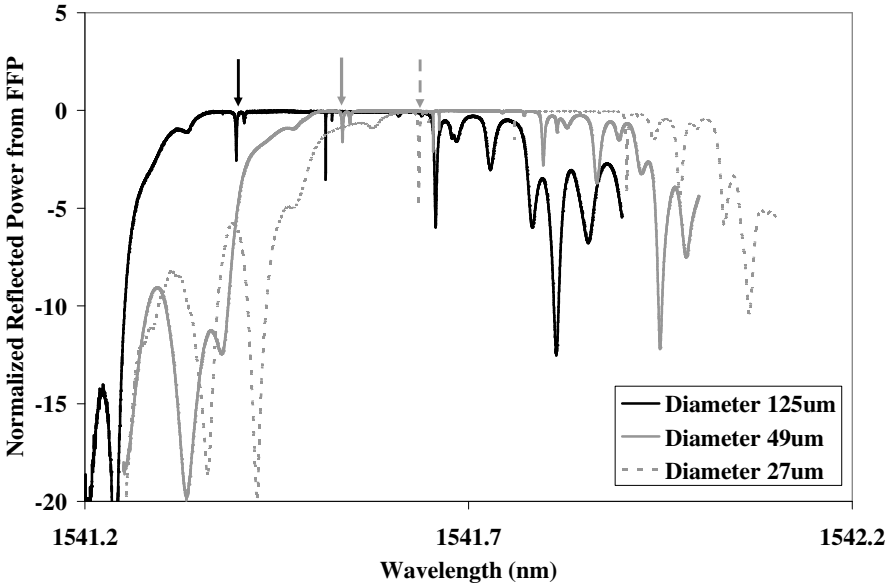

Figure 6.72 Normalized reflection spectra of the FFP while the gratings and cavity are etched from 125 µm to 27µm. Arrows indicate Fabry Perot resonances with constant finesse.

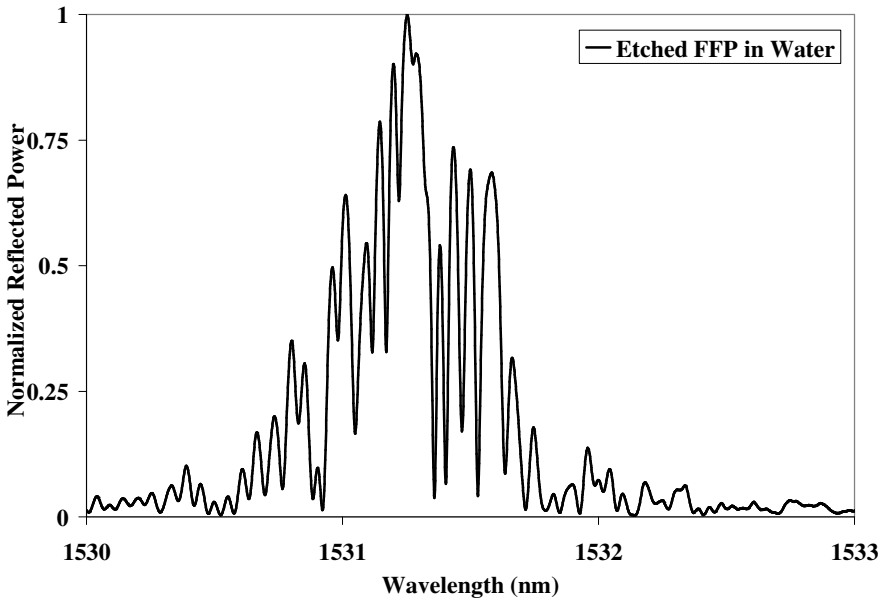

Figure 6.7.3 Normalized reflection spectrum of the etched FFP in water.

The FBGs in the etched FBG sensor are 5mm long. The FFP sensor is between 2 and 5cm long. Uniformity in the etch rates along the fiber must be better for etching the FFP and therefore etch baths are larger and temperature control may be introduced in the

future. Etch rates are temperature sensitive and therefore care must be taken to maintain a uniform temperature throughout the etchant.

6.8 Temperature Compensation

The premise behind compensating the spectral shifts of FBGs and FFPs was discussed in Chapter 4; experimental results are discussed below. Testing the temperature compensated mount involved fabricating a grating, mounting the fiber, and directly measuring the Bragg shifts as the sensor's temperature was changed in a large water bath. Lengths of low-CTE metals were held constant as the lengths of the aluminum insets were varied in order to determine the thermo-optic constants of two fibers: a germanosilicate fiber from JDSU and a boron co-doped fiber from Newport. Temperature dependence of a typical, unmounted germanosilicate FBG is between 10-14pm/°C. We achieved temperature compensation that reduces the sensitivity to -0.17pm/°C.

6.8.1 Stainless Steel-Aluminum Mount; JDSU Thermo-optic Constant

Initial designs incorporated stainless steel and aluminum as the low-CTE and high-CTE materials, respectively. Specifically, stainless steel alloy 416 and aluminum alloy 6063 were used. Thermal expansion constants for these metals are 9.9×10^{-6} °C^{-1} and 23.4×10^{-6} °C^{-1} respectively. The length of steel was constant at 3.419" and lengths of the aluminum insets varied between 0.80" and 1.00". Epoxy is used to join the metals at the end of the low-CTE metal. The thin layer of 353ND from Epotek has a CTE of 45×10^{-6} and the thickness was consistently 0.01", as determined by optical microscopy. While 353ND is designed for fiber optics packaging, spot welding between the metals

may improve temperature stability in the future. Using Eqn. 6.8.1, the thermo-optic constant of the JDSU fiber was determined by measuring the temperature sensitivity of the mount.

$$\alpha_{Al} \times 2L_{Al} - \alpha_{lowCTE} \times L_{lowCTE} - \alpha_{epoxy} \times L_{epoxy} = \zeta_{FBG} \qquad (6.8.1)$$

$$\left(23.4\times10^{-6}\right)\left(2L_{Al}\right) - \left(9.9\times10^{-6}\right)\left(3.419\right) - \left(45\times10^{-6}\right)\left(0.1''\right) = \zeta_{JDSU} \approx 9.8\times10^{-6}$$

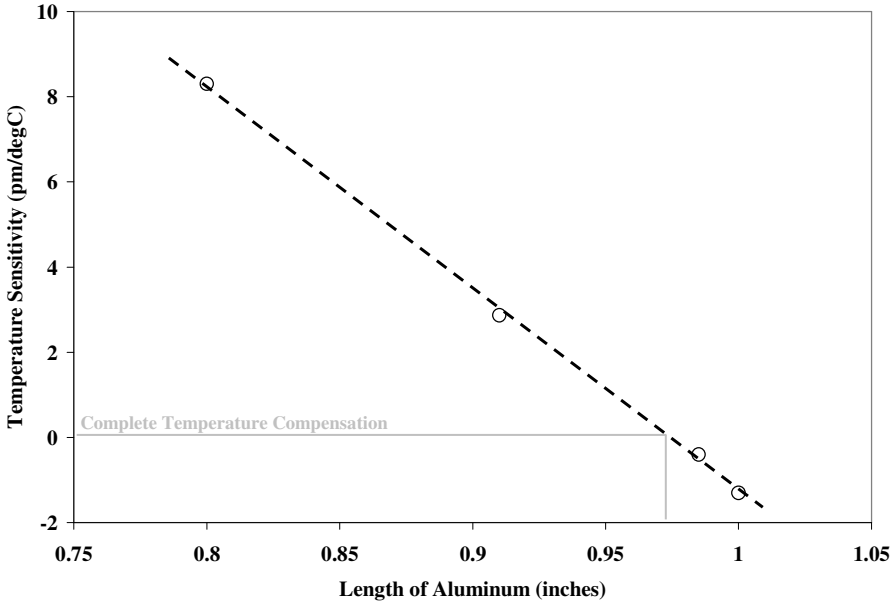

Figure 6.8.1 Temperature sensitivity of a germanosilicate FBG in steel/aluminum mounts with varying lengths of aluminum. The slope indicates a thermo-optic constant of plain germanosilicate fiber of $\zeta_{GeSi}=9.8\text{x}10^{-6}$. Data from single measurements.

The minimum temperature sensitivity measured was -0.4pm/°C. This sensitivity could be improved, though it became apparent that the use of stainless steel was impractical due to the lengths required. The overall mount would have to be over 11cm long in order accommodate a 3cm FFP cavity and 7.5mm gratings. For these longer lengths, a temperature sensitivity experiment was attempted but it was obvious that temperatures were not uniform throughout the 11cm mount and thus temperature compensation failed. To reduce the mount size, the difference between thermal expansion constants of the low-

CTE and high-CTE had to be greater. Invar is an ideal metal for this application and, while exotic, has been used extensively in high-temperature aerospace applications.

6.8.2 Invar-Aluminum Mount; Newport Thermo-optic Constant

Design for the Invar-Aluminum temperature-compensated mount was exactly the same as with stainless steel. Invar36 was purchased as a 1/8" rod. The Invar rod was machined to flatten the ends and two sides so that the aluminum insets joined properly. The length of Invar was constant at 2.294" and the lengths of aluminum were varied. Invar was purchased from ESPI High Performance Metals and the quoted CTE for their Invar36 is $1.26\text{x}10^{-6}$ °C^{-1}. Results are shown in Fig. 6.8.2.

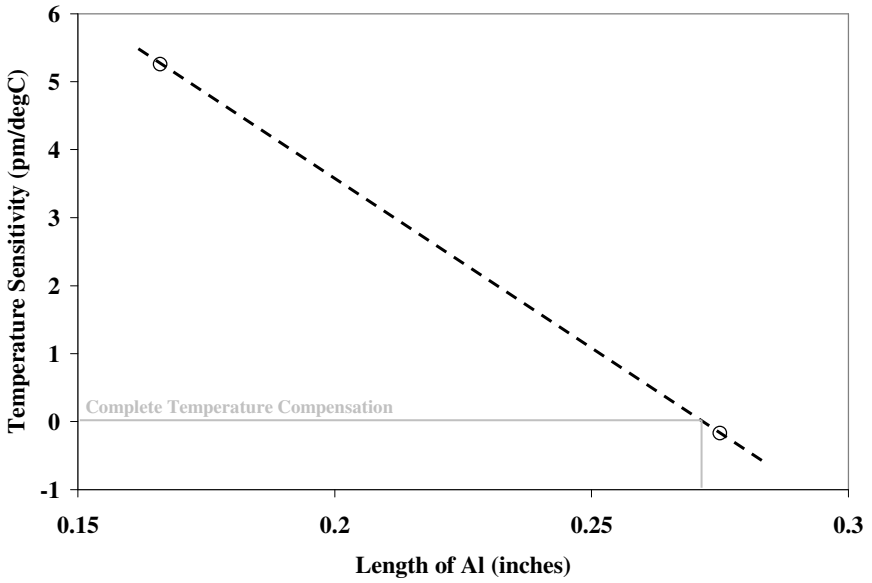

Figure 6.8.2 Temperature sensitivity of a germanosilicate boron co-doped FBG in Invar/aluminum mounts with varying lengths of aluminum. The slope indicates a thermo-optic constant of Newport F-SBG-15 fiber of $\zeta_{GeSi\text{-}B}=8.9\text{x}10^{-6}$. Data from single measurements.

$$\left(23.4\times10^{-6}\right)\left(2L_{Al}\right)-\left(1.26\times10^{-6}\right)\left(2.294\right)-\left(45\times10^{-6}\right)\left(0.2''\right)=\zeta_{JDSU}\approx8.9\times10^{-6}$$

The Newport fiber's thermo-optic constant was determined to be lower than the germanosilicate fiber's, which was expected from the boron co-doping. Also, the

temperature sensitivity is reduced to -0.17pm/°C, which is of the same order as the commercially available JDSU housing. With such low temperature sensitivity, wavelength shifts can be corrected to within 0.017pm, which is the 20 times larger than the Agilent tunable laser's linewidth. Temperature compensation works and is implemented in the sensor fabrication.

6.8.3 Thermo-optic Constant of Solutions

If the wavelength resolution is not limited by thermal effects on the silica itself, then the temperature effects on liquids used in sensing must be considered. In calibrating the etched fiber Bragg grating sensor, the Bragg wavelength was monitored over a range of temperatures for water and ethanol. Temperature is again measured with a YSI thermistor. Raw data is processed by compensating for the effect in each solution. For example, the thermo-optic constant for water was determined to be $-8\text{x}10^{-6}$ °C^{-1}.

The wavelength data may be corrected accordingly:

$$\Delta\lambda_{B,temperature} = \lambda_B\left(\frac{1}{n_{eff}}\frac{\partial n_{eff}}{\partial T}\right)\Delta T \qquad (6.8.2)$$

$$\Delta\lambda_{\min imum,water} \approx \zeta_{water} \times S \times \Delta T \qquad (6.8.3)$$

$$\Delta\lambda_{\min imum,water} \approx 15\frac{nm}{riu}\left(8\times10^{-5}\,\frac{riu}{°C}\right)(0.1°C) = 0.12\,pm$$

Eqn. 6.8.3 depends on the sensitivity (S), thermo-optic constant of water (ζ_{water}) and temperature resolution. The thermo-optic constants of ethanol and methanol were measured using the same technique to be $-6.8\text{x}10^{-5}$ °C^{-1} and $-8.6\ \text{x}10^{-5}$ °C^{-1}, respectively. While the accuracy of determining local temperatures may be improved with higher resolution thermometers, practical RI sensing of chemical processes is limited by the temperature uniformity and convection within the liquid solutions.

Chapter 7: Bulk Refractive Index Sensing

The data presented and discussed in Chapters 7 and 8 are wholly acquired with the etched FBG sensor. The etched FFP sensor is still in development and has not been thoroughly tested. Furthermore, previous work with the etched FBG may be found in various journals [Ref. 7.1.1, 7.1.2, 7.1.3]. Generally, the Bragg wavelength of the etched fiber's fundamental mode is monitored when the sensor is immersed in homogeneous solutions. However, the first higher order mode appears on the low-wavelength portion of the spectrum provides greater sensitivity at solution indices near common solvents. In addition to calibrating the sensor with refractive index solutions known as Cargille liquids, the sensor is also used to measure the refractive index of solvents and solutions. BPM calculations are used to provide a theoretical basis for the index shifts.

7.1 High Index Solutions

As shown in Chapter 4, the maximum Bragg sensitivity to refractive index changes occurs as the RI of the surrounding solution approaches the core index. For the etched JDSU fiber Bragg grating sensor, the core index was determined to be 1.4708. In order to test the sensor's RI sensitivity, liquid solutions with known index were used.

Cargille Labs provides commercially available high-accuracy refractive index liquids that are comprised of carbonfluorocarbon (CFC) mixtures. The exact mixtures are protected trade secrets but the company revealed that the liquids are miscible and that

by combining two different Cargille liquids, the net index would be a weighted average by volume.

The results below were acquired by my colleague Athanasios Chryssis in the early stages of sensor testing.

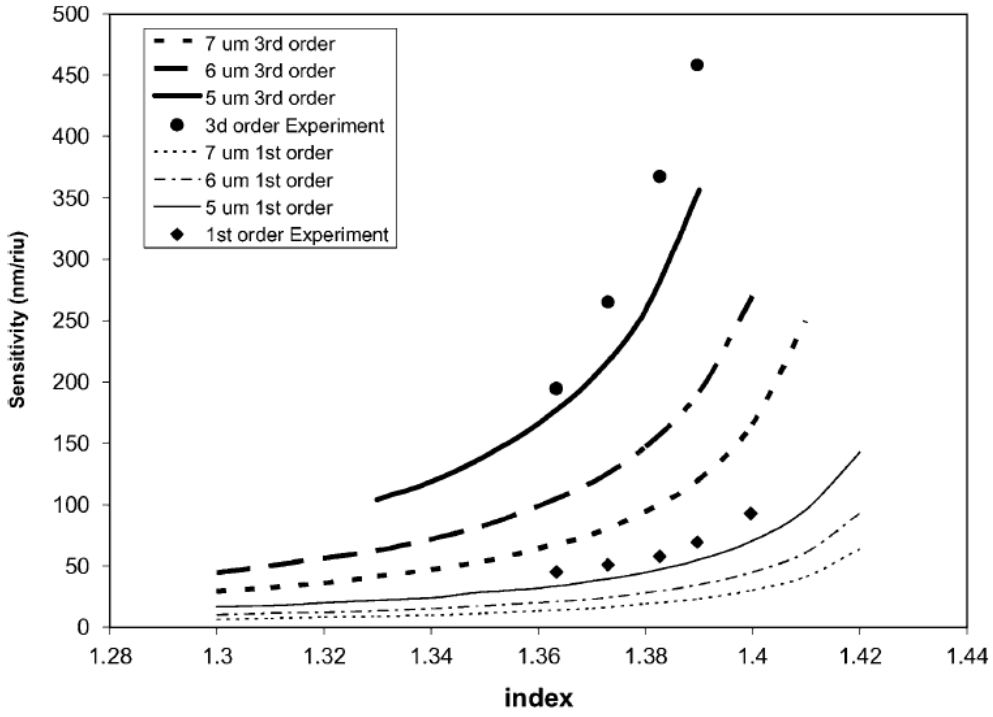

Figure 7.1.1 Experimental and theoretical plots of sensitivity vs. surrounding index. This figure is being used with permission from A. Chryssis [Ref. 7.1.3]

The maximum sensitivity was close to the theoretical limit of 1063nm/riu when the sensor was etched to 3.4μm and the surrounding liquid index approached 1.45.

7.2 Solutions with RI of Common Solvents

BPM calculations were used to theoretically predict the Bragg shifts due to varying surrounding indices. The experiments used an etched FBG sensor with a

diameter of 5µm and only refractive indices between 1.3 and 1.37 were considered. A YSI thermistor with ΔT=0.1°C was immersed in solution near the grating at all times. Wavelength data is corrected for temperature fluctuations in solution.

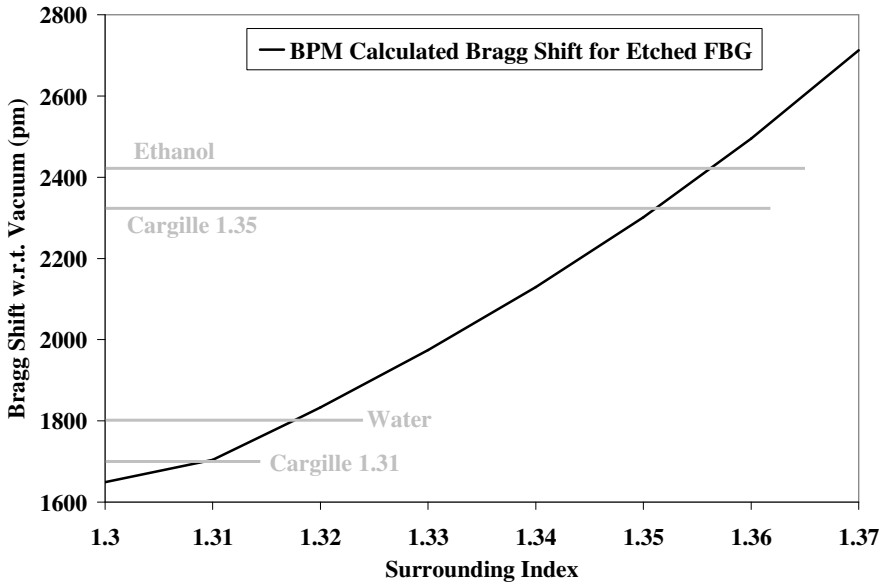

Figure 7.2.1 Bragg shifts were measure with respect to a water reference. The Bragg shifts are compared to BPM-calculated shifts

The refractive index of all solutions depends on wavelength. Sellmeier coefficients indicate how the refractive index varies with wavelength. For water, Sellmeier coefficients are well-known and therefore all of the refractive index measurements of our sensor are referenced to water. Fig. 7.2.1 plots the Bragg reference with respect to vacuum. From these Bragg shifts we may use low-index Cargille liquids to verify the sensitivity of the sensor. For mixtures and solvents of unknown index, this plot may be used to determine the refractive index. For example, ethanol does not have well-documented Sellmeier coefficients like water. The commonly-published index for ethanol is 1.359 though this is for visible wavelengths used in typical refractometers. At

1550nm, out sensor measures the refractive index of ethanol to be 1.356. Determining the index of mixtures will be discussed in Chapter 8.

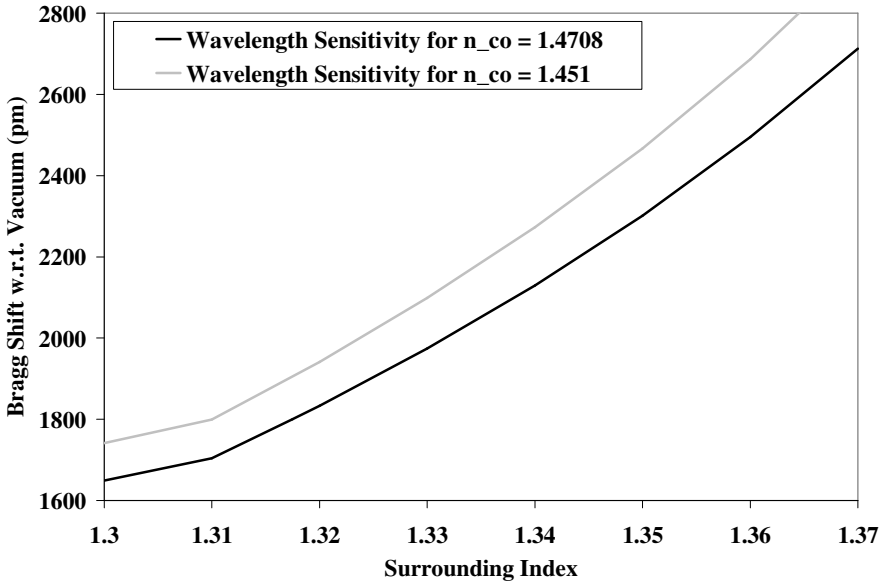

Figure 7.2.2 Comparison between the etched JDSU plot and the FBG shift expected from the boron co-doped FBG sensor. The two are only slightly divergent in this wavelength range but will diverge more when the surrounding index nears 1.451.

Chapter 8: Multilayer RI Sensing

Our etched FBG sensor testing has focused on the detection of DNA hybridization, monolayer adsorption, and selective binding with proteins. DNA hybridization experiments examined how the refractive index on the fiber surface shifts when complimentary strands of DNA are introduced. In order to immobilize DNA onto the silica surface, the fiber must first be silanized. Investigating DNA hybridization naturally transitioned into studying how siloxane monolayers attached to our fiber's silica surface. Recently, protein conjugation has been examined. Glucose molecules are known to selectively bind to the jack bean protein Concanavalin A at a site within the protein's large structural cavity [Ref. 8.1.1]. The FBG sensor is sensitive enough to quantify the difference between single and multiple molecular monolayers in real-time as they form around the fiber. For the siloxane attachments, BPM models and calculations were used in conjunction with Bragg shifts to quantify the results.

8.1 Silanization

8.1.1 Experimental Results

Silanization of silica glass surfaces is used for a range of applications from water repellents to DNA assays. Initially, silanization was used to functionalize the sensor surface for the attachment of DNA strands. Silanization uses covalent bonds between the hydroxyl groups on a newly etched silica surface and molecules with siloxane groups.

Two examples of siloxanes are shown in Fig. 8.1.1. The primary difference is in the number of groups that are free to bind to hydroxyls. Both molecules in Fig. 8.1.1 will attach to the sensor surface and extend the amines away from the surface. For the single ethoxy molecule, monolayers are expected to form and functionalize the surface with amine groups. For the triethoxy molecule, oligomeric siloxane layers form hydrogen bonds with surface silanols and amine groups alike [Ref. 8.1.2, 8.1.3, 8.1.4, 8.1.5, 8.1.6]

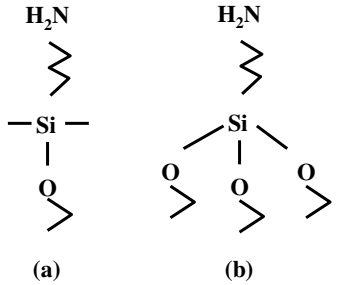

Figure 8.1.1 Structural diagrams of (a) 3-aminopropyldimethylethoxysilane (APDMS) and (b) 3-aminipropyltrithoxysilane (APTES)

The APTES multilayer often becomes disordered and promotes surface roughness, making it difficult to predict the outcome of biological conjugation experiments. APDMS monolayers, in comparison, are dense, highly ordered, and ideal for preparing the silica surface for DNA hybridization experiments. The formation of a multilayer extends a high refractive index material several tens of nanometers from the silica surface and suits the evanescent field sensor.

Attachments were conducted within borosilicate glass test tubes with 5mL volumes. The APTES and APDMS solutions were varied between 0.2% and 3% by volume in either water or ethanol. The concentration of ethanol was 100% throughout the experiments. APTES and APDMS solutions were purchased from Gelest, Inc. and were diluted with a syringe.

Freshly etched FBG sensors were rinsed thoroughly with several 30mL volumes of deionized water. The post-etchant rinse step is used as the reference for the duration of the experiments. Bragg shifts were measured with the OSA set-up described in Section 6.1. Temperature data was recorded from a thermistor that followed the sensor between solutions. Temperature fluctuations were slight and ranged between +/- 1°C. It was observed that temperature fluctuations in ethanol were larger due to evaporative cooling.

For attachments, the sensor was immersed within the 5mL siloxane solution and Bragg wavelengths were monitored immediately. The first in-situ measurements were taken within 30 second and then again at 30 second intervals for 5 minutes. At that time, measurements were spaced to one minute or five minutes depending on the duration of immersion. Generally, attachments were performed and monitored for 30 minutes or one hour. While the Bragg wavelength shifts within the first 30 seconds, measurements were not recorded this early because time had to be taken to carefully position the thermistor in the test tube and near the grating.

At the end of the attachment, the sensor was again immersed in 30mL volumes of water for rinsing. Between experiments, the sensor was heated to 150°C in a custom oven with dry nitrogen flowing over the surface. The sensor had to be cooled after this bake step before being reintroduced to a room temperature liquid, or else the FBG spectrum would drastically degrade. It is believed that sudden cooling caused defects and stresses throughout the silica fiber.

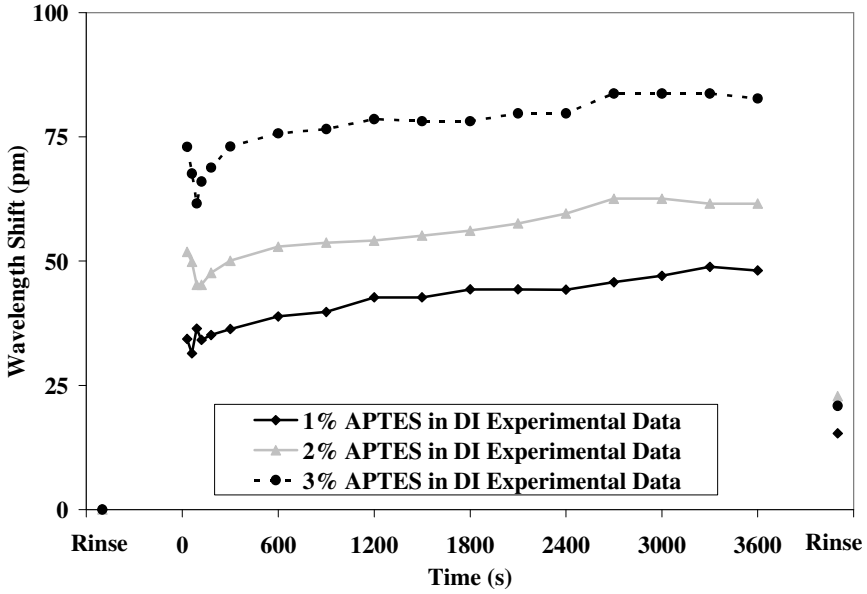

Figure 8.1.2 *In situ* data for silanization with 1%, 2%, and 3% APTES concentrations. Solutions are diluted in water. Silanization data is between 0s and 3600s.

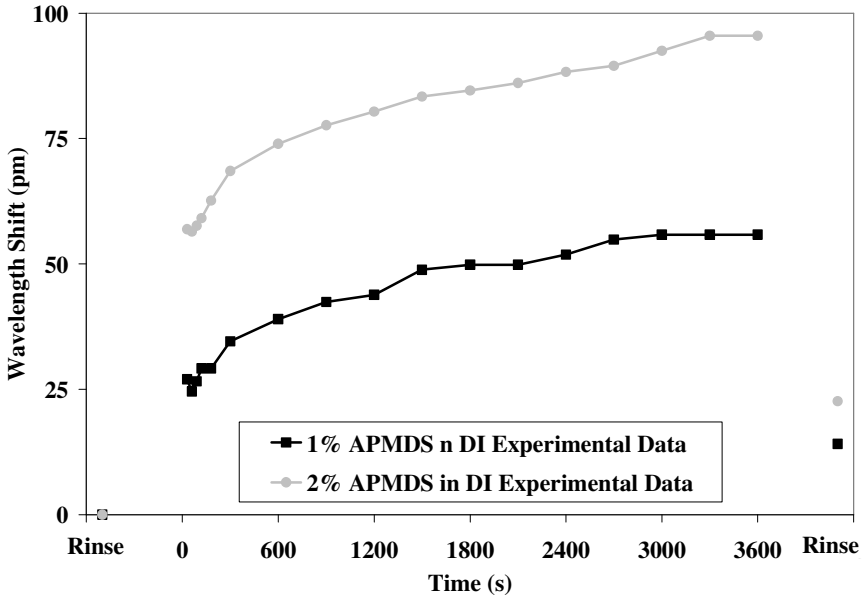

Figure 8.1.3 *In situ* data for silanization with 1% and 2% APDMS concentrations. Solutions are diluted in water. Silanization data is between 0s and 3600s.

When the sensor is first introduced to the solution (at t=0s), the index of refraction is expected to be higher than n_{water} because the surrounding liquid consists of a high index solute dissolved in water. Shifts associated with the initial RI increase are due entirely to

the change in the bulk index around the sensor and not yet due to any adsorption onto the fiber. Data is not acquired at t=0s and so the Bragg shifts are estimated by the expected shifts and sensitivity at indices near water. Within 30s after immersion, the Bragg wavelength has blue-shifted as if a lower index material has accumulated near the evanescent field. After 100s, the data for all APTES and APDMS experiments show a gradual increase over one hour, with the rate of attachment decreasing as more of the fiber surface becomes silanized. The final rinse step is designed to remove excess adsorbed molecules that are not covalently bound to the surface. In APTES and APDMS experiments the final rinse step reduces the Bragg wavelengths to values common between all experiments and independent of the siloxane concentration. Experiments were also conducted in ethanol; the results of which are summarized in Figs. 8.1.4 and 8.1.5.

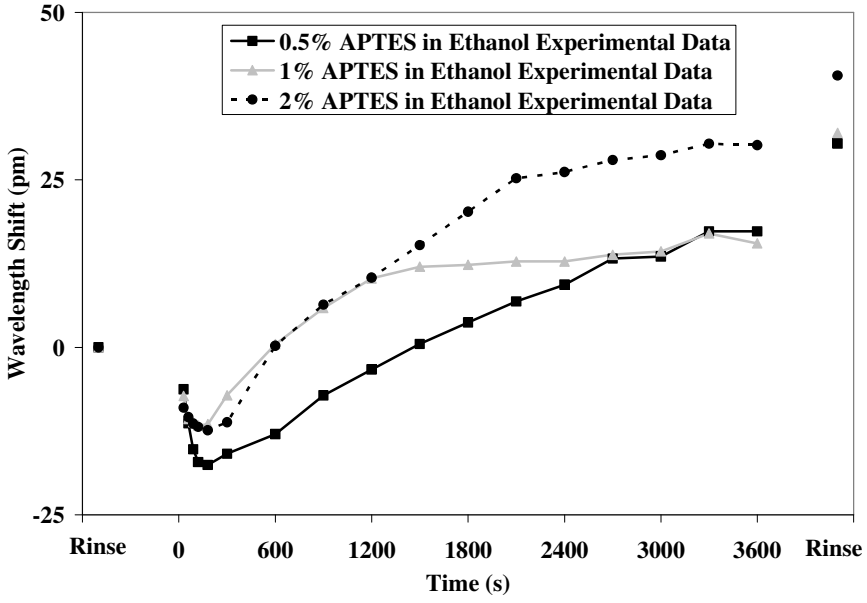

Figure 8.1.4 ***In situ*** **data for silanization with 0.5%, 1%, and 2% APTES concentrations. Solutions are diluted in ethanol. Silanization occurs between 0s and 3600s.**

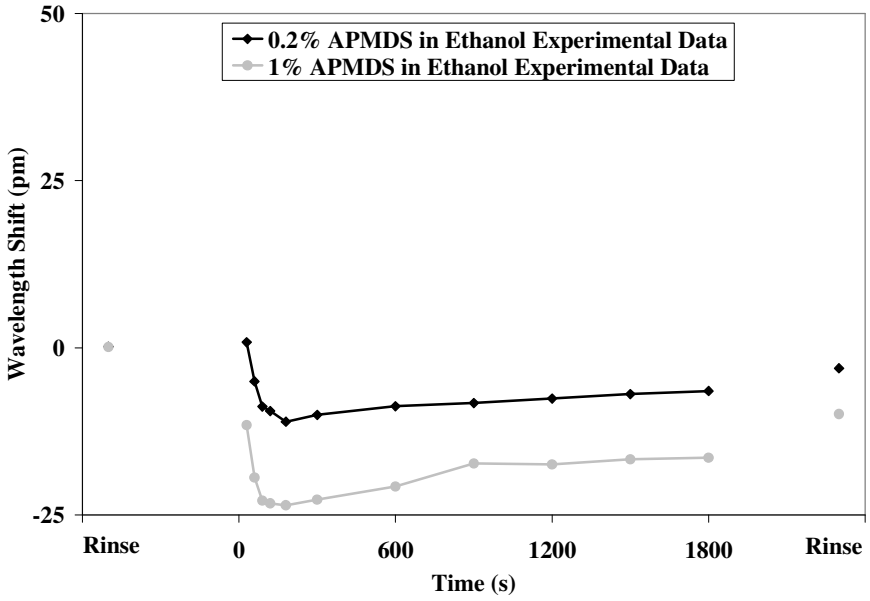

Figure 8.1.5 *In situ* data for silanization with 0.2% and 1% APDMS concentrations. Solutions are diluted in ethanol. Silanization occurs between 0 and 1800s.

The experiments in ethanol share similar qualities as the experiments in water. In each ethanol experiment Bragg shifts indicate that the surrounding index decreases within the first 100 seconds before increasing throughout the rest of the attachment. Data are referenced to the initial Bragg wavelength in the initial ethanol rinse before the attachment. As opposed to experiments in water, the t=30s Bragg shifts are negative for all concentrations and types of silane. When a single monolayer is expected to form within 30 minutes, data reveal that the Bragg wavelength red-shifts slightly above the minimum at approximately 100 second and then in the final rinse step suddenly shift again to slightly longer wavelengths. APTES data show much greater shifts during the formation of a silane layers and again suddenly shift during the final rinse steps. For these experiments, we anticipated an initial red-shift due to the increased index from the rinse solution (t=0s), then saturating red-shifts during the attachment. Finally, the final rinse step should be at the same Bragg wavelength as the final attachment datum (t=30min or 60min). Deviations from the expected shifts may only be explained by the

formation and removal of a low index material near to the evanescent field. Effective index models that incorporate adsorbed water monolayers agree very well with experimental results.

8.1.2 Effective Index Modeling

The data at distinct moments of the real-time Bragg monitoring will be analyzed in this section and compared with results from BPM simulations. BPM models use a 4-layer model with constant refractive indices and varying thicknesses. The inner most layer is the 5μm core with n_{core} = 1.4708. On the fiber surface, the $n_{adsorbed}$ = 1.42 (for APTES and APDMS) with a layer thickness of 1nm per monolayer (determined from computer software ChemDraw). The adsorbed water layer, n_{water}, and the bulk surrounding solution complete the model. Thickness for the immobilized APTES/APDMS molecules and water are variable in modeling and fits are made to be self-consistent at five points in the *in-situ* attachment data. BPM modeling and calculations use 2-D calculations, utilizing the fiber's azimuthal symmetry, in order to reduce the computation time for fine grid sizes. The grid size is maintained at 0.1nm so that 10 data points are calculated within the smallest layer (i.e. 1nm siloxane monolayer). Results are discussed in Section 8.1.3 below.

8.1.3 Fitting Experimental Bragg Shifts

Each experiment is analyzed at the following five points: initial rinse, t=0 immersion, t=100s immersion, t_{end} immersion, and final rinse. All models use the 5μm core and then each experimental step has a unique model beyond the core.

(1) **Initial rinse** models one infinite layer with a refractive index of the solvent (n_{water} or $n_{ethanol}$)

(2) **t = 0s immersion** models one infinite layer with a refractive index of the APTES and APDMS. Refractive indices of these solutions are weighted averages by volume. Expected Bragg shift is calculated.

(3) **t = 100s immersion** models two layers: a water layer with varied thickness and the appropriate APTES/APDMS solution. Water layer thickness is determined from fits.

(4) **t_{end} immersion** models a layer siloxane, a layer of water, and an infinite thickness of the appropriate APTES/APDMS. Water and siloxane layer thicknesses are determined from fits.

(5) **final rinse** models the same siloxane layer as Step 4, a water layer of varied thickness, and an infinitely thick layer of solvent. Water layer thicknesses are determined from fits.

Theoretical fits are shown in Figs. 8.1.6 through 8.1.9.

Figs. 8.1.8 and 8.1.9 include an extra data point to further validate the modeling. This data point represents an additional step to the experiment that is not required for any chemical functionalization procedure. Once the sensor is rinsed in ethanol, it is reintroduced to the 1% or 2% APDMS solution. The Bragg shift between the final solvent rinse and this post-rinse APDMS step should be due only to the solutions refractive index and not an additional immobilization or removal of siloxanes.

Experimental data shows that APDMS is neither removed nor added to the sensor during this step and therefore the procedure is not common practice.

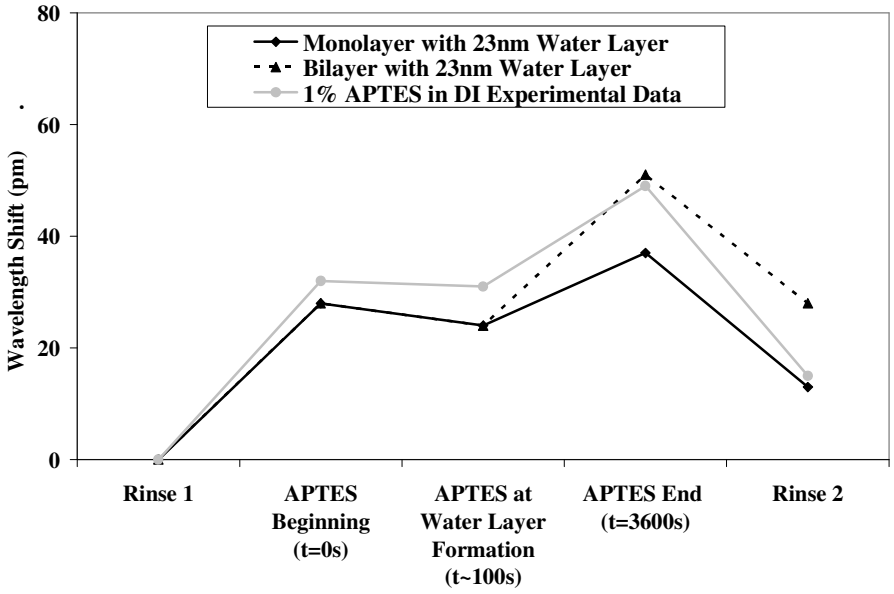

Figure 8.1.6 Theoretical and experimental data from silanization with 1% APTES concentration diluted in water

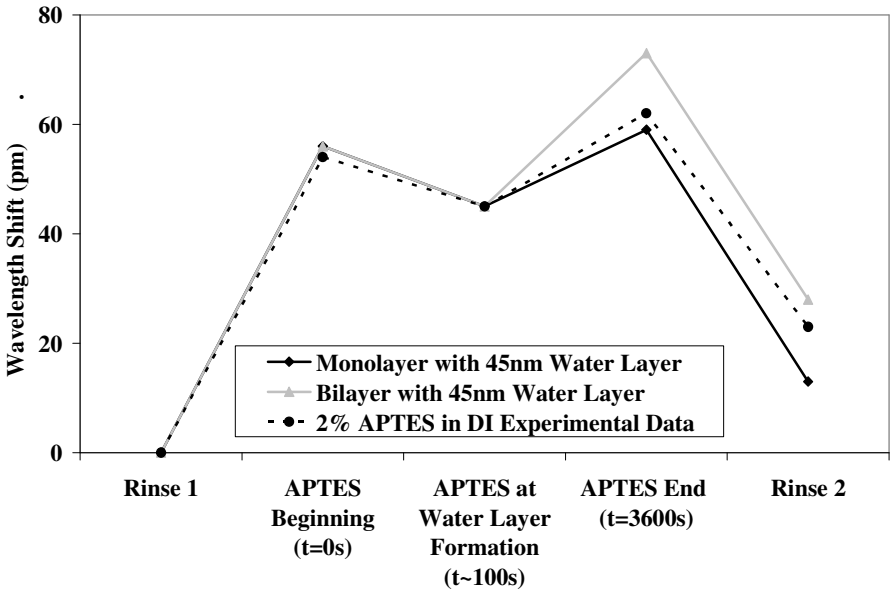

Figure 8.1.7 Theoretical and experimental data from silanization with 2% APTES concentration diluted in water

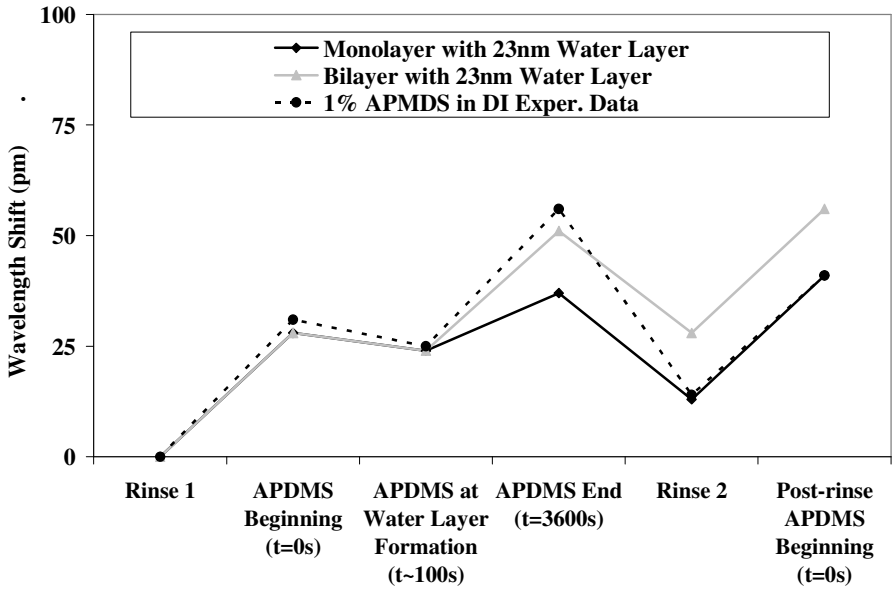

Figure 8.1.8 Theoretical and experimental data from silanization with 1% APDMS concentration diluted in water

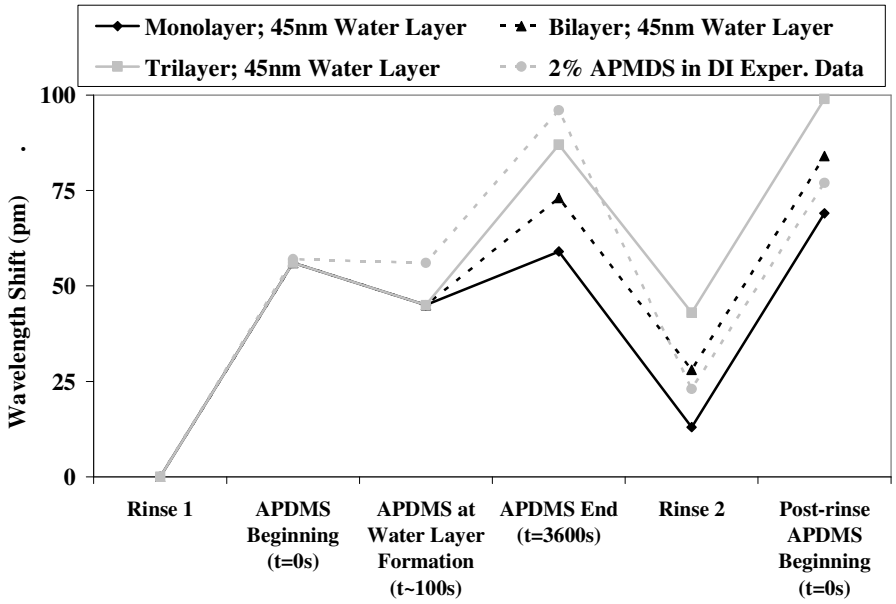

Figure 8.1.9 Theoretical and experimental data from silanization 2% APDMS concentration diluted in water

Specific layer thicknesses vary from one step to another and from one experiment to another but the modeling shows that fitted data supports the idea that water layers form near the fiber surface while multiple monolayers of siloxane attach to the fiber. Water

layers tend to form within the first 100s, which effectively blue-shifts the sensor signal more than was anticipated. Attachments lasting more than one hour showed similar trends of fading attachment rates but there were no signs that the process would stop. Furthermore, fitted data at the Rinse 2 step shows that siloxane layers grow to more than 1-3 monolayers within 30-60 minutes before being rinsed away by the solvent. This reduction in the siloxane layer thickness can be attributed to weak binding forces that promote adsorption of thick siloxane layers to the silica surface. For DNA hybridization experiments, the siloxane layers should be well-organized monolayers that covalently bind to the surface.

These experiments were repeated using ethanol as the diluting solvent. Results are shown in Figs. 8.1.10 and 8.1.11.

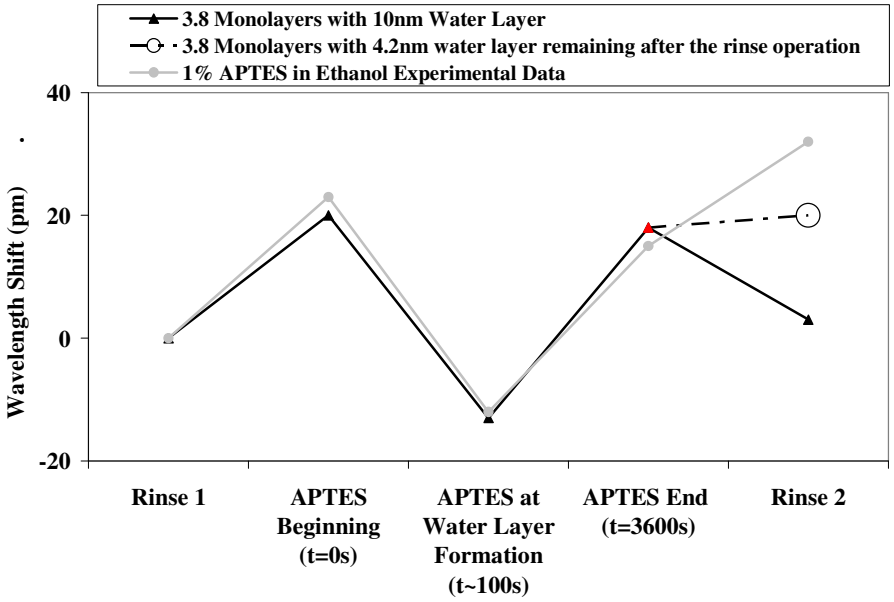

Figure 8.1.10 Theoretical and experimental data from silanization with 1% APTES in ethanol.

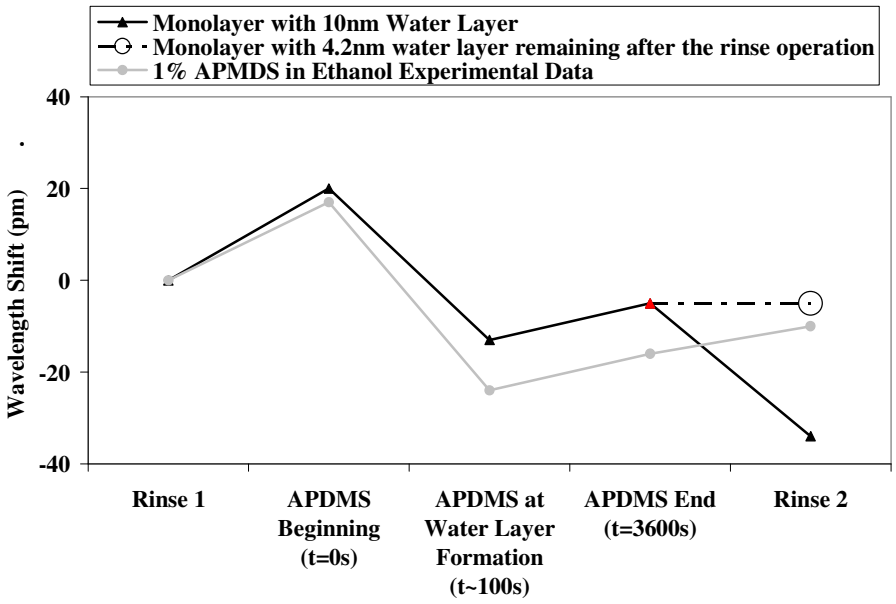

Figure 8.1.11 Theoretical and experimental data from silanization with 1% APDMS in ethanol.

We find that there is again evidence that a water layer forms near the surface of the fiber during experiments performed in ethanol. The ethanol used was 100% concentration so it is believed that the humidity provided the water necessary to red-shift the data [Ref. 8.1.7, 8.1.7, 8.1.9]. Water layer thicknesses are extracted from the t=100s and t_{end} data. In these experiments, a large multilayer of APTES forms around the fiber and binds more tightly than in previous experiments. By modeling a 10nm water layer, fitted and experimental data agree very well when almost 4 monolayers of APTES bind to the surface. As compared with experiments in which water is used as the diluting solvent, the final rinse step data can not be explained if the adsorbed water layer remains after rinsing. At this point, the repeated rinsing in 100% ethanol solution causes the water to be removed from the surface and be replaced by the ethanol rinse solvent.

In summary, real-time monitoring of Bragg shifts throughout the silanization of our fiber sensor revealed the evolution of some interesting phenomena. Unexpectedly

low Bragg shifts and discontinuities in the data agree with the formation of a water layer around the sensor. At the same time, APTES and APDMS covalently bind with the sensor and increase the modal effective index within the evanescent field. As the sensor is immersed for longer periods, siloxanes aggregate near the fiber but do not covalently bind to the surface or any neighboring chemical species. Instead, the weakly-bound siloxanes are mostly removed by repeated solvent rinses, with the exception of APTES diluted in ethanol. Ultimately, the etched FBG sensor detects between 1-2 monolayers of siloxane after rinsing except for APTES, which is expected to attach to itself and form thicker layers.

8.2 DNA Hybridization and Concanavalin A

More complicated chemical processes may be studied with refractive index sensors. DNA hybridization and selective protein binding have been investigated by monitoring shifts in the effective refractive index with our etched FBG sensor.

DNA hybridization is the process in which two complimentary strands of DNA bind to one another. The process is highly selective. DNA components are commercially available and complimentary strands may be purchased separately. Our experiments consisted of immobilizing strands of probe DNA on the sensor surface and then measuring the Bragg shift if the sensor was immersed in a solution of (a) complimentary DNA or (b) non-complimentary DNA. If the target DNA does not properly hybridize with the probe DNA then the subsequent rinse steps would return the Bragg shift to a "pre-target" wavelength. The procedure utilizes glutaraldehyde chemistry to functionalize the surface amines (from siloxanes examined in Section 8.1) in order to

enhance probe DNA immobilization on the surface. The probe DNA was a 21-mer strand. Data shown below was obtained by A. Chryssis and S.M. Lee, though it represents typical experiments that predated the protein study that will be discussed next.

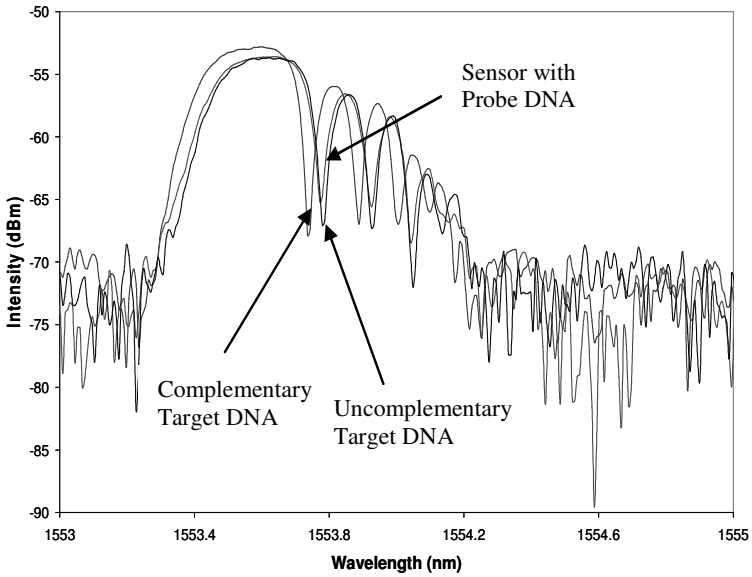

Figure 8.2.1 DNA Hybridization results showing that the Bragg shift is maximized when complimentary DNA is introduced to the silica sensor with immobilized probe DNA. Permission to use this figure received by A. Chryssis.

The final chemical testing experiment examines how the protein Concanavalin A selectively binds with the saccharide glucose. Ideal testing procedures are still being investigated so that the signal to noise ratio between selective and nonselective binding is enhanced. The first steps are ethanol, water, and buffer rinses so that the sensor has been thoroughly rinsed and reference Bragg wavelengths are recorded. The ConA solution is a 1μM concentration dissolved in HEPES-buffered saline (HBS). The HBS solution consists of 10mM HEPES, 150mM NaCl, 1mM $CaCl_2$, 1mM $MnCl_2$, and 1mM $MgCl_2$. The pH is adjusted to 7.4 The lectin is dissolved in this particular buffer solution so that glucose binding is enhanced. Ca^{2+} and Mn^{2+} ions are necessary for glucose to bind with ConA. Buffer rinses use the same HBS mixture without the addition of ConA; ethanol

rinses use 100% ethanol; and water rinses used deionized water. The steps not shown in Fig. 8.2.2 involve silanization of the fiber with either butyltrimethoxysilane (BTMS) or APTES. During protein folding, portions of protein surfaces naturally adopt hydrophobic or hydrophilic characteristics. We thought to immobilized either BTMS (hydrophobic) or APTES (hydrophilic) on the fiber and augment nonselective protein binding to the sensor surface. We used the standard procedures described in Section 8.1 with 1% siloxane solutions. Initial Bragg shifts in the ConA-HBS solution indicate that the ConA is nonselectively attracted to hydrophobic surfaces more than hydrophilic surfaces. Data throughout the 70 minute immersion in ConA-HBS show that the mechanisms that bring ConA to within the evanescent field last throughout immersion in ConA-HBS and even through several buffer rinses. Bragg shifts associated with ConA adsorption to a hydrophobic sensor are 5 times greater than in hydrophilic experiments. With ConA immobilized onto the surface, the sensor is immersed in a 0.5M solution of glucose in buffer or a 0.25M solution of lactose in ethanol. In the first experiment displayed in Fig. 8.2.2, ConA has been effectively immobilized onto the BTMS layer when glucose is introduced. The Bragg shift between pre- and post-glucose rinses was 172pm. In contrast, the same procedure was used to immobilize ConA and then the sensor was immersed in a lactose solution. Lactose is not expected to selectively bind with ConA and therefore in post-lactose rinse steps we expect to se much smaller Bragg shifts than if glucose had been introduced. In fact, the Bragg shift is only 31pm. Lastly, we investigated how ConA would immobilize onto a hydrophilic surface. Bragg shifts are comparatively small. When glucose was introduced to the sensor, the pre- and post-glucose Bragg shift was 16pm. This data is qualitatively sound. If some, though not

much, ConA remained on the sensor surface, some glucose would selectively bind to that ConA though the ConA would likely block other hydrophobic sites that glucose might naturally bind to. In summary, we validate that glucose selectively binds to ConA and that lactose does not bind to the same extent. In the future, other experimental procedures will be explored to enhance the selective binding Bragg shifts and suppress the nonselective Bragg shifts. The first efforts will focus on using water-based only solvents and solutions.

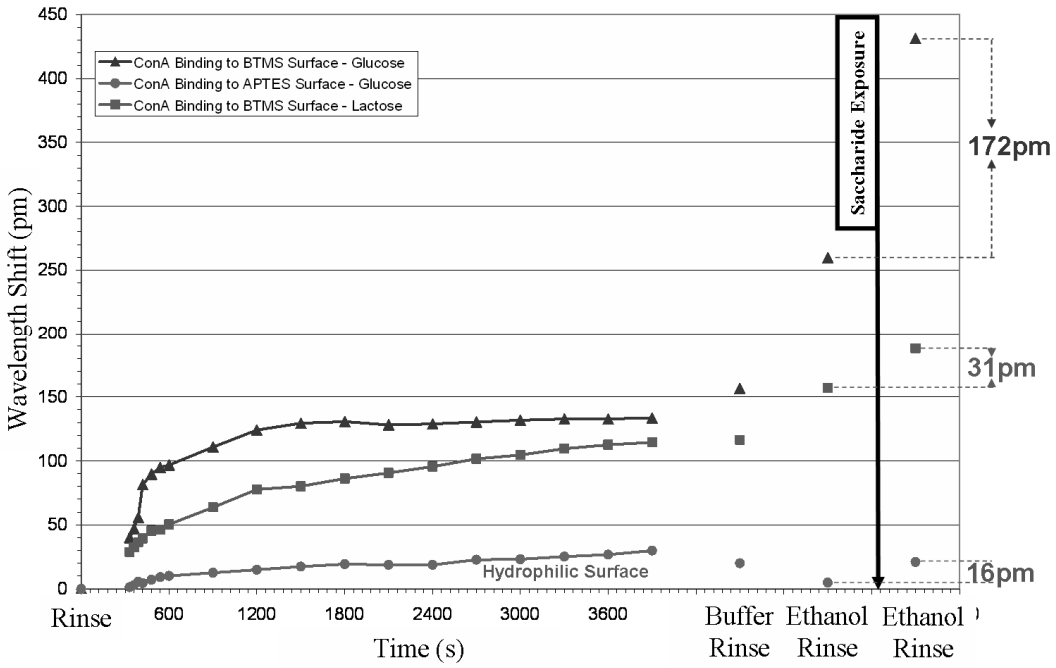

Figure 8.2.2 Summary of experiments immobilizing ConA onto the surface. ConA is immobilized on both hydrophobic and hydrophilic surfaces and then selectivity is tested by introducing glucose and lactose

Chapter 9: Conclusion

Optical fiber refractive index sensors are highly sensitive diagnostic components. Etched Bragg grating sensors can monitor refractive index shifts within $1x10^{-12}$L volumes adjacent to the fiber in real-time. Practical sensors do not use such small volumes, but sensitivity has been enhanced to the extent that the minimum index resolution is now $1x10^{-8}$ and will likely be improved to $5x10^{-9}$ by the end of the etched fiber Fabry Perot sensor's development.

Future sensor research will continue on two fronts: the development of the etched Fabry Perot sensor and the testing of protein conjugation. Highly reflectivity FBGs will narrows the spectral features of the FFP sensor and improve the minimum index resolution. Ultrahigh finesse cavities with 41dB FBG elements may even create a sensor that detects single molecules. The studies of protein conjugation have been extensive and more complicated than expected. Experiments will be entirely performed within environments of water or water-based solutions (i.e. HEPES buffer, etc.) in order to improve the signal to noise ratio between selective and nonselective binding.

Etched fiber sensors may be highly sensitive but they are fragile and difficult to handle. Efforts are being made to transition the project to corrugated planar waveguide sensors. Similarly, the planar structures will reflect narrowband signals that red-shift for increasing modal index. The evanescent fields penetrate the surface corrugation and resonance linewidths depend on carefully choosing the materials and layer thicknesses.

Simulations have been performed with FDTD to optimize the design of siliconoxynitride waveguides. For the purposes of DNA hybridization, silanization, etc. the surfaces will have a thin layer of SiO_2 deposited atop the sensor.

REFERENCES

2.1.1 Agrawal, G., **Fiber-Optic Communication Systems**, 3rd Edition, *John Wiley & Sons*, New York, 2002

2.1.2 Saini, S., et al, "Monolayer Detection of Biochemical Agents using Etched-Core Fiber Bragg Grating Sensor", *IEEE PTL*, Vol. 19, No. 18, 2007, p. 1341

2.1.3 Saini, S., et al, "Monolayer Detection using Etched-Core Fiber Bragg Grating Sensors", *IEEE LEOS*, October 2006

2.3.1 Othonos, A., Kalli, K., **Fiber Bragg Gratings**, Artech House, Inc., Norwood, MA, 1999

2.3.2 D. Johlen, et al, "Fiber Bragg Grating Fiber Fabry Perot Interferometer for a Precise Measurement of the UV-induced Index Change", ECOC 20-24, September 1998, p. 393

2.4.1 Huang, P., et al, "Simulation of Three-Dimensional Optical Waveguides by a Full-Vector Beam Propagation Method", *IEEE JSTQE*, Vol. 29, No. 10, 1993, p. 2639

2.4.2 Okamoto, K., **Fundamentals of Optical Waveguides**, Published by Academic Press, 2006, p.330

2.4.3 J. Homola, et al, "Fiber-optic Sensor Based on Surface Plasmon Resonance", Electronics Letters, February 1996, Vol 32, No 5, p. 480

2.4.4 J. Berthold, "Historical Overview of Microbend Fiber-optic Sensors", J. of Lightwave Tech., July 1995, Vol. 13, No. 7, p. 1193

3.1.1 Hand., D. P., et al, "Photoinduced Refractive Index Changes in Germanosilicate Fibres", *Opt. Letters*, Vol. 15, 1990, p. 144

3.1.2 Wong, D. S., et al, "Stress-birefringence Reduction in Elliptic-core Fibers under UV-radiation", *Opt. Letters*, Vol. 20, 1995, p. 1346

3.1.3 Williams, D. L., et al, *SPIE*, Vol 1513, No. 158, *Glasses for Optoelectronics II*, 1991

3.2.1 Atkins, R. M., et al, "Mechanisms of Enhanced Photosensitivity via Hydrogen Loading in Germanosilicate Glass", *Electron. Letters*, Vol. 29, No. 14, 1993, p. 1234

3.2.3 Dong. L., et al, "Larg3 Photo-induced Changes in Sn-codoped Germanosilicate Fibers", *Photosensitivity and Quadratic Nonlinearity in Glass Waveguides: Fundamentals and Applications*, Vol. 22, 1995, p. 70

3.3.1 Meltz, G., "Formation of Bragg Gratings in Optical Fibers by a Transverse Holographic Method", *Optics Letters*, Vol. 14, No. 15, August 1989, p. 823

3.3.2 Hill, K. O., et al, "Photosensitivity in Optical Fiber Waveguides: Applications to Reflection Filter Fabrication", *Appl. Phys. Lett.,* Vol. 32, 1978, p. 647

3.3.3 Cheng, T. S., et al, "The Application of Spontaneous Vibrational Raman Scattering for Temperature Measurements in High Pressure Laminar Flames", *Combust. Sci. and Tech.*, Vol. 174, 2002, p. 111

3.3.4 Lambda Physik **LPX 250 Instruction Manual**

3.4.2 Rizvi, S., **Handbook of Photomask Manufacturing Technology**, CRC Press, 2005

3.4.3 Sullivan, D. M., **Electromagnetic Simulations Using the FDTD Method**, IEEE Press, 2000

3.5.1 Kittel, C., **Introduction to Solid State Physics**, 6th Edition, Published by John Wiley & Sons, 2005

3.5.2 Kannan, S., et al, "Thermal Stability Analysis of UV-induced Fiber Bragg Gratings", *J. of Lightwave Techn.*, Vol. 15, No. 8, 1997, p. 1478

3.5.3 Kashyap, R., **Fiber Bragg Gratings**, Published by Academic Press, San Diego, CA, 1999

3.5.4 Gruner-Nielsen, L., et al, "Photosensitive Fibers for Highly Reflective Fiber Bragg Gratings",

4.1.1 A. Yariv, et al, "Periodic Structures for Integrated Optics", *IEEE J. of Quant. Electr.,* Vol. QE-13, No. 4, 1977, p.233

4.1.2 Othonos, A., "Fiber Bragg Gratings", *Rev. Sci. Instrum.*, Vol. 68, No. 12, 1997, p. 4309

4.1.3 Hill., K. O., et al, "Fiber Bragg Grating Technology Fundamentals and Overview", *J. of Lightwave Techn.,* Vol. 15, No. 8, 1997, p. 1263

4.2.1 Yariv, A., "Coupled-Mode Theory for Guided-Wave Optics", *IEEE JSTQE*, Vol. QE-9, No. 9, 1973, p. 919

4.2.2 Kogelnik, H., "Filter Response of Nonuniform Almost-Periodic Structures", *The Bell System Technical Journal*, January 1976, p. 109

4.2.3 Yamada, M., et al, "Analysis of Almost-Periodic Distributed Feedback Slab Waveguides via a Fundamental Matrix Approach", *Applied Optics*, Vol. 26, No. 16, 1987, p. 3474

4.3.1 Hill, K. O., "Photosensitivity in Optical Fiber Waveguides: Applications to Reflection Filter Fabrication", *Appl. Phys. Lett.*, Vol. 32, No. 10, 1978, p. 647

4.3.2 Ferreira, L. A., et al, "Simultaneous Measurement of Strain and Temperature Using Interferometrically Interrogated Fiber Bragg Grating Sensors", *Opt. Eng.*, Vol. 38, No. 9, 2000, p. 2226

5.2.1 Barmenkov, et al, “Effective Length of Short Fabry Perot Cavity Formed by Uniform Fiber Bragg Gratings”, *Optics Express*, Vol. 14, No. 14, 2006, p. 6394

5.5.1 Kersey, A. D., et al, “Fiber Grating Sensors”, *J. of Lightwave Techn.*, Vol. 15, No. 8, 1997, p. 1442

5.5.2 Lee, C. E., et al, “Optical Fiber Fabry Perot Sensors for Smart Structures”, *Smart Mater. Struct.*, Vol. 1, 1992, p. 123

5.5.3 Liang, W., Yariv, A., et al, “Highly Sensitive Fiber Bragg Grating Refractive Index Sensors”, *Applied Physics Letters*, Vol. 86, No. 151122, 2005

5.5.4 Armani, A. M., Vahala, K. J., et al, “Label-free, Single Molecule Detection with Optical Microcavities”, *Science*, Vol. 317, 2007, p. 783

6.2.1 Chryssis, A. N., et al, “Increased Sensitivity and Parametric Discrimination Using Modes of an Etched-Core Fiber Bragg Grating Sensor”, *IEEE Photon. Techn. Lett.,* VOl. 18, No. 1, 2006, p. 178

6.4.1 conversation with Prof. J. Goldhar, January 2008

6.6.1 Renner, H., “Effective-index Increase, For Birefringence, and Transition Losses in UV-side-illuminated Photosensitive Fibers”, *Opt. Express*, Vol. 9, No. 11, 2001, p. 546

6.7.1 Liang, W., et al, “Highly Sensitive Fiber Bragg Grating Refractive Index Sensors”, *Applied Phys. Lett.,* Vol. 86, 151122, 2005

7.1.1 Chryssis, A., et al, “High Sensitivity Evanescent Field Fiber Bragg Grating Sensor”, *IEEE PTL*, Vol. 17, No. 6, 2005, p. 1253

7.1.2 Chryssis, A., et al, "Detecting Hybridization of DNA by Highly Sensitive Evanescent Field Etched Core Fiber Bragg Grating Sensors", *IEEE JSTQE*, Vol. 11, No. 4, 2005, p. 864

7.1.3 Chryssis, A., et al, "Increased Sensitivity and Parametric Discrimination Using Higher Order Modes of Etched-Core Fiber Bragg Grating Sensors", *IEEE PTL*, Vol. 18, No. 1, 2006, p. 178

8.1.1 Beckers, J. W., et al, "The Covalent and Three-Dimensional Structure of Concanavalin A", *J. of Biological Chemistry*, Vol. 250, No. 4, 1975, p. 1513

8.1.2 Homs, M. C., et al, "DNA Sensors". *Analytical Letters*, Vol. 35, 2002, p. 1875

8.1.3 Pavlovic, E., et al, "Spatially Controlled Covalent Immobilization of Biomolecules on Silicon Surfaces", Ph. D. dissertation, Uppsala University, Sweden, 2003

8.1.4 Kurth, D. G., et al, "Thin Films of 3-APTES on Aluminum Oxide and Gold Substrates, *Langmuir*, Vol. 11, 1995, p. 3061

8.1.5 Mon, J. H., et al, "Formation of Uniform Aminosilane thin layers: an imine formation to measure relative surface density of the amine group", *Langmuir*, Vol. 12, 1996, p. 4621

8.1.6 Oh, So., et al, "Characteristics of DNA Microarrays Fabricated on Various Aminosilane Layers", *Langmuir*, Vol. 18, 2002, p. 1764

8.1.7 Asay, D. B., et al, "Effects of Adsorbed Water Layer Structure on Adhesion Force of Silicon Oxide Nanoasperity contact in humid ambient", *J. Chem. Phys.,* Vol. 124, 2006, p. 174712

8.1.8 Freund, J., et al, "How Dry are Dried Samples?", *Microscopy Research and Technique*, Vol. 44, 1999, p. 327

8.1.9 Takahagi, T., et al, "Adsorbed Water on a Silicon Wafer Surface Exposed to Atmosphere", *Jpn. J. Appl. Phys.,* Vol. 40, 2001, p. 6198